Characterization and radiation hardness studies of the silicon microstrip sensors for the CBM experiment

Dissertation
zur Erlangung des Doktorgrades
der Naturwissenschaften

vorgelegt beim Fachbereich Physik
der Johann Wolfgang Goethe-Universität
in Frankfurt am Main

von
Ievgeniia Momot
aus Chernihiv, Ukraine

Frankfurt am Main   (2019)
(D 30)

vom Fachbereich Physik der
Johann Wolfgang Goethe-Universität als Dissertation angenommen.

Dekan: Prof. Dr. Michael Lang

Gutachter: Prof. Dr. Peter Senger
Prof. Dr. Joachim Stroth

Datum der Disputation:

Abstract

High-energetic heavy-ion collisions offer the unique opportunity to produce and to study dense nuclear matter in the laboratory. The future Facility for Antiproton and Ion Research (FAIR) in Darmstadt, Germany, will provide beams of heavy nuclei up to kinetic energies of 11 GeV/nucleon. At these energies, the nuclear matter in the collision zone of two nuclei will be compressed to densities of up to $5 - 10$ times the saturation density of atomic nuclei, similar to matter densities existing in the core of massive neutron stars. Under those conditions, nucleons are expected to melt and form a new state of matter, which consists of quarks and gluons, the so called Quark-Gluon Plasma (QGP). The search for such a phase transition from hadronic to partonic matter, and the exploration of the nuclear matter equation-of-state at high densities are the major goals of heavy ion experiments worldwide.

The observables, which are proposed to probe the properties of dense nuclear matter and possible phase transitions, include multi-strange hyperons, antibaryons, lepton pairs, collective flow of identified particles, fluctuations and correlations of various particles, particles containing charm quarks, and hypernuclei. These observables have to be measured in multi-dimensions, i.e. as function of collision centrality, rapidity, transverse momentum, energy, emission angle, etc., which requires extremely high statistics. Moreover, some of these particles are produced very rarely. Therefore, the Compressed Baryonic Matter (CBM) experiment at FAIR is designed to run at collision rates of up to 10 MHz, in order to perform measurements with unprecedented precision. Due to the complicated decay topology of many observables, no hardware trigger can be applied, and the data have to be analysed online in order to filter out the interesting events. This strategy requires free-streaming read-out electronics, which provides time stamps to all detector signals, a high performance computer center, and high-speed reconstruction algorithms, which provide an online track and event reconstruction based on time and position information of the detector hits (”4-D“ reconstruction).

The core detector of the CBM experiment is the Silicon Tracking System (STS). The main task of the STS is to provide track reconstruction and momentum determination of charged particles originating from beam-target interactions. To fulfil the whole tasks the STS is located in the large gap of a superconducting dipole magnet with a bending power of 1 Tm providing momentum measurements for charged particles. The STS comprises 8 detector stations, which are positioned from 30 cm to 100 cm downstream the target. The corresponding active area of the stations grows up from $40{\times}50$ cm^2 up to $100{\times}100$ cm^2 with a total area of $4\,\text{m}^2$. The silicon double-sided sensors exhibit 1024 strips on each side with a stereo angle at p-side of 7.5° and a strip pitch of 58 μm. The strip length ranges from 2 cm for sensors located in a close vicinity to the beam axis, up to 12 cm for other sensors where the flux of the reaction products drops down substantially. In total, the STS consist of 896 sensors mounted on 106 detector ladders. The detector readout electronics

dissipates $40\,\mathrm{kW}$ and will be equipped with a CO_2 bi-phase cooling system. The detector including electronics will be mounted in a thermal enclosure to allow for sensor operation at below $-5°C$ which minimizes radiation induced leakage currents.

The task of the STS is to measure the trajectories of up to 800 charged particles per collision with an efficiency of more than 95% and a momentum resolution of $1-2\%$. In order to guarantee the required performance over the full lifetime of the CBM experiment, the detector system has to have a low material budget, a high granularity, a high signal-to-noise (SNR) ratio, and a high radiation tolerance. As a result of optimisation studies, the STS consists of double-sided silicon microstrip sensors, about $300\,\mu$m thick, which have to provide a SNR ratio of more than 10, even after radiation with the expected equivalent lifetime fluence of 10^{14} $1\,\mathrm{MeV\,n_{eq}cm^{-2}}$.

This thesis is devoted to the characterization of double-sided silicon microstrip sensors with an emphasis on investigation of their radiation hardness. Different prototypes of double-sided silicon sensors produced by two vendors have been irradiated by 23 MeV protons up to the double life time fluence for the CBM experiment (2×10^{14} $1\,\mathrm{MeV\,n_{eq}cm^{-2}}$). The sensor properties have been characterised before and after irradiation. It was found, that after irradiation with a double lifetime fluence the leakage current increased 1000 times, which results in an increased shot noise. Moreover, the relative charge collection efficiency of irradiated with respect to non-irradiated sensors drops down to 85% for the lifetime equivalent fluence, and down to 73% for the double lifetime fluence, both for the p-side and n-side. For non-irradiated sensors the SNR was found to be in the range of $20-25$, whereas for irradiated sensors it dropped down to $12-17$.

In addition to the sensor characterization, a part of this thesis was devoted to the optimisation of the sensor readout scheme. In order to investigate the possible increase of SNR, and to reduce the number of readout channels in the outer aperture of STS, three versions of routing lines have been realized for the p-side readout of the sensor prototype, and have been tested in the laboratory and under beam conditions. The tests have been performed with different inclination angles between beam direction and sensor surface, corresponding to the polar angle acceptance of the CBM experiment, which is from $2.5°$ to $25°$.

As a result of the studies carried out in this thesis work, the radiation hardness of the double-sided silicon microstrip sensors developed for the CBM STS detector was confirmed. Also the advantage of individual read-out of sensor channels in the lateral regions of the detector was verified. This allowed to start the tendering process for sensor series production in industry, an important step towards the construction of the detector in the coming years.

Kurzfassung

Hochenergetische Schwerionenkollisionen stellen die einzige Möglichkeit dar, dichte Kernmaterie im Labor herzustellen und zu untersuchen. Die zukünftige Beschleunigereinrichtung "Facility for Antiproton and Ion Research (FAIR)" in Darmstadt, Deutschland, wird Strahlen schwerer Kerne bis zu kinetischen Energien von 11 GeV/Nukleon liefern. Bei diesen Energien wird die Kernmaterie in der Kollisionszone zweier Kerne auf Dichten bis zu 5-10 mal der Sättigungsdichte von Atomkernen komprimiert, ähnlich den im Kern massereicher Neutronensterne vorhandenen Materiedichten. Unter diesen Bedingungen wird erwartet, dass Nukleonen schmelzen und einen neuen Materiezustand bilden, der aus Quarks und Gluonen besteht, das sogenannte Quark-Gluon-Plasma (QGP). Die Suche nach einem solchen Phasenübergang von hadronischer zu partonischer Materie und die Untersuchung der Zustandsgleichung von Kernmaterie bei hohen Dichten sind die Hauptziele von Schwerionenexperimenten weltweit.

Zu den Observablen, die zur Untersuchung der Eigenschaften dichter Kernmaterie und möglicher Phasenübergänge dienen können, gehören Hyperonen mit mehreren Strange-Quarks, Antibaryonen, Leptonpaare, kollektiver Fluss identifizierter Teilchen, Fluktuationen und Korrelationen verschiedener Teilchenproduktionsgrössen und -raten, ferner Teilchen, die Charm-Quarks enthalten, und Hyperkerne. Diese Observablen müssen in mehreren Dimensionen gemessen werden, d. h. als Funktion der Kollisionszentralität, der Rapidität, des Transversalimpulses, der Energie, des Emissionswinkels usw., was extrem hohe Statistiken erfordert. Darüber hinaus werden einige dieser Teilchen sehr selten produziert. Daher ist das Compressed Baryonic Matter (CBM) Experiment bei FAIR, das Gegenstand der folgenden Diskussion ist, für Kollisionsraten von bis zu 10 MHz ausgelegt, um Messungen mit bisher unerreichter Genauigkeit durchzuführen. Aufgrund der komplizierten Zerfallstopologien vieler Observablen kann kein Hardware-Trigger angewendet werden, und die Daten müssen online analysiert werden, um die interessanten Ereignisse herauszufiltern. Diese Strategie erfordert eine Ausleseelektronik mit freiem Streaming, die allen Detektorsignalen Zeitstempel zuweist und an ein Hochleistungsrechenzentrum leitet. Dort wird mit schnellen Rekonstruktionsalgorithmen eine Online-Spur- und Ereignisrekonstruktion basierend auf Zeit- und Positionsinformationen der Detektordaten durchgeführt ("4-D" Rekonstruktion).

Der zentrale Detektor des CBM-Experiments ist das Silicon Tracking System (STS). Die Hauptaufgabe des STS besteht darin, Spurrekonstruktion und Impulsbestimmung von geladenen Teilchen vorzunehmen, die aus Strahl-Target Wechselwirkungen stammen. Um diese Aufgaben zu erfüllen, befindet sich der STS zwischen den Polschuhen eines supraleitenden Dipolmagneten mit einem Ablenkvermögen von 1 Tm. Der STS umfasst 8 Detektorstationen, die zwischen 30 cm und 100 cm hinter dem Target positioniert sind. Die entsprechende aktive Fläche der Stationen wächst von $40 \times 50\,\text{cm}^2$ auf $100 \times 100\,\text{cm}^2$ mit einer Gesamtfläche von etwa $4\,\text{m}^2$. Die doppelseitigen Siliziumsensoren weisen auf jeder Seite 1024 Streifen mit einem Stereowinkel

auf der p-Seite von $7,5°$ und einem Streifenabstand von $58\,\mu$m auf. Die Streifen-länge reicht von $2\,$cm für Sensoren, die sich in unmittelbarer Nähe der Strahlachse befinden, bis zu $12\,$cm für andere Sensoren, bei denen der Fluss der Reaktionspro-dukte erheblich abfällt. Insgesamt bestehen das STS System aus 896 Sensoren, die auf 106 Detektorleitern montiert sind. Die Ausleseelektronik des Detektors hat eine Leistungsaufnahme von $40\,$kW und wird mit einem zweiphasigen CO_2-Kühlsystem ausgestattet. Der Detektor einschließlich der Elektronik wird in einem thermisch isolierten Gehäuse montiert, um einen Sensorbetrieb bei einer Temperatur unter $-5°$C zu ermöglichen, bei dem strahlungsinduzierte Leckströme reduziert werden.

Die Aufgabe des STS Detektors besteht darin, die Trajektorien der am Target pro-duzierten geladenen Teilchen (bis zu etwa 800 pro nuklearer Wechselwirkung) mit einer Effizienz von größer 95% und einer Impulsauflösung $\Delta p/p$ von besser 2% zu vermessen. Um die erforderliche Leistungsfähigkeit über die gesamte Lebensdauer des CBM-Experiments zu gewährleisten, muss das Detektorsystem ein niedriges Ma-terialbudget, eine hohe Granularität, ein hohes Signal-zu-Rausch-Verhältnis (SNR) und eine hohe Strahlungstoleranz aufweisen. Als Ergebnis von Optimierungsstu-dien besteht das STS aus doppelseitigen, etwa $300\,\mu$m dicken Silizium-Mikrostreifen-Sensoren, die selbst nach Bestrahlung mit dem erwarteten äquivalenten Lebensdauer-Fluss von $1 \times 10^{14}\,1\,$MeV n_{eq}cm^{-2} einen SNR-Wert größer 10 aufweisen müssen.

Diese Dissertation widmet sich der Charakterisierung doppelseitiger Silizium-Mik-rostreifen-Sensoren mit dem Schwerpunkt der Untersuchung ihrer Strahlungshärte. Verschiedene Prototypen doppelseitiger Siliziumsensoren mit einer Dicke von etwa $300\,\mu$m, von zwei Herstellern produziert, wurden mit $23\,$MeV-Protonen bis zur dop-pelten Lebensdauerfluenz für das CBM-Experiment bestrahlt ($2\times10^{14}\,1\,$MeV n_{eq}cm^{-2}). Die Sensoreigenschaften wurden vor und nach der Bestrahlung charakterisiert. Es wurde festgestellt, dass der Leckstrom nach einer Bestrahlung mit einer doppelten Lebensdauer auf das 1000-fache anstieg, was zu einem erhöhten Rauschen führte. Darüber hinaus sinkt der relative Ladungssammlungswirkungsgrad von bestrahlten Sensoren in Bezug auf nicht bestrahlte Sensoren für die lebensdaueräquivalente Fluenz auf 85% und für die doppelte Lebensdauerfluenz auf 73%, sowohl für die p-Seite als auch für die n-Seite. Bei nicht bestrahlten Sensoren lag das SNR im Bereich von 20 bis 25, während es bei bestrahlten Sensoren auf 12 bis 17 fiel.

Neben der Sensorcharakterisierung wurde ein Teil dieser Arbeit der Entwick-lung des STS-Detektormoduls, der Basisdetektoreinheit, gewidmet. Es umfasst einen Sensor, Kabel mit geringer Masse, die den Sensor und die Ausleseelektronik verbinden, und eine tragende Struktur. Die Testergebnisse für verschiedene Verbin-dungsschemata zwischen Sensoren und Ausleseelektronik werden dargestellt. Um eine mögliche Erhöhung des SNR in den lateralen Bereichen des STS zu untersuchen,

und eine Veringerung der Anzahl der Auslesekanäle dort, wurden drei Varianten von gruppierten Ausleseleitungen realisiert und im Labor und Strahlexperiment getestet. Dabei wurden unterschiedlichen Neigungswinkeln zwischen Strahlrichtung und Sensoroberfläche berücksichtigt, entsprechend der Polarwinkelakzeptanz des CBM-Experiments von 2.5° bis 25°.

Als Ergebnis der in dieser Dissertation durchgeführten Untersuchungen wurde die Strahlungshärte der für den CBM STS-Detektor entwickelten doppelseitigen Silizium-Mikrostreifen-Sensoren bestätigt. Ebenfalls bestätigt wurde der Vorteil des individuellen Auslesens von Sensorkanälen in den seitlichen Bereichen des Detektors. Dies ermöglichte den Start des Ausschreibungsverfahrens für die Sensorserienfertigung in der Industrie, ein wichtiger Schritt auf dem Weg zum Detektoraufbau in den kommenden Jahren.

Contents

1
Introduction

Ordinary substances exist in different phases such as gas, liquid, and solid, depending on the temperature and pressure. A variation of these conditions may cause a transition from one phase to the other, and the boundaries between the different lines can be drawn in a diagram as function of temperature and pressure. These lines could meet at the triple point where several phases coexist. In general, there is also a critical point where the distinct phase boundary between liquid and gas ends, and beyond there is a continuous "crossover" between the two phases. The phase boundaries, the triple point and the critical point represent fundamental landmarks in the phase diagram of each substance.

Substantial experimental and theoretical efforts worldwide are devoted to the exploration of the QCD phase diagram of strongly interacting matter. In the laboratory hot and dense nuclear matter can be generated in a wide range of temperatures and densities by colliding atomic nuclei at high energies. In the collision zone, the matter is heated and compressed for a very short period of time. At kinetic beam energies around several hundred MeV per nucleon, nucleons are excited to short-lived states (baryonic resonances) which decay by the emission of pions. At higher beam energies, also strange mesons and hyperons, and finally baryon-antibaryon pairs are created. This mixture of baryons, antibaryons and mesons, all strongly interacting particles, is generally called hadronic matter, or baryonic matter if baryons prevail. If the energy pumped into this fireball is sufficiently large, the temperatures and/or

densities reach critical values: the hadrons melt, and the constituents, the quarks and gluons, may move freely forming a new phase, the Quark-Gluon-Plasma.

Fist attempts to create and investigate compressed nuclear matter were in the 1970s with experiments at the Bevatron at the Lawrence Berkeley National Laboratory (LBNL) (with $E_{Lab} \approx 2\,A$GeV) and at the Synchro-Phasotron at the Joint Institute for Nuclear Research (JINR) (collision energies of the order of 100 AMeV). To discover QGP, next experiments moved towards larger energies. The Alternating Gradient Synchrotron (AGS) [1] at the Brookhaven National Laboratory (BNL) has studied the energies $E_{Lab} = 2-11\,A$GeV, while the Super Proton Synchrotron (SPS) [2] at Centre Europeen de la Recherche Nuclaire (CERN) has addressed the energy interval of $E_{Lab} = 20-160\,A$GeV. To conduct studies with higher center-of-mass energies $\sqrt{s_{NN}}$, the collider configuration has been more preferred then the fixed target experiments. The Relativistic-Heavy-Ion-Collider (RHIC) [3, 4] at BNL has been the first collider experiment for HIC (Heavy Ion Collisions) and it is currently able to span a wide range of center-of-mass energies, i.e. $\sqrt{s_{NN}} = 5-200\,A$GeV. Measurements at 200 AGeV provided results, which indicate that a QGP has been created during the collisions and that it behaves as an almost perfect fluid [5]. However, there are indications that a QGP can be produced also at lower energy. The upper limit set by RHIC has been overtaken by the Large Hadron Collider (LHC) [6], which is currently performing collisions at the TeV scale. Complementary to these high-energy collision programs, some experiments (FOPI [7], KaoS [8] and HADES [9]) have studied low energy reactions ($E_{Lab} = 2\,A$GeV) at the SchwerIonen Synchrotron (SIS) at the Gesellschaft für Schwerionenforschung (GSI Helmholtzzentrum für Schwerionenforschung) in Darmstadt, Germany.

In the kinetic beam energy range from 2 AGeV to about 30 AGeV, where the highest net-baryon densities are expected to be produced in heavy-ion collisions, only exploratory measurements have been performed so far. Due to technical limitations, in particular concerning the rate capabilities of the experiments, mainly abundantly produced particles like protons, pions, kaons, and lambdas could be measured with sufficient statistics to allow for a multidimensional analysis. In order to explore the high net-baryon density region of the QCD phase diagram, new facilities are under construction: the Facility for Antiprotons and Ion Research (FAIR) at GSI [10] and the Nuclotron-based Ion Collider fAcility (NICA) [11]. At FAIR, fixed target experiments will be performed within the energy range $\sqrt{s_{NN}} = 2.74-4.9\,$GeV (at SIS100 synchrotron), with the Compressed Baryonic Matter (CBM) experiment [12]. NICA is a collider facility, which will carry out experiments for example Baryonic Matter at Nuclotron (BM@N) [13] and Multi Purpose Detector (MPD) at $\sqrt{s_{NN}} = 4-11\,$GeV. In addition to the new facilities, the beam energy scan (BES) performed

at RHIC [14] is currently studying intermediate energies: $\sqrt{s_{NN}} = 5.5 - 62.4\,\text{GeV}$. However, the RHIC collider faces the problem that the luminosity rapidly decreases with decreasing beam energy.

The hypothetical phases of strongly interacting matter and their boundaries are illustrated in Fig. 1.1, as function of temperature versus net baryon density. This represents a qualitative look, which is based on theoretical considerations and existing experimental data, which have to be still confirmed by future experiments. The high temperature region has been investigated experimentally at LHC (Large Hadron Collider) and RHIC (Relativistic Heavy Ion Collider). In this regime, matter is produced at low net baryon densities, where number of baryons and antibaryons is almost equal. This kind of conditions existed in the early Universe several microseconds after the Big Bang. While cooling, the system hadronises, and finally freezes out chemically at a temperature around 160 MeV [15, 16] or about one trillion Kelvin. This temperature coincides with the transition temperature predicted by the Lattice QCD calculations [17, 18] for a smooth crossover transition from partonic to hadronic matter [19].
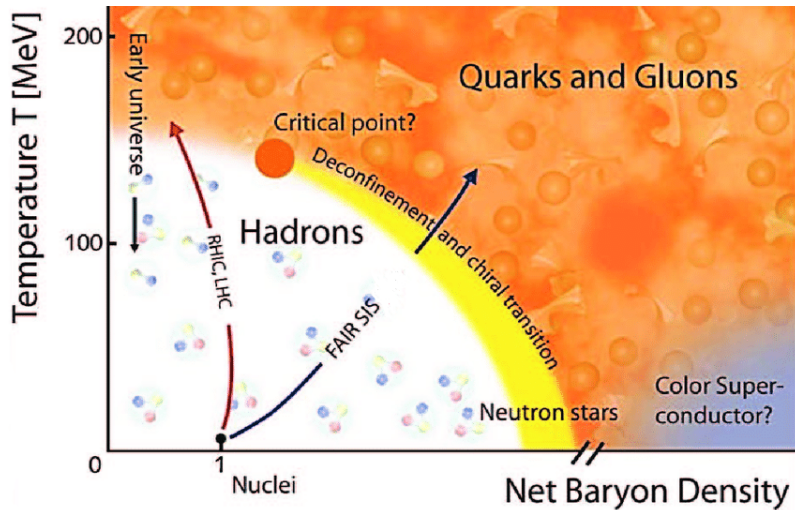

Figure 1.1: Schematic view on QCD phase diagram in the temperature and net baryon density plane, where different phases of strongly interacting matter are depicted [20].

Up to now, lattice QCD is not able to make predictions for the high net-baryon density region of the QCD phase diagram. Structures like a first order deconfinement and chiral transition, a critical point, or a quarkyonic phase are predicted by QCD inspired models [21].

Heavy-ion beams in the energy range between 2 AGeV and about 14 AGeV are ideally suited to explore the properties of dense baryonic matter. According to the transport calculations, energy densities up to 2.5 GeV fm^3 and baryon densities of

2 - 7 times the saturation density ρ_0 are expected to be reached in the center of the reaction zone [22]. Above a certain critical energy density, nuclear matter is believed to exist in a deconfined state. At such densities, the nucleons will start to melt and to dissolve into their constituents: quarks and gluons. According to transport model and hydrodynamical calculations [23], in central Au+Au collisions at 5 GeV, the nuclear fireball will be compressed to more than 5 times the saturation density ρ_0 and 10 GeV to above $8\rho_0$, which is illustrated in Fig. 1.2. Such conditions prevail in core collapse supernovae and in the core of neutron stars. At SIS100 energies it will be possible to investigate the properties of baryon resonances close to the phase boundary, and, therefore, to provide important information on this transition region of the QCD phase diagram.
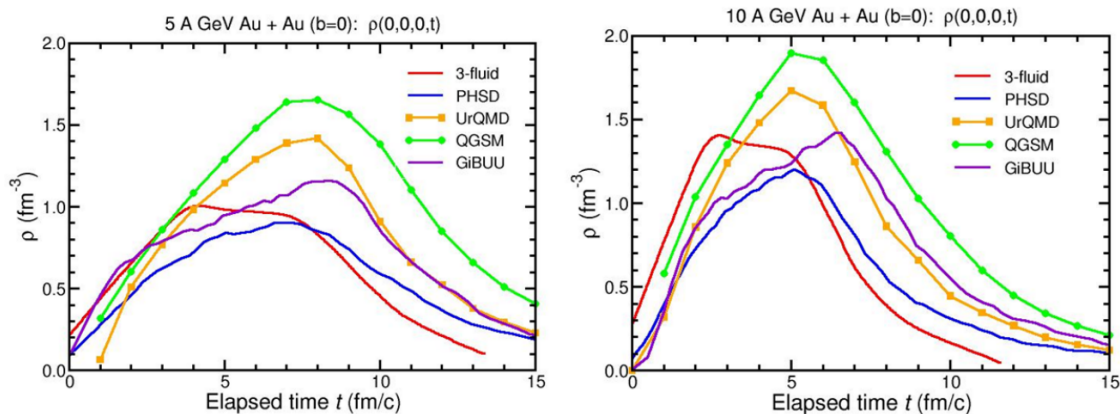

Figure 1.2: Evolution of the central net baryon density $\rho(t)$ as a function of elapsed time calculated by different transport models and by a 3-fluid hydrodynamics code for central Au+Au collision at $5\,A\mathrm{GeV}$ (left panel) and at $10\,A\mathrm{GeV}$ (right panel) [23].

The CBM experiment offers a broad range of physics cases to be addressed by reaching large net baryon densities with an extreme high interaction rate.

1.1   Physics of the CBM experiment

A comprehensive study of bulk and rare observables is foreseen in the diverse experimental program of the CBM experiment. In particular, rare probes are expected to be studied with unprecedented precision despite the very low production cross-sections. Among them, there are extremely rare ones, e.g., multi-strange anti-hyperons, open and hidden charm. The multiplicity of such probes is expected to be one in a million collisions or even less. In Fig. 1.3, a statistical model calculations of the particle multiplicities times branching ratio are shown in central Au+Au collision at $10.7\,A\mathrm{GeV}$ [24]. In order to compensate for these low cross-sections, the

experiment has to run at very high interaction rates. This is several orders of magnitude higher than the capability of current or other planned experiments in the field of relativistic heavy-ion physics (see Fig. 1.4).
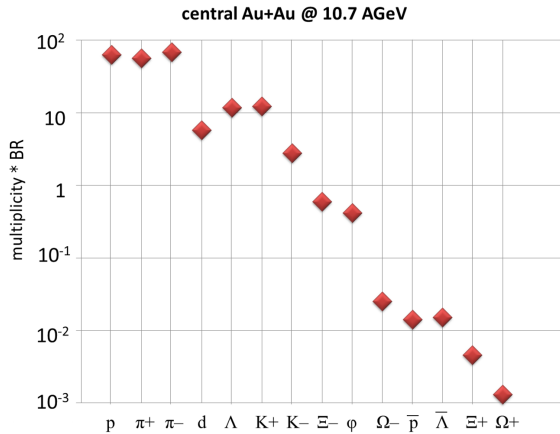

Figure 1.3: Model predictions for yields (multiplicity times branching ratio) of probes intended to be measured by CBM @10.7 AGeV calculated with the statistical model [25].
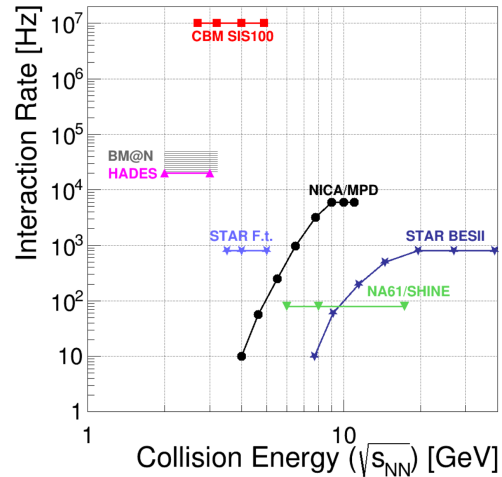
Figure 1.4: Interaction rates achieved by existing and planned heavy-ion experiments as function of beam energy [26].

The beam energies foreseen at SIS100 appear to be very well suited for observables which give the information about the properties of dense nuclear matter. The measurements will shed light on fundamental scientific questions, such as: equation of state of the dense strongly interacting matter, location of possible phase transition from QGP to hadronic phase, identification of the different phases of strongly interacting matter, properties of hadrons in dense baryonic matter. The broad physics program of the CBM experiment includes studies of both bulk observables and the rare probes. The CBM physics cases are summarized below.

Collectivity

The collective flow of hadrons is driven by the pressure gradient created in the early stage of fireball evolution and provides information on the dense phase of the collision [27, 28]. The strength of the elliptic flow and its dependence on the particle transverse momentum can shed light on the degrees of freedom which prevail in the early stage of collision.

The suppression of the directed flow is sensitive to the details of the phase transition, the softening of the QCD matter EOS, and is an important observable for clarifying the role of partonic degrees of freedom [29].

Of particular interest is the flow of particles not affected to rescattering like Ω hyperons or ϕ mesons, for which no experimental data exist in the CBM energy range. These measurements will significantly contribute to our understanding of the equation of state of the QCD matter in the region at the neutron star core densities.

Event by event fluctuations

Event-by-event fluctuations of conserved quantities such as baryon number, strangeness and electrical charge can shed light on the properties of matter created in high-energy nuclear collisions. For example, the ratios of hadron yields, are expected to probe possible phase transitions, as shown by lattice QCD calculations [30].

Higher moments of the fluctuations (like skewness, kurtosis) are expected to be especially sensitive to location of the critical end point [31]. Existence of a critical point is expected to lead to a non-monotonic behaviour of the kurtosis times squared standard deviation ($\kappa\sigma^2$) observable [31, 32].

Up to date, there have been no higher-order event-by-event fluctuations measured at SIS100 energies, thus CBM have a great discovery potential performing precision measurements of high order fluctuations to search for QCD critical point.

Strangeness

Particles containing strange quarks are expected to be sensitive to the phase transition between hadronic and partonic phase [33–35]. The density of the expected fireball correlates with yields of strange particles. Strange quarks are expected to be produced more in the parton-parton interaction than during hadron reaction. Hence, yields of strange particles increase by the number of participating nucleons and should be higher in heavy ion collisions than in p+p collisions.

The enhancement of strange hadron yields compared to light hadrons in the partonic phase, was observed in Pb+Pb collisions at SPS at $\sqrt{s_{NN}} = 7.7 - 13.7\,\text{GeV}$ [36, 37]. It was taken as an indication of transition from a partonic to the hadronic phase [38].

These results show the importance of the strangeness production, as it provides information on process possibly sensitive to phase transition.

Lepton pairs

Di-leptons emitted in heavy ion collisions, allow to investigate the microscopic properties of strongly interacting matter [39, 40]. They are emitted during the whole evolution of the fireball and carry the information about the medium properties, because di-leptons do not interact strongly. Leptonic decay channels (muon or elec-

tron pairs) give the possibility to enable unique measurements such as: degrees of freedom of the medium, fireball lifetime, emitting source temperature.

Lepton pairs are messengers of the dense matter, because they provide a direct link to the possible chiral symmetry restoration [41].

Open and hidden charm

Particles containing charm quarks are generated in the early stage of the collision. Thus, they are sensitive to the degrees of freedom of the created matter: partonic or hadronic. Depending on their interaction with the medium, the charm and anti-charm quarks hadronize into D mesons, charmed baryons, or charmonium.

The suppression of charmonium production due to color screening is thought to be as a signature for the quark-gluon plasma [42]. The charmonium suppression was observed at RHIC [43] and LHC [44] in central Pb+Pb collisions.

Hypernuclei and strange objects

The discovery of (double-) Λ hypernuclei and determination of their lifetimes will provide information on the hyperon-nucleon and hyperon-hyperon interactions, which are essential ingredients for understanding of the nuclear matter EoS at high densities, and structure of neutron stars [45].

The CBM experiment at SIS100 will measure hydrogen and helium hypernuclei in huge amounts. According to the thermal model it is expected to collect sufficient statistics of $^3_\Lambda$H and $^4_\Lambda$He with a yields of 1.1×10^{10} and 5.2×10^8 respectively at 10 AGeV Au+Au collisions in 10 weeks of the experiment. The lifetime of hypertritium has been already measured by ALICE and STAR collaborations [46], but their result differs within 2σ, that is why CBM measurements are important to clarify this discrepancy. Up to now, there are no measurements of double hypernuclei, like $^4_{\Lambda\Lambda}$He and $^6_{\Lambda\Lambda}$He available, but it is expected to observe them during CBM campaign, although their yields are extremely low.

The experimental task of CBM is to measure all available observables in A+A and p+A collisions, as a function of collision energy and system size, with high precision and statistics. The experimental program is based on the following requirements:

- 10^5 - 10^7 Au+Au reactions/sec;

- determination of displaced vertices ($\sigma \approx 50\,\mu$m);

- fast and radiation hard detectors and front-end electronics (FEE);

- free-streaming readout electronics;

- high speed data acquisition and high performance computing for online event selection;

- time-based (4D) event reconstruction.

An overview of compressed baryonic matter physics and its theoretical concepts and predictions for important observables in the future, present and past heavy-ion collision experiments can be found in the CBM Physics Book [22] and CBM paper [26].

1.2 Facility for Antiproton and Ion Research

The future CBM experiment will be operated at the synchrotron SIS100 of the FAIR facility. FAIR is the Facility for Anti-protons and Ion Research under construction at the GSI[1] laboratory in Darmstadt, Germany. FAIR will provide a exceptional range of high-energy and high-intensity radioactive ion beams, high intensity anti-protons and high-energy heavy-ions [47]. These beams will support a broad range of science including nuclear structure, hadronic, relativistic heavy ion, plasma and atomic physics [48]. The layout of the FAIR facility is shown in Fig 1.5. The SIS-100[2] synchrotron will deliver beams of protons up to $29\,\text{GeV}$, Au ions up to $11\,A\text{GeV}$ and nuclei with $Z/A = 0.5$ up to $14\,A\text{GeV}$ with the intensity of 10^9 ions/sec.

The rich research programme of FAIR is grouped in the following experimental collaborations: APPA (Atomic, Plasma Physics and Applications [50]), CBM (Compressed Baryonic Matter experiment [51]), NuSTAR (NUclear STructure, Astrophysics and Reactions [52]), PANDA (anti-Proton ANnihilation at DArmstadt [53]). The wide program of APPA experiment will cover atomic physics, bio- and medical physics, material research and plasma physics. APPA will perform tests of fundamental interactions and symmetries as well as applications of nuclear physics in medicine and energy. The CBM experiment is designed to perform precision measurements of hadronic, leptonic and photonic probes in order to explore the QCD phase diagram in the region of high net-baryon densities. NuSTAR will investigate nuclear structure and dynamics and nuclear astrophysics. PANDA will focus on antimatter research as well as on various topics related to the weak and the strong force, exotic states of matter, and the structure of hadrons.

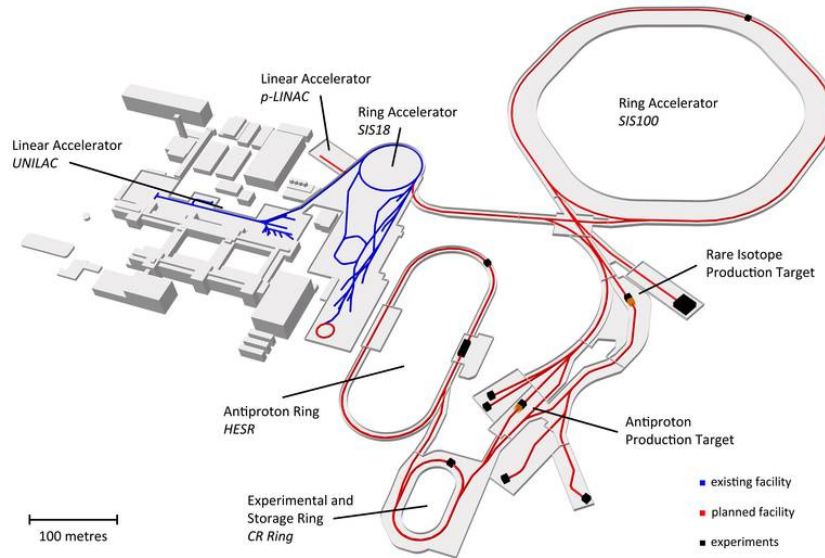[1]Gesellschaft für Schwerionenforschung
[2]Schwerionensynchrotron

Figure 1.5: Layout of the Facility for Antiproton and Ion Research complex [49].

1.3   Detectors of the CBM experiment

The detector system of the CBM experiment features a fixed target geometry accepting polar emission angles between 2.5° and 25° in order to cover the midrapidity region for symmetric collision systems at beam energies between 2 AGeV and about 40 AGeV. The CBM experimental setup consists of following systems and detectors: a superconducting magnet with the silicon spectrometer inside: the Micro Vertex Detector (MVD) and the Silicon Tracking System (STS), the Ring Imaging Cherenkov counter (RICH) for electron-hadron configuration, the Transition Radiation Detector (TRD) and the Time-of-Flight (TOF) wall. Following the tracking and particle identification detectors the forward calorimeter Projectile Spectator Detector (PSD) is placed. The CBM operation scenario assumes two modes: for electron and muon measurements. When running muon measurements, RICH will be replaced with the Muon Chambers (MuCh) detector, as it is shown in Fig. 1.6 with RICH at its parking position. A brief description of the system components is given further.

Superconducting Dipole Magnet

The superconducting dipole magnet [54] serves to bend charged particle trajectories in order to determine their momenta. The H-type magnet of the CBM experiment is designed to provide a vertical magnetic field with bending power of 1 Tm over a
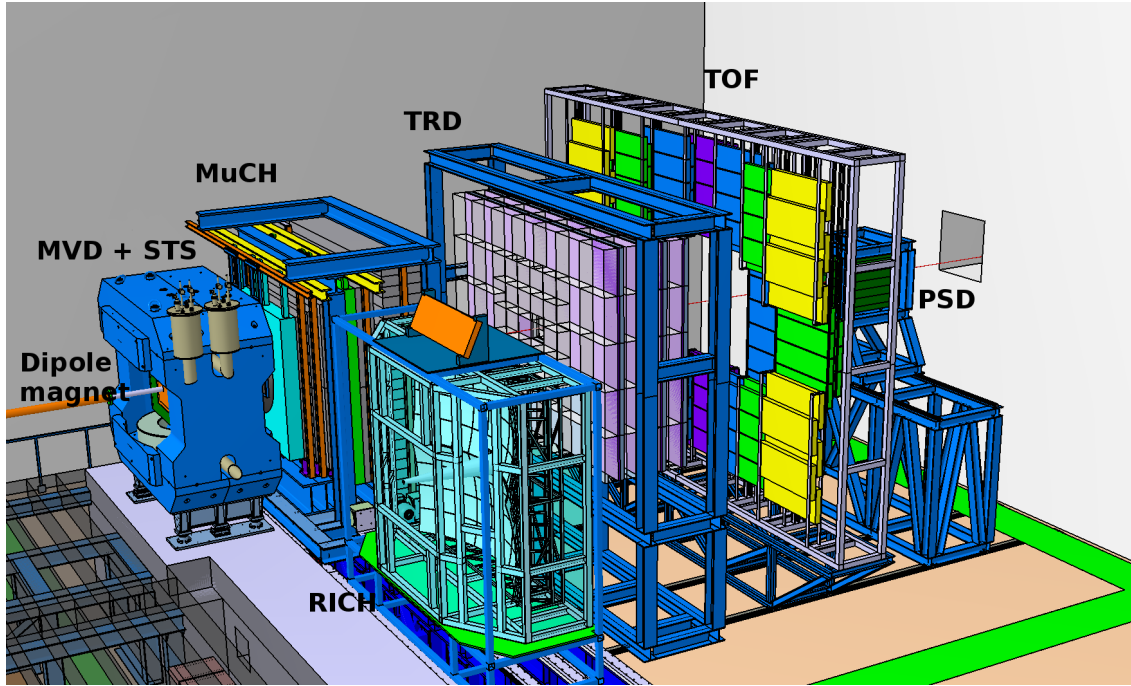
Figure 1.6: The CBM experimental setup with the muon detection system in measuring position, and Ring Imaging Cherenkov detector in parking position.

length of one meter from the target position [55]. The tracking system consisting of MVD and STS will be placed in the generated field insight the magnet, which are inserted in the magnet gap of 1.44×3 m^2.

MVD – Micro Vertex Detector

The aim of a vertex detector is to determine secondary vertices of short lived particles with accurate position resolution of $3.6 - 6\,\mu$m [56]. In order to achieve the required high resolution, the MVD is based on pixel sensors. The MVD consists of four layers of very thin silicon monolithic active pixel sensors (MAPS) with a pixel size between $25 \times 25\,\mu$m^2 to $40 \times 40\,\mu$m^2. The layers are placed at 5, 10, 15 and 20 cm downstream the target. An ultra low material budget of less than $< 0.05\%$ X_0 is foreseen in order to mitigate multiple scattering of the charged particles in the detector material. CBM will work at high rates, thus this detector has to work at high readout speed of > 30 kfps. The MVD is the closest detector to the target, therefore it has to cope with the highest radiation. According to the simulations, the expected NIEL[3] damage will be $5 \times 10^{14}\,1\,\text{MeV}\,\text{n}_{\text{eq}}\text{cm}^{-2}$, and the ionising dose around 3 MRad.

---

[3]Non-Ionising Energy Loss

STS − Silicon Tracking System

The Silicon Tracking System is intended for the reconstruction of the trajectories of charged particles produced in the interaction and the measurement of their momenta with resolution of $\sim 1.5\%$ [57]. The typical hit resolution is expected to be about $25\,\mu$m. Such a performance can only be achieved with an ultra low material budget of the stations (about 1.3% radiation length per station), within particular restrictions on the location of power-dissipating front-end electronics, which should be placed outside of an active volume.

The STS is build as an array of eight tracking stations consisting of $\sim 300\,\mu$m thick double-sided silicon micro-strip detectors based on the n substrate with $58\,\mu$m pitch, which are located downstream of the target at distances between $30\,$cm and $100\,$cm in a magnetic dipole field [22].

It is expected that the silicon microstrip sensors have to withstand a NIEL damage up to $10^{14}\,1\,$MeV $\mathrm{n_{eq}cm^{-2}}$, and an ionising dose around 11 MRad during the SIS100 operation. More design details on the STS are given in Section 1.4.

MuCh − Muon Chamber

The MUCH [58] is designed to identify muon pairs which are produced in high-energy heavy-ion collisions. An accurate muon identification will allow CBM to reconstruct rare particles, which may decay by a dimuon channel like low-mass vector mesons and J/ψ. In order to detect muons with different energies, the system for muon identification consists of a set of gaseous micropattern chambers sandwiched between hadron absorber plates made of graphite and iron. The first two stations will consist of triple Gas Electron Multiplier (GEM) detectors, the next stations will be also based on MRPC (Multigap Resistive Plate Chambers).

RICH − Ring Imaging Cherenkov Detector

The main task for RICH [59] is to identify electrons and positrons, suppress pion contamination in dielectron spectrum during the reconstruction of short-lived particles. RICH should provide a pion suppression ratio of about 500 which in combination with TRD will allow to reduce pion contamination $10^3 - 10^4$ times. RICH will be placed outside of the dipole magnet, behind the STS, about 1.6 meter downstream from the target. The detector comprises a $1.7\,$m length CO_2 radiator, glass mirrors of $6\,$mm thickness with a reflective Al+MgF$_2$ coating and a UV photon detector realized with multi-anode photomultipliers (MAPT).

TRD − Transition Radiation Detector

The TRD detector has to provide electron and positron identification with momenta p > 1.5 GeV/c, and rejection of pions by registering the produced transition radiation; particle tracking to the following TOF detector; identification of light nuclei like deutrons, triton, helium by the dE/dx method. It will be located at approximately 4 m downstream the target. The detector will be based on Multi-Wire Proportional Chambers (MWPC) in combination with a radiator. The modules will have a structure of rectangular pads with a resolution of $300 - 500$ μm across and $3 - 5$ cm along the pad [60]. In order to ensure an accurate measurements of both coordinates, every second detector layer will be rotated 90° with respect to the previous one.

TOF − Time-of-Flight Wall

The main task of the TOF wall is to identify hadrons and light nuclei produced in a collision. The TOF provides a precise measurement of time and is placed far $(6 - 10$ m$)$ from the target. Thus, having a momentum of the track determined by the STS, and time of flight measured by the TOF hit, which gives a velocity, the mass of the charged particle can be estimated. The TOF detector [61] is based on the technology of resistive plate chambers (RPC), providing a time resolution of about 60 ps, which will be assembled in a wall with an active area of about 120 m². The granularity is adapted to cope with the variation of hit rates, which range from 2 kHz/cm² at the periphery to 25 kHz/cm² in the inner sections.

ECAL − Electromagnetic Calorimeter

The main purpose of the ECAL [62] detector is the identification and the measurement of energy and position of photons and electrons. ECAL will measure spectra of photons and neutral mesons decaying in their photonic decay channels. Precise measurement of masses and widths of short-living mesons (η, $\eta^{'}$, ϕ, χ_c etc.) will shed light on the chiral symmetry restoration which is expected to occur in dense nuclear matter. It is built from individual modules that are made of lead absorber plates interleaved with scintillator tiles as active material. The calorimeter system has 4352 electronic channels, built from 1088 modules of 60×60 mm² cells. Sufficient electron/hadron separation is obtained using a sampling structure of 1.5 mm lead sheets interspersed with 2 mm thick scintillator plates, and design of the light collection by the wavelength shifting fibres.

PSD – Projectile Spectator Detector

The PSD [63] is a forward hadron calorimeter for event characterisation. The main purpose of PSD is to determine the collision centrality and orientation of the reaction plane. The detector is designed to measure the number of non-interacting nucleons from a projectile nucleus in heavy ions collisions. The PSD is a full compensating modular lead-scintillator calorimeter which provides very good and uniform energy resolution. The calorimeter comprises 44 individual modules, each consisting of 60 lead/scintillator layers with a surface of 20×20 cm^2. The scintillation light is read out via wavelength shifting (WLS) fibers by Multi-Avalanche PhotoDiodes (MAPD) with an active area of 3×3 mm^2 and a pixel density of 10^4 per mm^2.

Data Acquisition System (DAQ) and First Level Event Selection (FLES)

As it has been already mentioned, CBM will measure rare probes, which one has to reconstruct from physical events in the presence of a large background. In order to identify them, one has to reconstruct tracks with high speed and accuracy. In order to collect sufficient statistics for the analysis of rare observables, the CBM experiment has to cope with unprecedented interaction rates of up to 10 MHz.

Because of the complicated decay topology of particles like Ω hyperons or D mesons, a trigger signal can't be generated. There are no simple criteria for event triggering and selection, thus the whole event needs to be reconstructed. This would require a prohibitively long trigger latency. Therefore the data readout chain is based on a free streaming front-end electronics which delivers time-stamped signals from each detector channel without event correlation. All detector systems are equipped with self-triggered readout electronics. In this case, instead of "event building", data acquisition will produce "time-slice building", where physical events are reconstructed later by software. The data reduction is shifted entirely to software, which gives maximum flexibility w.r.t. physics [64].

The full reconstruction of the collision is required already at the selection stage and will be run in the online mode [22]. The First-Level Event Selector is a dedicated computing farm intended to reduce on-line the raw data volume by up to three orders of magnitude to a recordable rate, which will be able to reconstruct online the full event topology including long-lived charged and short-lived particles [65]. The basis for the online event selection will be fast algorithms. Based on the reconstructed signals the collisions of interest will be stored on tape.

1.4 The Silicon Tracking System

The work is focused on the study of the double-sided silicon microstrip sensors within the STS project, therefore more a detailed description of the Silicon Tracking System is provided below.

STS is intended to reconstruct tracks of charged particles in the magnetic field and to determine their momentum with high precision. For this, it will be installed inside the dipole magnet of about 1 Tm bending power. STS will consist of 8 tracking stations, constructed of modules based on $\sim 300~\mu$m double-sided silicon microstrip sensors, which will be placed on a low mass carbon fibre support structure. In Fig. 1.7, the CAD model of the STS structure presented together with the system installed inside the magnet.
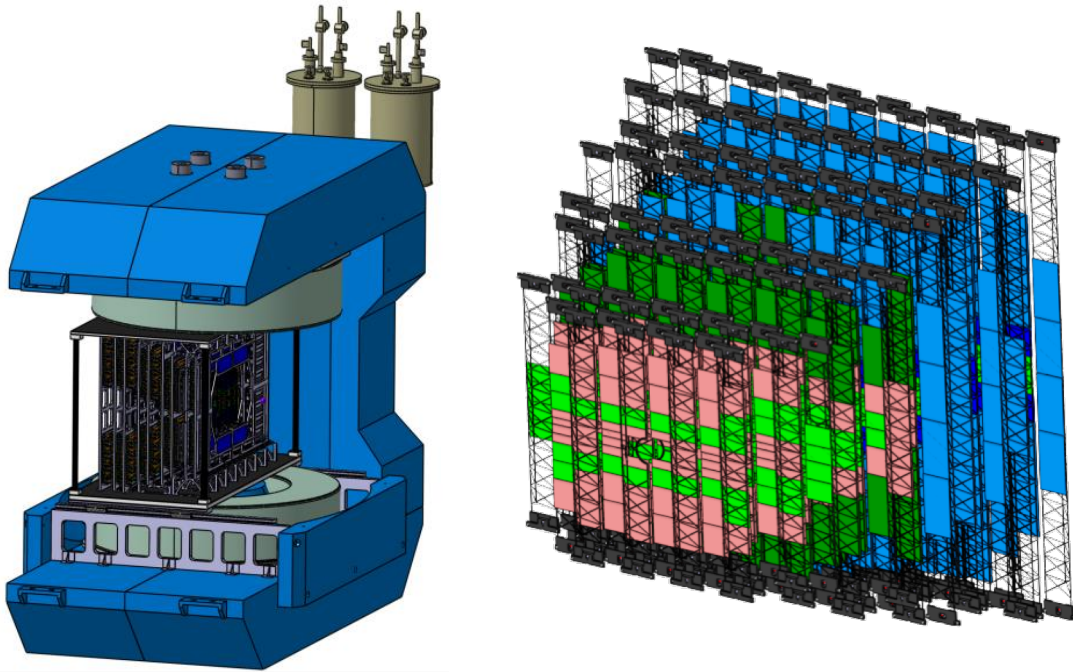
Figure 1.7: View of the Silicon Tracking System inside of the dipole magnet (left) & without thermal enclosure and services (right) [66].

In order to meet the CBM needs, the main tracker should be fast, thin, radiation hard, comprise adequate number of readout channels and it has to fulfil the following requirements:

- operating with a track multiplicity up to 700 per central Au+Au collision (in the STS acceptance);

- acceptance in polar angle $2.5° < \theta < 25°$;

- high track reconstruction efficiency of $\approx 95\%$ for tracks at p $> 1\,\text{GeV}/c$;

- momentum resolution of $\Delta\text{p}/\text{p} \approx 1.5\%$ over a wide range from $0.1\,\text{GeV}/c$ to $12\,\text{GeV}/c$;

- a single-hit resolution of about $20\,\mu\text{m}$ in X direction and $120\,\mu\text{m}$ in Y;

- time resolution of $5\,\text{ns}$;

- radiation hardness $10^{13}\,1\,\text{MeV}\,\text{n}_{\text{eq}}\text{cm}^{-2}$ (innermost region of stations) during SIS100 operation and $10^{14}\,1\,\text{MeV}\,\text{n}_{\text{eq}}\text{cm}^{-2}$ at SIS300.

Double-sided silicon microstrip sensors

The momentum resolution required for physics observables is constrained by multiple scattering. Low material budget guarantees less multiple scattering, hereby sensors have to be thin, but produce a sufficiently high signal. Thus, the STS is based on double-sided sensors of n-type silicon produced on standard float-zone silicon wafers of $2 \div 6\,\text{k}\Omega\cdot\text{cm}$ resistivity and sensors of 285 ± 15 or $320 \pm 15\,\mu\text{m}$ thickness (depending on vendor). During the R&D phase, prototypes from Hamamatsu Photonics K.K (later referred as HPK), Japan and CiS Forschungsinstitut für Mikrosensorik GmbH (later labeled as CiS), Germany were tested.
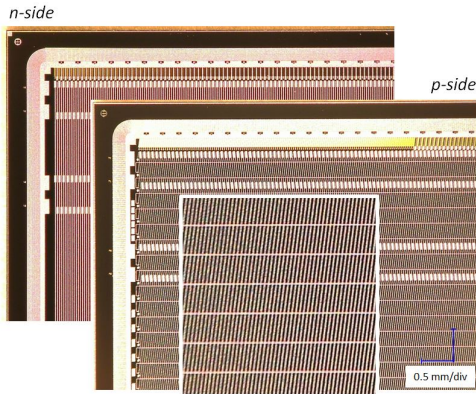
Figure 1.8: Close-up view of microstrip sensor, showing the strip segmentation on two sensor sides, the double-metal routing lines (magnified) and sensor edge structures including guard rings.
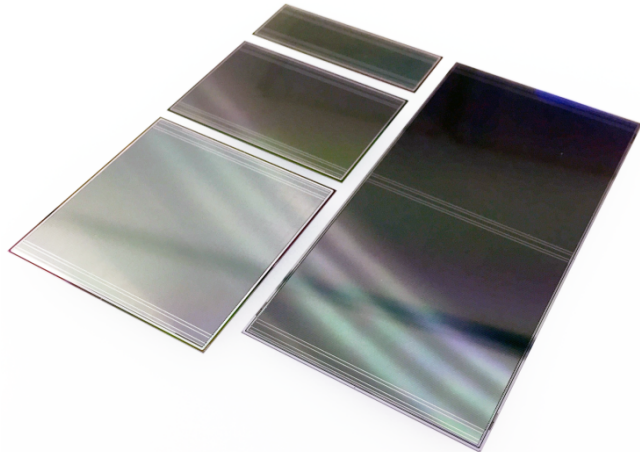
Figure 1.9: Silicon micro-strip sensors for the CBM Silicon Tracking System produced in different form factors: 62×22, 62×42, 62×62, $62 \times 122\,\text{mm}^2$.

Different sizes of sensors are foreseen to cover an area close to the beam pipe and periphery. Sensors in of four different sizes are shown on Fig. 1.9, they all have the

same width 6.2 cm, but different length of 2.2, 4.2, 6.2 and 12.4 cm. The smaller sensors will be placed in the inner region of the stations, close to the beam pipe. The outer region will be covered with large sensors. Thus, sensor length will match the hit occupancy that decreases towards the periphery of the station. Each prototype comprises 1024 strips per side with 58 μm pitch. In order to decrease the level of fake hits, there is a stereo angle between the strips on the p- and n-side. On the other hand, this leads to the fact that one coordinate is measured with better precision than the other. In our case, it is important to measure X with good accuracy, since the field is directed along Y and, as a result, the quality of momentum measurement is sensitive to X. After optimization, an angle of 7.5° of p-side strips with respect to the n-side (see Fig. 1.8) was chosen.

In this case, short strips occur at the edges of the p-side. They are interconnected via a double metallisation layer. This kind of Z-connection allows to read out the entire sensor from one edge, thus making it compatible with the STS detector module structure and for the formation of "ladders" out of them.

The sensor strips are connected to a common bias ring and biased via polysilicon resistors with a resistance $\sim 1\,\mathrm{M}\Omega$ s to bias individual sensor strips. Two pairs of AC pads are implemented at both ends of the readout strips. Also there is a set of (for CiS) or one wide (for HPK) guard ring implemented in the outer part of sensor, to suppress surface currents and to gradually reduce the electric field in the edge area. The strips on the n-side are isolated with the p-spray technique.

The sensors will feature integrated AC-coupling in order to avoid the need of the leakage current compensation circuitry in the front-end electronics.

Readout

The STS task requires a new readout ASIC, which has to provide timing and energy information for each incoming signal, it has to be fast and works in selftriggering mode in order to avoid pile-up of events. For this, a 128 channels STS-XYTER (STS X and Y coordinate, Time and Energy Read-out chip) chip was designed and developed [67], photo is shown in Fig. 1.10. The block diagram of the chip is shown in Fig. 1.11. Here, the input current pulse from the detector is processed by the charge sensitive amplifier (CSA). The signal path is then split into a fast and a slow branch [68]. The fast branch includes a fast shaper with a shaping time of 30 ns, a discriminator and a timestamp latch. It is optimized to provide good timing resolution of < 10 ns. The slow branch consists of a slow shaper with the typical shaping time of 80 ns, a 5-bit flash ADC and a digital peak detection logic.

To achieve the desired track reconstruction efficiency, hits should be processed with Equivalent Noise Charge (ENC) of about 1000 e- rms and the processing chain
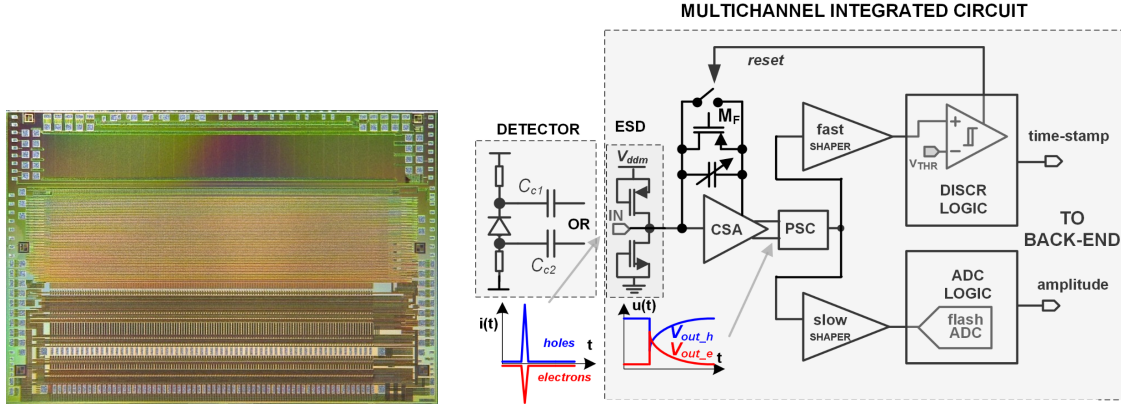
Figure 1.10: Photo of the STS-XYTER v.1 chip.

Figure 1.11: Block diagram of the STS-XYTER chip.

should be able to handle an average input hit rate of $250\,\mathrm{kHz}$/channel.

Radiation load of STS

The end-of-life fluence of $10^{14}\,1\,\mathrm{MeV}\,\mathrm{n_{eq}cm^{-2}}$ is expected to be received by $5-10\%$ of the sensors in the innermost region of STS after about 10 months of Au beam of $E_k = 10\,A\mathrm{GeV}$ colliding with Au target at $10\,\mathrm{MHz}$ interaction rate. Considering that a substantial part of the CBM physics programme will be carried out with lower interaction rates, smaller collision systems and, in the first years, at the lower beam energies of SIS100, this corresponds to at least five years of operation [57].

Table 1.1: Maximum values of the ionising dose and fluence deposited in the STS, after two months of Au+Au collisions at $10\,\mathrm{MHz}$ interaction rate [57].

Operation conditions	Fluence, $1\,\mathrm{MeV}\,\mathrm{n_{eq}cm^{-2}}$	Ionising dose, Gy
$E_k = 10\,A\mathrm{GeV}$ (SIS100)	0.2×10^{14}	1.2×10^4

The non-ionising energy loss and ionising dose (XY cross-sections corresponding to Z positions of STS stations) for the $2\,A\mathrm{GeV}$ Au beam and Au target are shown in Fig. 1.12-1.13 [69]. For this simulation passive material was not taken into account, thus, δ-electrons are produced in a big amount from backscattering at the muon setup.

After introducing passive materials (like supporting structure, cables, services), level of NIEL at last stations will significantly decrease. One can see in Fig. 1.13 the reduction of ionising dose with an increasing distance from the target, both downstream and upstream.
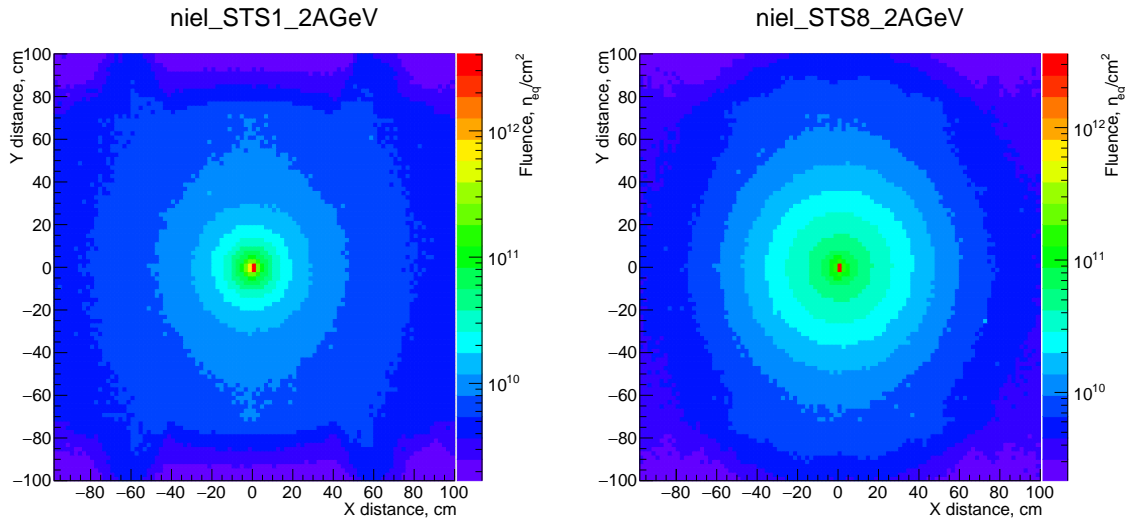
Figure 1.12: FLUKA calculations of non-ionising energy loss (top) at 1st (left) and 8th (right) STS stations for $2\,A$GeV 10 MHz Au+Au collisions at SIS100 [69].
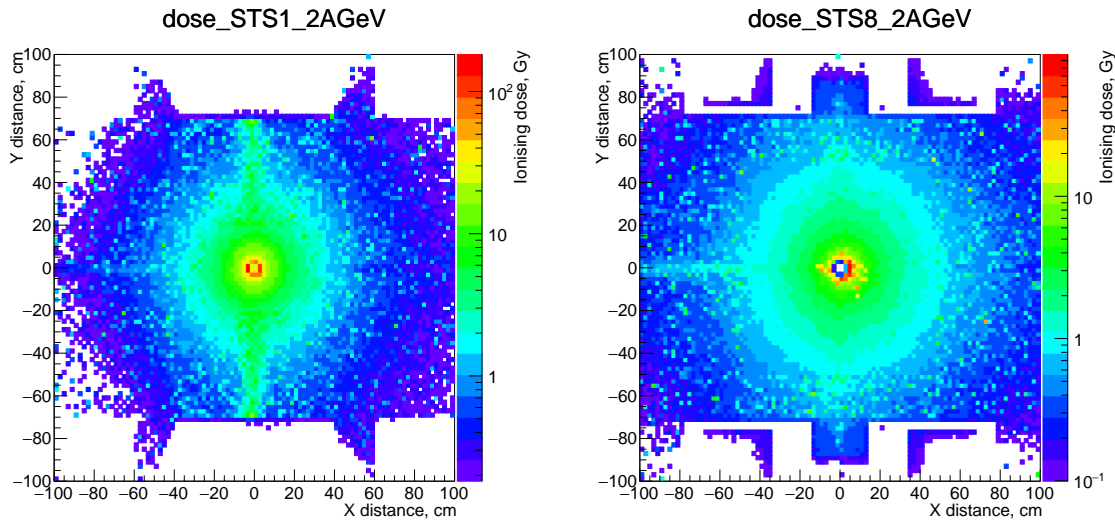
Figure 1.13: FLUKA calculations of ionising dose at 1st (left) and 8th (right) STS stations of 2 month $2\,A$GeV 10 MHz Au+Au collisions at SIS100 [69].

As an alternative to FLUKA simulations, the radiation dose estimation was also obtained with transport simulations within the standard CBM software environment `CBMRoot` which employs the GEANT3 package for the particle-mater interactions. For this study, the actual hits of the particle trajectories in the sensitive volumes were used. The calculations were done for minimum-bias Au+Au collisions at $10\,A$GeV, using the actual STS geometry. Here, nor δ-electrons were taken into account, neither fragments were produced. The obtained values are normalised to 5×10^{13}

events, which corresponds to one effective month of running at 10 MHz [70].
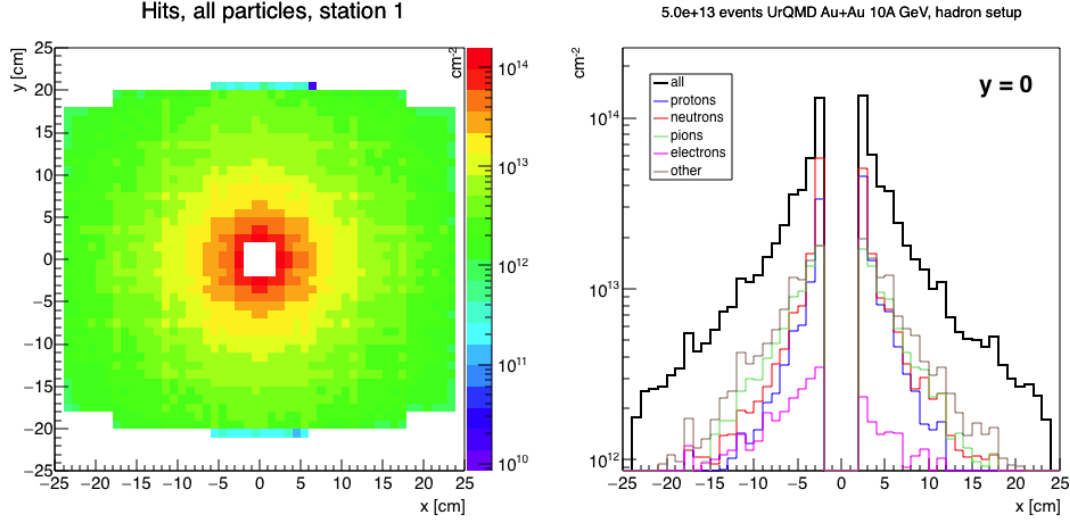
Figure 1.14: CBMRoot simulation results using the GEANT3 transport engine for hit rates at 1st STS station for 10 AGeV Au+Au collisions at SIS100.

Both simulation approaches mentioned above provide values which are in a good agreement with each other. Thus we use 1×10^{14} 1 MeV n_{eq}cm^{-2} as a conservative limit for the lifetime fluence of the silicon micro-strip sensors of STS.

Cooling

During operation of the STS detector system, the thermal power of about 50 kW will be generated, where the FEB-electronics is the main contributor to the total amount (about 40 kW), heavily irradiated sensors will generate < 6 mW/cm^2, low voltage power cables and heat through the walls of an insulation box will create additional heat of 10 kW. The increase of temperature leads to increase of the leakage current in the silicon microstrip sensors, which sequentially bring to the increase of the shot noise, because it proportional to $\sqrt{I_{leak}}$. Also, with irradiation, leakage current increases proportionally to the obtained dose. Thus, the excess of heat can cause the thermal runaway of the whole detector. During the experiment, when the system is under the influence of radiation, the operating temperature of silicon causes both beneficial annealing and worsens reverse annealing, which results in increasing of the full depletion voltage of the sensor. Its effect is seen in the development of the effective doping concentration and the full depletion voltage.

That is why all generated heat has to be constantly cooled away and silicon sensors have to be operated at low temperatures. To avoid reversal annealing of irradiated sensors and decrease leakage current during operation, they have to be kept at

temperature below -7°C in a dry nitrogen atmosphere to prevent condensation. The cooling of the STS involves two different cooling systems: a bi-phase CO_2 system to remove the power dissipated by the front-end readout electronics and gas cooling to remove the heat produced by the sensors themselves in acceptance region.

Material budget

The STS tracker is required to have a low material budget in order to minimize multiple Coloumb scattering and achieve high momentum resolution $\sim 1.5\%$. To reduce amount of material in the active volume, the readout electronics will be placed outside of the detector aperture.

Signals from sensors will be transferred by microcables to readout chips and later to the data acquisition system. The microcables are realized on a polyimide substrate with aluminium traces with spacers in between and additional shielding layers on the outside. The thickness of aluminium is 14 μm and of polyimide is 10 μm, respectively. Such a cable structure for one module corresponds to 0.23% X_0 equivalent to 213 μm of silicon. The module support structures are made of low-Z material carbon fiber.
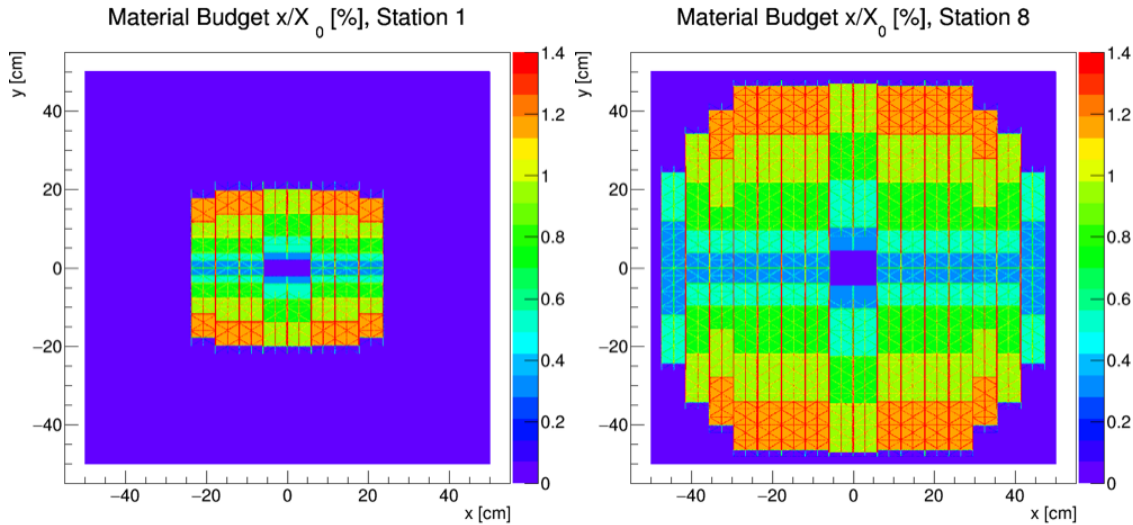
Figure 1.15: Material budget distribution in X_0 units (radiation length) for first (left) and eighth (right) STS tracking stations including supporting structures and micro-cabels.

The distribution of material budget is shown in Fig. 1.15. In this case, the material budget is vary from 0.3% X_0 to 1.3% X_0 per tracking station in the acceptance region. One can see that it is low in the center of the station, where the track density is the highest, but due to the stuck of microcables, it increases towards the periphery.

System integration

In total, the STS will consist of 896 detector modules, which will be installed onto 106 carbon-fiber support structures. A detector module (see Fig. 1.16) is defined as an assembly of a single sensor and two front-end boards with eight chips per side each connected with a set of stacked low-mass polyimide-aluminium readout microcables (32 per sensor in total).

Figure 1.16: Module assembly: 1024 sensor channels of $62 \times 62 \, \mathrm{mm}^2$ sensor connected via $50 \, \mathrm{cm}$ long micro-cables to 16 ASICs placed on two FEBs (frond-end-board) for the p- and n-side.

The STS will comprise modules of 23 different types, in different sensor sizes (strip length) and microcable length (distance between sensor and front-end electronics). Up to ten modules are arranged on a carbon fiber support structure forming a ladder. The modules are mounted on carbon fiber ladders (see Fig. 1.17), the readout directions oriented towards either the top and or the bottom part of the STS. The ladders will be mounted on a C-frame to form half of a tracking station. A station will be built from half-stations.

Figure 1.17: Example of the ladder made of carbon fiber and sensors attached to it: two of $62 \times 62 \, \mathrm{mm}^2$ and three sensors of $62 \times 122 \, \mathrm{mm}^2$ size. Microstrip cables are placed underneath.

Physics performance of the STS

The track finding in the STS detector system, operated in an inhomogeneous magnetic field, is based on the Cellular Automaton method [71]. Track and vertex fitting

is done using a procedure based on a Kalman filter [72, 73]. The track reconstruction efficiency and momentum resolution of charged particles as a function of particle momentum and polar angle are depicted in Fig. 1.18.

(a)

(b)

(c)
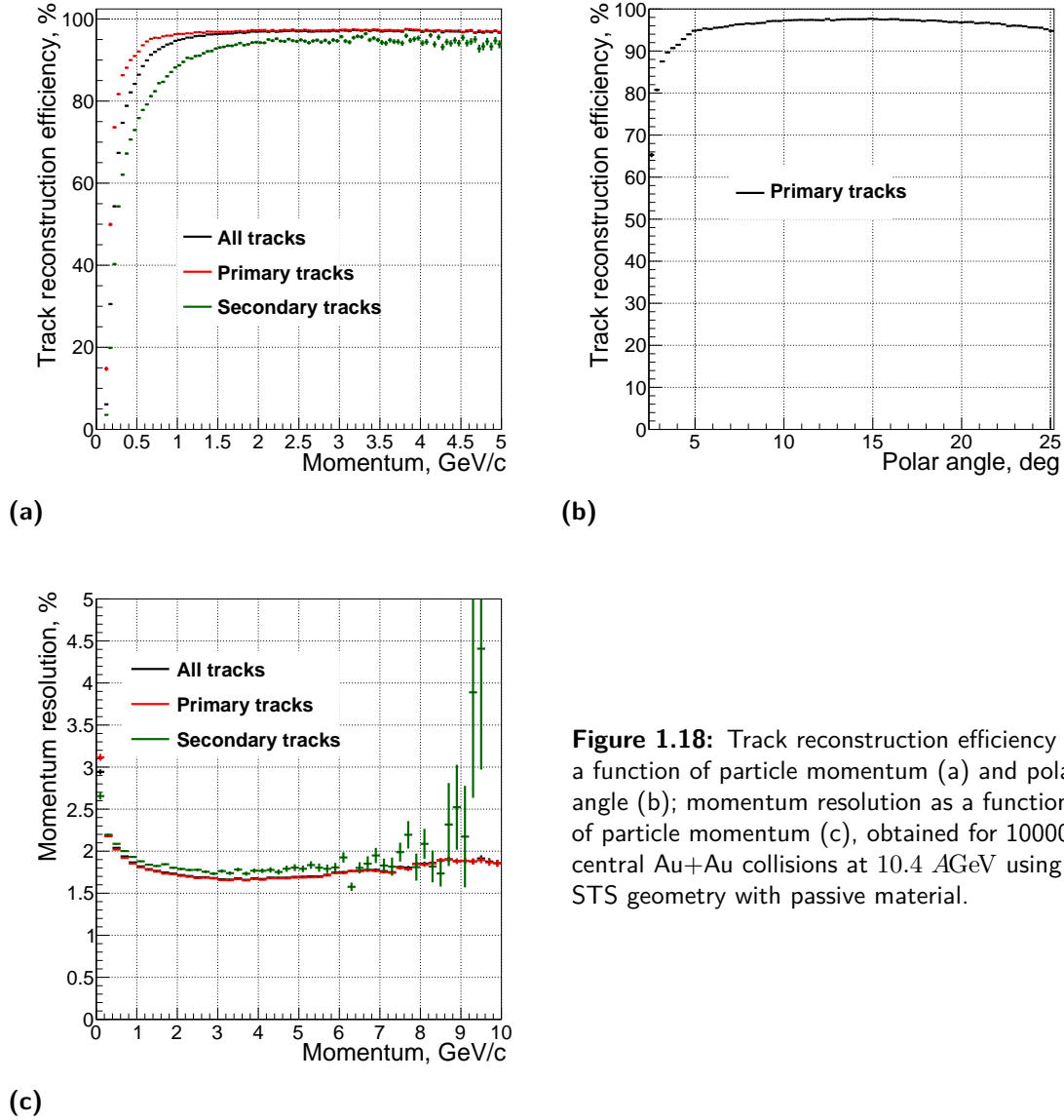
Figure 1.18: Track reconstruction efficiency as a function of particle momentum (a) and polar angle (b); momentum resolution as a function of particle momentum (c), obtained for 10000 central Au+Au collisions at 10.4 AGeV using STS geometry with passive material.

By definition, a track is considered reconstructible if it intersects the sensitive regions of at least four stations. A reference track should have a momentum greater than 1 GeV/c, which have certain physical importance. The reference set of tracks can also include tracks of particular physics interest: secondary tracks from interested decays; primary tracks coming from the target region. The track reconstruction efficiency for primary tracks reaches a plateau of 97% after 1 GeV/c, and for

secondary is about 95% after 2 GeV/c. The momentum resolution is below 2% over a wide range. As a function of the polar angle, i.e. the emission angle of the particle with respect to the beam direction, the efficiency varies between 90% and 98% level. In the case of all considered tracks, the track reconstruction efficiency is more than 95%, which meets the design requirements. The drop of the efficiency at momentum lower than 1 GeV/c is mainly caused by the low number of measurements (charged particle crossed less than 4 stations) and high impact of the multiple scattering.

2

Radiation damage effects of silicon microstrip sensors

Semiconductors are often used for the production of position sensitive detectors not only for nuclear and particle physics, but also in satellite experiments and industrial applications (medicine, biology, security). The most commonly used semiconductor detector materials are silicon (Si), germanium (Ge) and diamond. Germanium detectors are mainly used in nuclear physics, they have a small band gap of $0.66\,\mathrm{eV}$, so as to keep the leakage current minimum, they require constant cooling. Diamond detectors have a large band gap of $5.5\,\mathrm{eV}$, and are radiation hard, but they are very expensive to be manufactured in large volumes. The silicon detectors are usually represented as pixel and microstrip detectors, they have a moderate band gap of $1.12\,\mathrm{eV}$ and can be operated at room temperature. Particularly, silicon pixel detectors are mainly used for vertex reconstruction in a presence of high tracking density. Due to their high cost per volume, further tracking in large size area mainly utilizes of strip sensors.

Silicon detectors are applied for measuring the position of charged particles. With the help of track reconstruction software, it is also possible to deduce the momentum of the particle through the curvature in a magnetic field, the vertex of the interaction and, if the particle has a long lifetime, a decay vertex, called a secondary vertex.

The detection of minimum ionizing particles (MIP) is based on ionisation or ex-

citation of atoms in the medium caused by the passage of charged particles. The energy required to create an electron-hole (e-h) pair in Si is 3.6 eV yielding an ionization of about 80 e⁻h/μm.

2.1 Operation principle of silicon strip sensors

The mean value of the energy lost by a charged particle in a medium is described by the Bethe-Bloch formula [74]:

$$-\frac{dE}{dx} = 4\pi N_A r_e^2 m_e c^2 z^2 \frac{Z}{A} \frac{1}{\beta^2} \left[\frac{1}{2} \ln \frac{2m_e c^2 \beta^2 \gamma^2 T_{max}}{I^2} - \beta^2 - \frac{\delta(\gamma)}{2} \right] \qquad (2.1)$$

where z is the charge of an incident particle in elementary charge units, T_{max} is the maximum kinetic energy that can be imparted to a free electron in a single collision, I is the mean excitation energy, Z is the atomic number, A is the atomic mass, N_a is the Avogadro constant, m_e is the electron mass, c is the speed of light, r_e is the classical electron radius, $\gamma = \sqrt{1 - \beta^2}$ is the Lorentz factor, and δ is the density effect correction.

Signals are generated whenever electrons are excited into the conduction band leaving holes in the valence band. These free electrons and holes may then induce a measurable signal. Such an excitation can happen either by absorption of photons or by ionization of charged particles. Hence both types of radiation can be detected with silicon sensors. In order to separate electrons and holes and detect them, one can structure silicon in suitable way. Due to the applied field, the e-h pairs travel separately to the electrodes on the sensor surfaces. The silicon sensor can be internally segmented into independent p-n junction regions (strips). This allows to determine the position of the initial interaction. The implants can be coupled via internal capacitance to the aluminium readout strips. The latter are connected to the readout electronics, where the intrinsic signal is amplified and shaped. In the case of segmented p-strip implants in the n-bulk silicon material, holes are collected at the p-strips. The operation principle of the n-bulk sensor and its structure is shown in Fig. 2.1.

To establish an electric field, a potential is applied between the electrodes to accelerate the charge carriers. The velocity of carriers at a defined position x depends on the local electric field $E(x)$:

$$\vec{v} = \mu \vec{E}(x), v_e = \mu_e E, v_h = \mu_h E \qquad (2.2)$$

where μ is the mobility of charge carriers, μ_e is the mobility of electrons, μ_h is the

mobility of holes. For example, in Si the mobility of holes $\mu_h = 450 \text{V/cm} \cdot \text{s}^2$ is lower than for electrons $\mu_e = 1350 \text{V/cm} \cdot \text{s}^2$, thus, at the same average electric fields, the traversing of holes through the sensor will take three times longer.
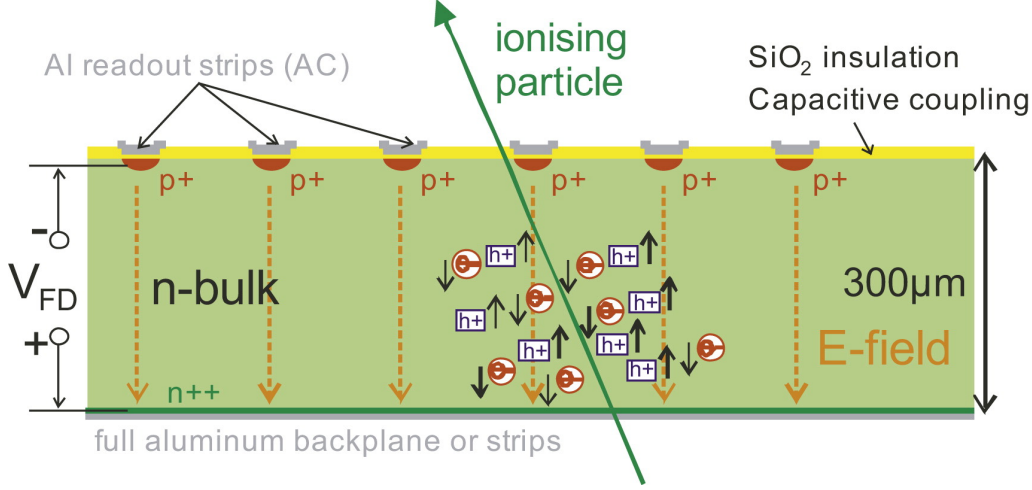
Figure 2.1: Structure and operation principle of an AC-coupled silicon micro-strip detector [75].

The position of the ionising particle is measured by weighting the signal amplitude in neighbouring activated strips. In order to use the full sensor depth as an active volume for the e-h creation, the sensor should be fully depleted. Usually, depletion is created by applying reverse bias voltage across the p-n junction. The width of the space-charge region increases as the square root of the applied voltage:

$$d = \sqrt{\frac{2\varepsilon\varepsilon_0 V_{fd}}{qN_d}} \tag{2.3}$$

where d is the width of the depletion region, ε_0 is the permittivity of vacuum, ε is the relative permittivity of Si, V_{fd} is the full depletion voltage, q is the elementary charge and N_d is the doping concentration.

The minimal value of the energy loss is expected around $\gamma\beta \simeq 3$. The detector has to be designed to detect Minimum Ionizing Particles (MIPs) with the minimum deposited energy, i.e., the noise level must be significantly lower than the resulting number of the induced e-h pairs. Both the number of collisions in a finite medium and the energy transfer per scattering vary. The first effect can be described by the Poisson distribution, while the second is described by a straggling function first deduced by Landau. In some rare cases, the energy transfer to the electron is much higher than the average; such energetic scattered electrons are called delta-electrons. These δ-electrons are responsible for the asymmetric long tail (see Fig. 1.13) towards

high energy deposition. Overall, the most probable value of the energy transfer is about 30% lower than the mean value. For silicon, the average energy used for the creation of one electron–hole pair at room temperature is 3.66 eV, about three times larger than the band gap ($E_g = 1.12$ eV). For a MIP, the most probable number of electron–hole pairs generated in 1 μm of Si crystal is about 80 e-h, i.e., 24k e-h pairs in 300 μm of silicon.

The production of double-sided silicon sensors require a sophisticated manufacturing process. Additional complication occurs due to the double-metal routing line on the junction side (p-side), which crosses all strips to read out signals from only one sensor edge per side and to avoid the non-readable corner strips, if there is a stereoangle between strips on the both sides.

Double-sided silicon microstrip detectors (DSSD) typically include integrated coupling capacitors and polysilicon resistors. The internal/integrated coupling capacitance of the strip is created by a thin oxide layer between the implantation and metallization. The biasing resistor is made of p-doped polysilicon; such kind of material is known for its radiation hardness and uniformity [76]. The AC-coupled readout prevents the direct current to flow into the readout electronics [74]. The p-stops are designed to prevent electrical short of n-side strips due to an electron accumulation layer [77] at the Si–SiO$_2$ interface.

2.2 NIEL hypothesis

The NIEL (Non-Ionising Energy Loss) hypothesis suggests a way of unification of the experimental data of radiation studies. The non-ionising energy loss scaling allows to judge about the global effect on the bulk, regardless of the energy spectrum and the type of radiation. It is assumed, that the volume damage effects in any material scale linearly with the amount of energy deposited via the crystal lattice displacements. This relation between energy deposition and damage induced changes of the material is referred to as the NIEL-scaling hypothesis [78].

With the NIEL scaling, an effective dose can be expressed in terms of 1 MeV equivalent neutron fluence which produces the same damage as an arbitrary radiation field with a certain spectral distribution $\phi(E)$ and of fluence Φ:

$$\Phi_{\text{eq}}^{1\,\text{MeV}} = \kappa \Phi = \kappa \int \Phi(E) dE \tag{2.4}$$

κ is a hardness parameter and is defined as:

$$\kappa = \frac{EDK}{EDK(1\,MeV)} \tag{2.5}$$

with EDK [1] the energy spectrum averaged displacement KERMA [2]

$$EDK = \frac{\int D(E)\phi(E)dE}{\int \phi(E)dE} \tag{2.6}$$

where $\phi(E)$ is the differential flux and

$$D(E) = \sum_k \sigma_k(E) \cdot \int_{E_d}^{E_R^{max}} f_k(E, E_R)P(E_R)dE_R \tag{2.7}$$

is the displacement KERMA or the damage function for the energy E of the incident particle, σ_k is the cross section for the reaction k, $f_k(E, E_R)$ is the probability of the incident particle to produce a recoil of energy E_R in reaction k, and $P(E_R)$ the partition function (the part of the recoil energy deposited in displacements). The hardness factor integrates $D(E)$ over the whole energy range and scales it to the equivalent displacement damage cross section of monoenergetic 1 MeV neutrons. $EDK(1 \text{ MeV}) = 95 \text{ MeV mb}$ [79].

Figure 2.2 represents the displacement damage functions depending on the incident energy calculated for the different particle types.
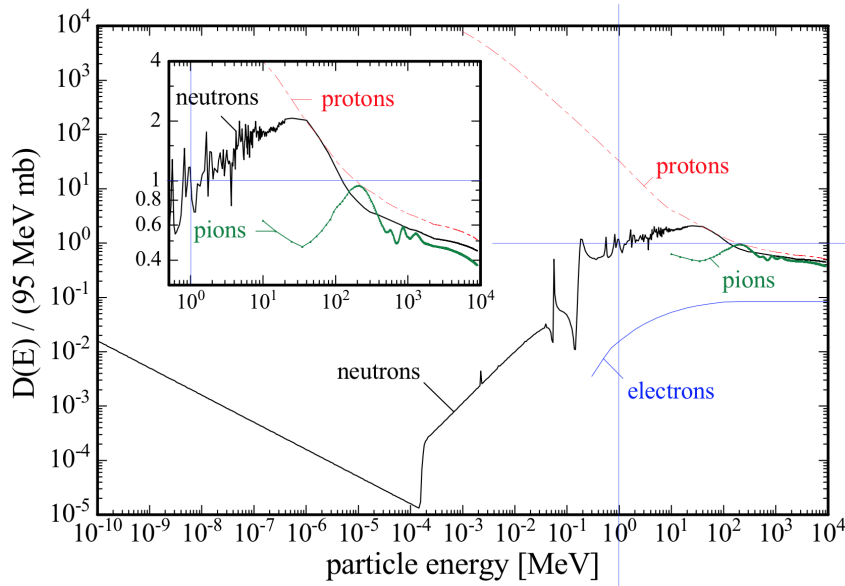
Figure 2.2: Displacement energy cross section for different particle types as a function of energy, normalised to 1 MeV neutrons [80].

---

[1]energy spectrum averaged value

[2]Kinetic Energy Released to MAtter – measures the amount of energy that is transferred from photons to electrons per unit mass at a certain position.

2.3 Damage mechanisms

During its lifetime, the STS detector will be exposed to a radiation field equivalent up to 10^{14} 1 MeV $n_{eq}cm^{-2}$ and to ionizing doses of up to 11.4 kGy [57], which will deteriorate the detector performance. Silicon devices (semiconductors in general) are affected by the following mechanisms of radiation induced damage: [81]:

- Displacement damage (caused by the non-ionising energy loss): The incident radiation displaces silicon atoms from their lattice sites. The resulting defects alter the electrical characteristics of the Si crystal.

- Ionisation damage: The energy deposited by ionisation in insulating layers, usually SiO_2, liberates charge carriers, which diffuse or drift to other locations where they are trapped. This leads to unintended concentrations of charge and, as a consequence, parasitic electrical fields.

2.3.1 Displacement damage

Particles crossing the volume of the silicon sensor can cause displacement damage by kicking silicon atoms out of the crystal lattice nodes. The rate of defects, resulting from nuclear reactions, is more than two orders of magnitude lower compare to defects originating from displaced silicon atoms and is thus negligible [82]. The bulk damage produced by hadrons and high energy leptons is caused primarily by displacing an atom (*called primary knock on atom, PKA*) out of its lattice site resulting in a silicon interstitial and a left over a vacancy (a *Frenkel pair*). At temperatures above 150 K, both the interstitials and the vacancies are very mobile and can migrate through the lattice [80]. Due to this, many of the produced Frenkel pairs will annihilate and therefore will not contribute to permanent damage. The remaining interstitials loose the energy along the path with the ionisation and displacement of the silicon atoms. Finally, both interstitials and vacancies with high probability will form a *point-like defects* (if energy of the incident particle > 25 eV) with impurity atoms being resident in the silicon lattice. If the recoil energy of an interstitial is high enough ($E_k > 5$ keV), it will not only give rise to point defects, but at the end of the path will form a dense agglomeration of defects called *clusters*. An example of the cascade of displaced atoms produced by recoil atom is presented in Fig. 2.3, where it produces a cascade with a lot of interactions, some of them stop in a terminal cluster.

Both point defects and clusters contribute to the bulk damage whereas ionisation losses will not cause any relevant changes in the silicon lattice [80].
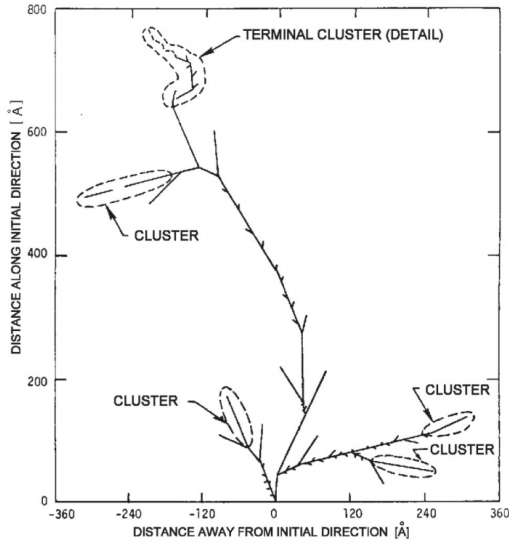
Figure 2.3: Monte Carlo simulation of a cascade caused by a recoil atom with initial energy of E_R = 50 keV. [83].
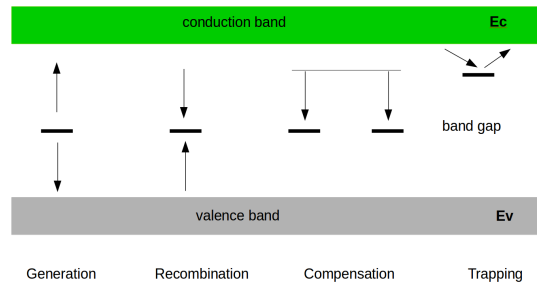
Figure 2.4: Main types of processes in the band gap (left to right): generation of the e^-h pairs, when energy of the defect close to mid-gap; re-combination of electron and hole, which reduces amount of free carriers; compensation of the doping effect, when defects act as acceptors or donors; trapping, when defects catch charge carriers. The arrows indicate the direction of electron and hole conversion.

Figure 2.4 shows the main ways the lattice defects affect the energy level distribution in semiconductors. The probabilities of these processes and of the population of defect levels can be calculated with the help of Fermi-Dirac statistics in thermal equilibrium. But the population of traps in the band gap by electrons or holes can be described by Shockley-Read-Hall statistic process [84], as an interaction of the defect level with the conduction and valence band. The above-mentioned processes caused by defects in the band gap result in the radiation-induced change of the macroscopic detector parameters, which will be discussed in Sec. 2.5.

2.3.2 Ionising damage

A signal in a semiconductor detector is formed when an ionising particle passes through a crystal and creates e-h pairs, which then drift in the electric field inducing a current pulse on electrodes. An exposure of the detector to ionising radiation causes also the build up of trapped charge in its oxide layers. The e-h pairs created in the oxide either recombine or move in the oxide electric field: the electrons towards the SiO_2-Si interface, the holes towards the metallic contact (depending on the voltage applied to the electrode). The more mobile electrons may escape from the recombination, and are injected into the silicon bulk, within a typical time of $\sim 10\,\mathrm{ps}$, the less mobile holes can be trapped at the SiO_2-Si interface. This trapping results in an increase of the oxide positive charge [85], and, therefore, in a degradation of

the oxide quality. In addition to the trapped charge, the ionising radiation also produces new energy levels in the band gap at the SiO_2-Si interface. These levels can be occupied by electrons or holes, depending on the position of the Fermi level at the interface [83], and the corresponding charge can be added or subtracted to the oxide charge.

The primary radiation damage depends on the absorbed energy, the effect of this dose depends on the rate of irradiation, the applied voltages, and their variation in time, the temperature, and the fluctuations of the radiation field itself. Ionising damage manifests itself mostly in MOS (Metal Oxide Semiconductor) field transistors [81].

In Ref. [86], the main electrical characteristics were studied after irradiation of silicon strip sensors by ^{60}Co. According to these studies, ionizing radiation damage leads to a decrease of the breakdown voltage, and to an increase of the surface current due to the reasons discussed above.

Due to fast recombination of charge carriers, the ionizing energy loss does not lead to bulk damage. The discussion of deffects of the radiation on the oxide and the surface damage are beyond the scope of this work.

2.4   Classification of defects

The interaction of high energy particles with the detector medium induces microscopic defects in the detector bulk [74]. The type of defects depends on the sort of the incident radiation. Many defects are point type lattice defects, well characterized both by experimental techniques and theoretical methods. Another type of defects, usually called cluster or extended defects, are disordered regions of material resulting from multiple interactions of high energy particle with material atoms along its track. In Fig. 2.5, one can see the simulated distribution of the vacancies in $1\,\mu m^3$ after the particle fluence of $10^{14}\,cm^{-2}$.

Several methods have been developed in order to determine cluster or point defects. Among them, TSC (Thermally Stimulated Current) defect spectroscopy technique is usually applied. The method is based on SRH (Shockley-Read-Hall) statistics, which assumes that the ionisation energy of the defects in a cluster depends on the fraction of occupied traps. The difference of ionisation energy of an isolated point defect and a fully occupied cluster (ΔE_a) could be extracted from the TSC data [88].
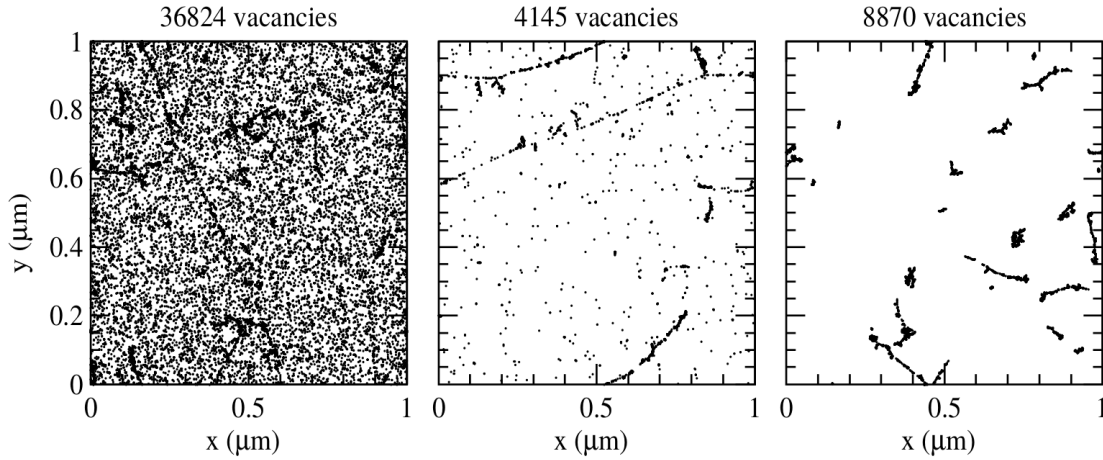
Figure 2.5: Distribution of vacancies after irradiation with $10\,\text{MeV}$ protons (left), $24\,\text{GeV}$ protons (middle) and 1 MeV neutrons (right). The simulation is a projection of over 1 μm of depth (z) and corresponds to a fluence of $\Phi = 10^{14}$ cm^{-2} [87].

2.4.1 Point defects

The primary defects, i.e., interstitials and vacancies, are mobile and react with each other or with impurities in the Si lattice, thus creating secondary defects or complex defects. In Figure 2.6 possible defect configurations are shown. Usually, single vacancies, interstitials, di-vacancies, di-interstitials combined with impurities are recognised as point defects. These defects could be also impurities from the sensor fabrication process. Point defects have their own classification depending on their electrical properties.

Some of them may have discrete energy levels in the Si band gap and therefore are electrically active, while others may not. The defect states can be acceptor- or donor-like. Acceptors are negatively charged if occupied by an electron and neutral otherwise, whereas donors are neutral if occupied by an electron and positively charged if not occupied. Defects also can have more than one energy level in the band gap, and there are even some which have both an acceptor and a donor state, being called amphoteric. Whether the states are occupied or not is determined in thermal equilibrium by the relative position of the energy level compared to the Fermi level.

Two sorts of defects are distinguished: shallow and deep. Lacking an exact definition, defects are commonly called shallow if they are close to one of the band edges so that they are ionised at room temperature, e.g., the dopants P and B. Deep defects are closer to the middle of the band gap.
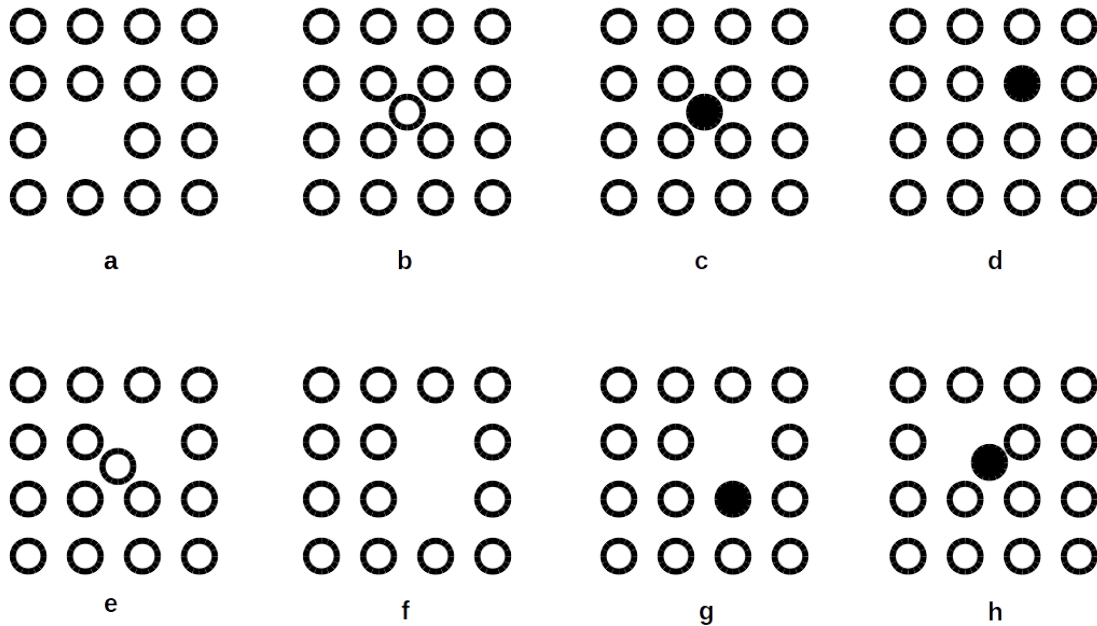
Figure 2.6: An overview on possible defect configurations. Example of simple defects: a) vacancy V, b) interstitial silicon atom I, c) interstitial impurity atom, d) substitutional impurity atom (e.g., phosphorus as donor). Examples of complex defects: e) close pair I-V, f) divacancy V-V, g) substitutional impurity atom and vacancy (e.g., VP complex), h) interstitial impurity atom and vacancy (e.g., VO complex). Impurity atoms denoted as a filled circles.

2.4.2 Cluster defects

Clusters are regions with high density of defects which emerge after irradiation by ultra-relativistic electrons ($E > 8\,\mathrm{MeV}$), intermediate and fast neutrons ($E > 35\,\mathrm{keV}$) and hadrons. They are mainly vacancies and interstitials which occupy about $15 - 20\,\mathrm{nm}^3$ of space with $10^5 - 10^6$ atoms [89]. They are able to change the local band structure in the cluster region. The exact nature of the defects inside a cluster is still not very well known. According to the model proposed by Gossick [89] a large number of Frenkel pairs is produced in the cluster region by a PKA (Primarily Knock on Atom). Due to their higher mobility, the Si interstitials diffuse fast out of this region, leaving a conglomeration of vacancies that form higher-order complex defects. Those are stable at room temperature and constitute the core of the cluster.

Cluster defects make an impact on the leakage current after fast hadron irradiation [90]-[91], because of the interaction between divacancies, located closely inside the cluster.

2.5   Damage effects – macroscopic processes

During the operation of silicon sensors in high energy physics experiments, their properties deteriorate due to radiation effects. The main requirements for silicon trackers are high signal-to-noise ratio and low leakage current or low heat dissipation during the operation. The microscopic processes inside the silicon crystal caused by defects in the lattice induce change of the macroscopic detector parameters. The deterioration of the electrical characteristic inflicted by the radiation makes it more difficult to fulfil of the basic requirements. Three main changes of sensor performance are discussed below.

2.5.1   Reverse current

One of the important effect of radiation induced damage is the increase of the reverse current. It has been shown that in case of irradiation with fast hadrons the current increase is proportional to the fluence and independent of the silicon material [80]. In Figure 2.7 the leakage current normalised per unit volume is shown as a function of the fluence. The increase of the current in volume unit can be expressed as:

$$\Delta I(T) = I(\Phi) - I_{Vol}(\Phi = 0) = \alpha \Phi V \tag{2.8}$$

where α is called reverse current damage factor, V is the volume of the sensor. The current I is linearly proportional to the depleted volume, it normally saturates for voltages above the full depletion voltage.
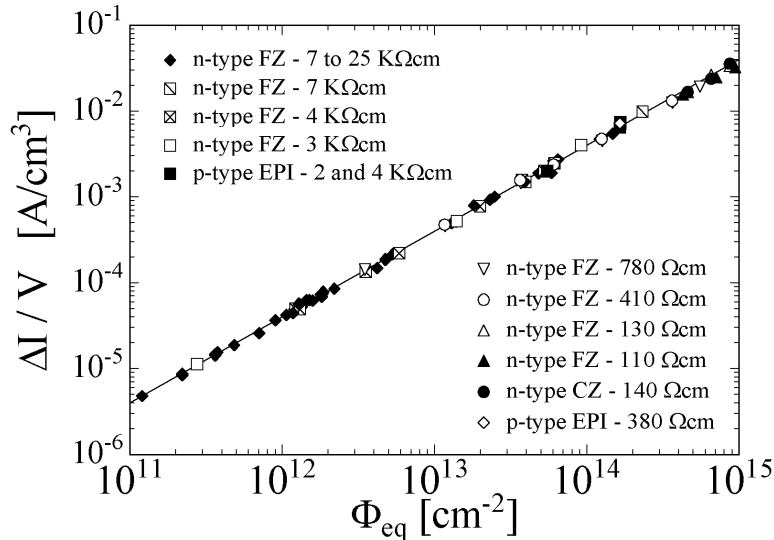
Figure 2.7: Leakage current per volume as function of the fluence. The sensors included in this study were produced by various process technologies from different silicon materials [80].

The leakage current is also strongly influenced by the temperature. The temperature dependence of the leakage current follows the relation:

$$I \sim T^2 \, e^{-\dfrac{E_g}{2k_BT}} \tag{2.9}$$

where $E_g = 1.12 \, \text{eV}$ is the silicon band-gap width at room temperature and $k_B = 8.62 \, \text{eV/K}$ is a Boltzmann constant. For consistency, the measurements of the current are usually normalised to 20°C.

The detector leakage current contributes to the shot noise and to the overall power dissipation of the system. During the operation of the CBM experiment the contribution of heat dissipation from silicon sensors is expected to be at the level of $6 \, \text{mW/cm}^2$. In order to mitigate high leakage currents irradiated sensors have to be operated at low temperature.

2.5.2 Doping type

One of the main parameters of a silicon sensor is the effective doping concentration which defines the depletion voltage (from 2.3):

$$V_{fd} = \frac{qd^2|N_{eff}|}{2\varepsilon\varepsilon_0}, \tag{2.10}$$

where d is the sensor thickness, q is a elementary charge, $|N_{eff}| = |N_d - N_a|$ with N_d and N_a as the positively charged donor and negatively charged acceptor concentration respectively. Radiation induced donor- and acceptor-like defects influence the effective doping of the detector. The donor removal mechanism will influence the effective space charge. After the formation of the phosphorus vacancy center, the phosphorous atoms cannot act as donors anymore. A typical example of the change in the depletion voltage respectively the absolute effective doping after irradiation is given in Fig. 2.8.

Here, the starting material is n-type silicon, doped with phosphorus donors. During the irradiation the sensor bulk material becomes effectively less n-doped. The effective doping concentration decreases until the number of acceptor states equals the number of donor states. The bulk material becomes intrinsic. After a certain fluence, the doping concentration increases again, however, the bulk material is already p-doped. This process is called *space charge inversion*. After the exhaustion of the initial doping concentration a linear increase of negative space charge is observed.

The macroscopic damage parameterisation is based on experimental results of the
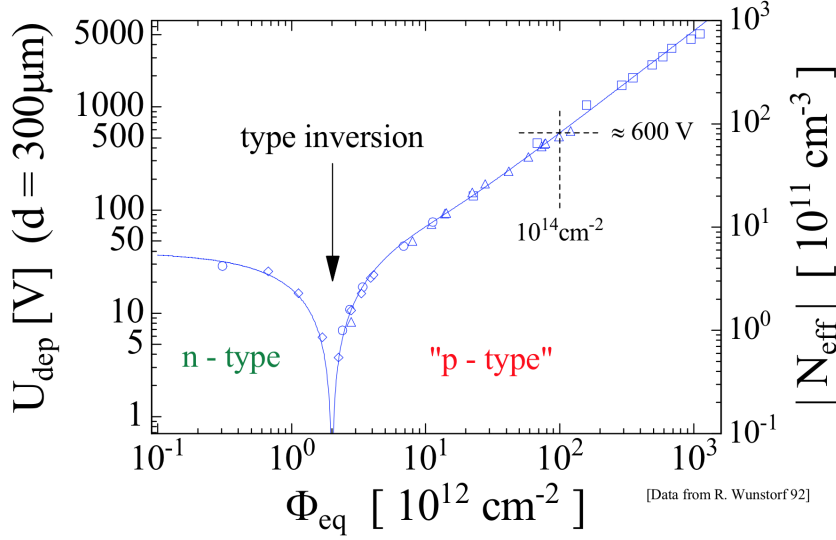
Figure 2.8: Change of the effective doping concentration in standard silicon, as measured immediately after neutron irradiation [80].

change in N_{eff} was described by the Hamburg model [80]. The absolute change in effective impurity concentration is a difference between the initial effective impurity concentration before irradiation and the one after irradiation $\Delta N_{eff}(\Phi_{eq}, t) = N_{eff,0} - N_{eff}(\Phi_{eq}, t)$, the evolution of the effective doping concentration as function of time and fluence can be described as:

$$\Delta N_{eff}(\Phi_{eq}, t(T_a)) = N_A(\Phi_{eq}, t(T_a)) + N_C(\Phi_{eq}, t(T_a)) + N_Y(\Phi_{eq}, t(T_a)) \qquad (2.11)$$

Here, N_A represents the short-term annealing, N_C is the stable damage term and N_Y is the long-term or anti-annealing component. The change in the doping concentration over the time is itself dependent on the annealing temperature T_a.

An example for the STS sensors is shown is Fig. 2.9 where type inversion from n- to p-like silicon occurs at the fluence about $2.25{\times}10^{13}$cm^{-2}. Using the Hamburg model equations and the values of the full depletion voltage before irradiation $V_{fd,0}$ as well as the thicknesses of the sensors, a parametrization of the V_{fd} was performed. In particular, the averaged value of the initial effective doping concentration $|N_{eff,0}| = 1.34{\times}10^{12}$ cm^{-3}, corresponding to the initial $V_{fd,0} = 85$ V was used in the calculation as well as the average sensor thickness of $290\,\mu$m. For calculation of the annealing components, 6 hours of annealing at 20°C that the sensors experienced during the bonding and assembly procedures, was considered.
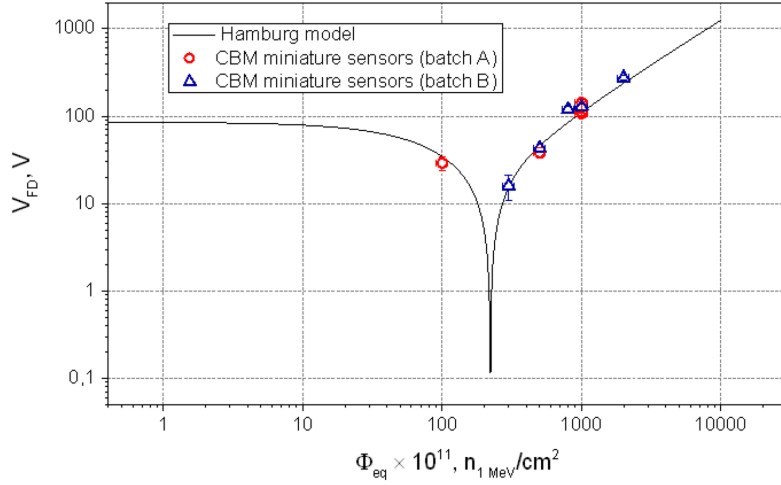
Figure 2.9: Full depletion voltage as a function of accumulated fluence. Experimental data for the STS sensors is shown together with the Hamburg model calculation, performed considering the initial space charge density of the STS sensors [92].

2.5.3   Charge collection efficiency and trapping

Electrons and holes created by an incident charged particle drift towards the corresponding electrodes; their movement in the electric field induces a current which flows into the charge sensitive preamplifier. In the ideal case, its integral is equal to the induced volume charge. Deep defects in the Si crystal could capture charge carriers during their drift through the bulk. If the typical trapping time of the charge carriers exceeds the shaping time of the readout electronics, the charge collection efficiency decreases. Also, the charge carrier cloud diffuses along its path. The charge collection time at the electrodes decreases with increasing bias voltage, and is also a function of the position in which the charges are created [93].

A hadron flux creates defects which introduce deep levels in the silicon band gap; they act as traps for the induced charge from particles passing through. The trapped charge can be successively released because of thermal excitation. Finally, it leads to enlargement of the charge collection time.

The increase of the inverse trapping time after irradiation is shown in Fig. 2.10 as a function of the fluence. The trapping effect results in an exponential absorption of the initially created e-h pairs:

$$N_{e,h}(t) = N_0 \ e^{\dfrac{-t}{\tau_{tr,e,h}}} \tag{2.12}$$

where $\tau_{tr,e,h}$ is the lifetime of electrons or holes. As long as the collection time

is much shorter then the charge carrier lifetime, and the integration time of the readout electronics is larger than the collection time, the number of collected pairs is about the same as initially created e-h pairs N_0.
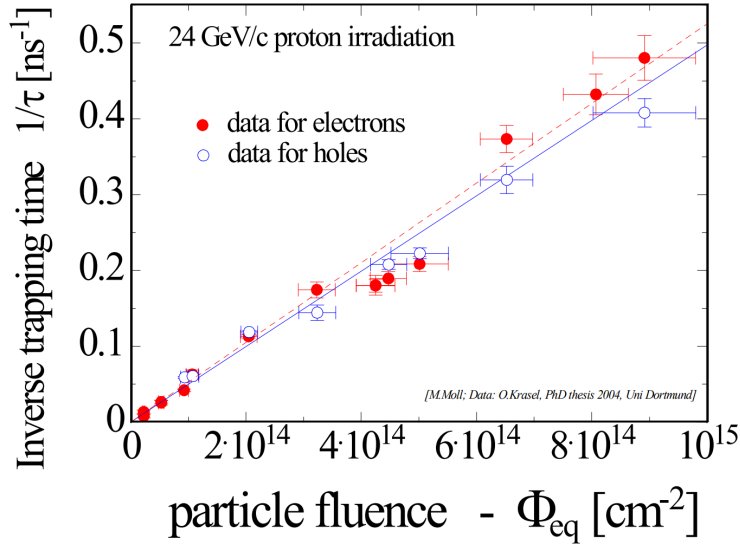
Figure 2.10: Inverse trapping time for electrons and holes in irradiated sensor with $24\,\mathrm{GeV}$ protons [94].

In case of comparable absorption and collection times, the reduction of the collected charge due to the trapping starts to be significant. Further radiation damage increases the number of the trapping centres, reducing the trapping lifetime. The following charge collection inefficiency, together with the increase of the noise, results in a worse signal-to-noise ratio for irradiated detectors [95].

As it was already discussed, the rise of leakage current enhances the shot noise in the detector. However, thanks to the strong temperature dependence, the leakage current can be suppressed by operation at low temperatures.

The most critical situation for silicon detectors in particle physics experiments is a change of effective doping concentration, which leads to an increase of the full depletion voltage. At hadron fluences above $10^{14}\,1\,\mathrm{MeV}\,\mathrm{n_{eq}cm^{-2}}$, the applied bias could exceed the system limits and sensors can stay undepleted, which leads to inability of fully registering charged particles traversing the bulk. According to the Hamburg model prediction, full depletion voltages up to $600\,\mathrm{V}$ are expected at CBM fluence, which coincides with the system requirements.

3

Radiation hardness studies of the silicon microstrip sensors for the STS

The main building blocks of the Silicon Tracking System (STS) are particularly sensitive to severe radiation environment of the Compressed Baryonic Matter (CBM) experiment. The expected lifetime fluence for the innermost part of the STS reaches $10^{14}\,1\,\mathrm{MeV\,n_{eq}cm^{-2}}$ after several years of operation. In the previous chapter, it was discussed that radiation at these levels will impact on the detector exploitation: increase of the leakage current and the full depletion voltage, decrease of the charge collection efficiency. While the reverse current and full depletion voltage influence the power dissipation and the noise of the detector, together with the decrease of the charge collection efficiency, they directly influence the final measurements of the tracking system.

To guarantee the required performance of STS over the full lifetime of the CBM experiment, double-sided silicon microstrip sensors have been studied focusing on bulk effects after the influence of radiation. Investigation of the sensor response after irradiation to a broad range of fluences is presented in this chapter. To study the impact of irradiation on the properties of the sensors, they were exposed to a $23\,\mathrm{MeV}$ proton flux at the irradiation facility.

3.1 Selection and electrical tests of sensors for irradiation

About 1100 specimen (including 15% extra material to compensate limited integration yield) will be produced in four variants for the final STS setup: 71 sensors of $62 \times 22 \, mm^2$, 326 of $62 \times 42 \, mm^2$, 326 of $62 \times 62 \, mm^2$, and 381 of $62 \times 124 \, mm^2$. The wafer size of 4 inch or 6 inch corresponds to the standard silicon sizes that the device can be processed on. The sensors used in these studies are developed, manufactured and tested in cooperation with two producers: Hamamatsu Photonics (HPK) and by CiS Forschungsinstitut für Mikrosensorik GmbH (CiS).

The HPK sensors are made of $320 \pm 15 \, \mu m$ thick silicon wafers, while the CiS provides thinner sensors of $285 \pm 15 \, \mu m$. The standard thickness of a silicon wafer is about $\sim 300 \, \mu m$, but could be changed if required. All tested prototypes are double-sided double-metal p^+-n-n^+ silicon microstrip sensors.

3.1.1 Irradiation facility

In order to evaluate the performance of the silicon microstrip sensors with respect to hadron fluence, an extensive irradiation campaign has been performed at the Irradiation Center Karlsruhe [96]. Sensor prototypes were exposed to a proton beam of $E_k = 23 \, MeV$; the narrow beam ($d = 4 - 8 \, mm$, see Fig. 3.1) sequentially scanned the sensor surface providing an uniform dose deposition. The sample box was constantly cooled with nitrogen flow to a temperature below -20°C to remove the heat produced by the interaction with the sensor, and to minimise annealing effects during irradiation.
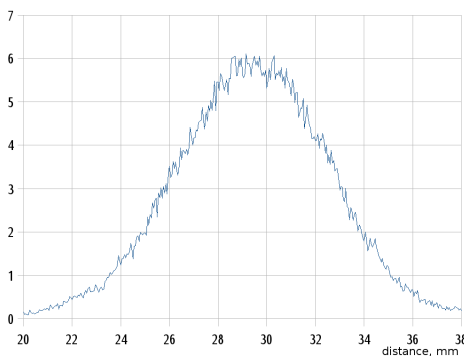
Figure 3.1: Example of a typical horizontal profile of the proton beam [96].
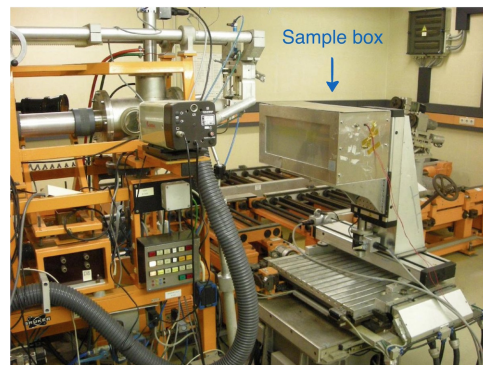
Figure 3.2: Sample box on the XY stage together with the beam line [96].

A thermally and electrically insulated box was placed 50 cm downstream to beam

exit window. It contained a protection plate made of pure aluminium with three[1]
silicon sensors mounted on top (see Fig. 3.2 and Fig. 3.3). The box was mounted on
a controlled XY stage in order to scan over sensor surface. The frame can be slid in
a thermally insulated box with a graphite absorber at the back. The front window
is made of a GFK frame covered by two thin Kapton® foils.
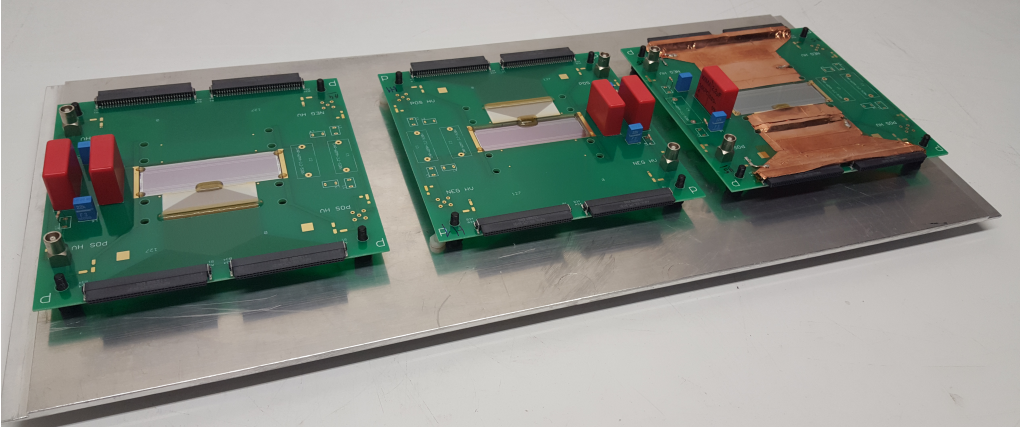
Figure 3.3: Samples ready for irradiation: three $62 \times 22 \, \text{mm}^2$ micro-strip silicon sensors glued inside
printed circuit board (PCB) and mounted on the aluminium shielding plate, designed at GSI to fit the
sample box.

The value of the proton fluence was estimated with the following relation:

$$\Phi_p = n_{\text{scan}} \frac{I_p}{e v_x \Delta y},\tag{3.1}$$

where I_p is beam current, n_{scan} number of sequential scans, e is a charge of electron,
v_x is a horizontal velocity of the stage, and Δy in the vertical step size. Using the
nominal values of $I_p = 1.5 \, \mu\text{A}$, $\Delta y = 1 \, \text{mm}$, and $v_x = 115 \, \text{mm/s}$ the obtained fluence
is 1.5×10^{13} protons/cm^{-2} per scan; with the hardness factor of 2.0 [97], which takes
into account the energy loss in Si, the fluence is $3 \times 10^{13} \, 1 \, \text{MeV} \, \text{n}_{\text{eq}}\text{cm}^{-2}$. The fluence
uncertainty is estimated to be not smaller than 20% [97]. If sensors are stacked in
two layers, the downstream set receives about 5% more of the deposited energy (see
Fig. 3.4).

In this study, sensors were irradiated without a bias voltage applied to obtain
mainly bulk damage and to avoid significant contribution of ionising damage. The
impact of protons was normalised to the equivalent non-ionising energy losses of
$1 \, \text{MeV}$ neutrons[2]. However, even non-ionising particles can deposit some ionising

---

[1]or six in case of two layers of sensors placed one under another
[2]values provided by KIT

dose via recoils. This contribution is estimated to be very small: $1\,\mathrm{MeV}\,\mathrm{n_{eq}cm^{-2}}$ in silicon corresponds to $2\times10^{-13}\,\mathrm{rad}$ [98]. During the irradiation campaign some sensors were exposed to the twice the CBM lifetime fluence, $2\times10^{14}\,1\,\mathrm{MeV}\,\mathrm{n_{eq}cm^{-2}}$, which is equivalent to $40\,\mathrm{rad}$ in terms of the ionising dose.
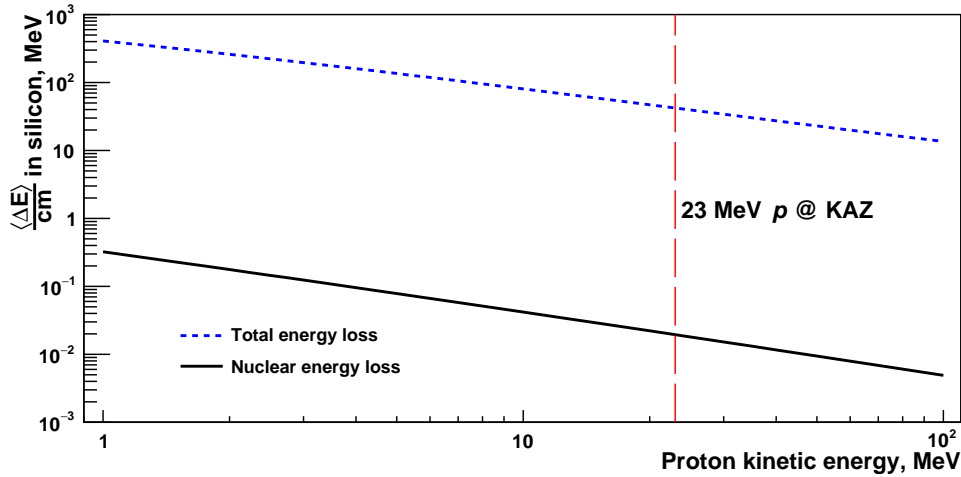
Figure 3.4: Average total energy loss and average energy loss in nuclear interactions for protons in silicon depending on the kinetic energy from the *pstar* data base [99]. The energy of KAZ (Karlsruher Kompakt Zyklotron) protons marked with the dashed vertical line.

3.1.2 Bulk electrical tests

Several kinds of electrical tests were carried out to evaluate the overall sensor conditions before the irradiation. Firstly, general electrical tests are done by the sensor manufacturers directly on a wafer before dicing into separate pieces: HPK performs the current-voltage (IV) scan up to $200\,\mathrm{V}$, while CiS tests sensors up to several hundreds volts. Also both companies do capacitance-voltage (CV) scans to estimate the total bulk capacitance depending on the bias voltage. This procedure provides the information about the full depletion voltage V_{FD} of the given sensor. The typical values of V_{FD} are $50-60\,\mathrm{V}$ for HPK sensors and up to $70-80\,\mathrm{V}$ for CiS sensors. The sensor manufacturers also perform strip-by-strip electrical tests to identify strips with abnormal characteristics. Particularly, a high leakage current in a strip can indicate insufficient or broken insulation layers on the AC pad. Such a so called "pin-hole" is a short between strip implant and metal line due to a hole in the coupling dielectric. Leakage current can freely flow into the amplifier in presence of the pinhole. The number of malfunctioning strips is an important characteristic, and will be used as an acceptance criterion during the mass production phase: one

can tolerate not more than 1% of dead strips per sensor side [57].

In addition to the tests done by the vendors, detailed electrical studies were performed in order to select sensors with the desired performance for the particular tasks. Electrical breakdown, i.e. a sudden rise of current at small steps of voltage, is not expected in the bias voltage range up to $500\,\text{V}$ for the sensors chosen to be irradiated to high doses. Also the IV curves of such sensors should be smooth and without particular irregularities. Unlike sensor producers, electrical tests were performed after the silicon wafers have been diced into sensors.

The bias voltage for IV and CV tests is provided to a sensor with a pogo-pin structure shown in Fig. 3.5. It can handle sensors of different sizes up to $62\times62\,\text{mm}^2$. This test socket is designed to provide bias voltage to a silicon sensor without bonding, here bias contact is supplied by so-called Spring Probe Pins ("pogo-pins") of a $30\,\mu\text{m}$ diameter located in the area corresponded to the center of a bias pads. The socket consists of two parts: bottom and top, which are connected together and held in place by metal screws. The sensor under test is placed in the bottom part of the socket which is milled out with a high precision to ensure proper positioning. Thus, easier exchange of numerous sensors is possible for the electrical tests, which is very helpful during mass measurements.
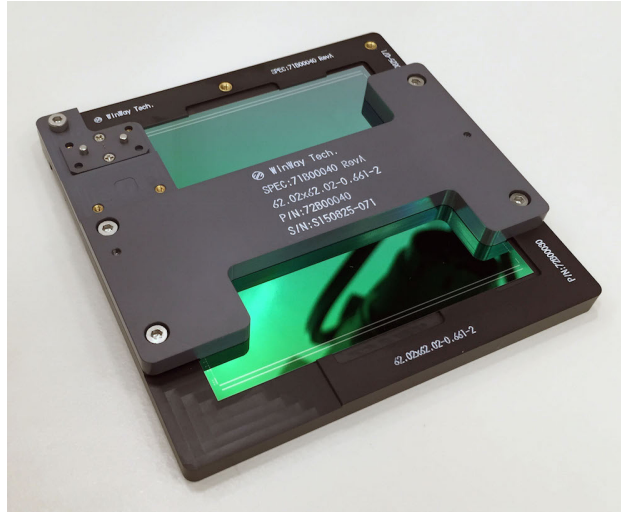
Figure 3.5: Photo of the $62\times22\,\text{mm}^2$ STS sensor installed inside the pogo-pin structure. The test socket designed at GSI detector laboratory.

In Fig. 3.6, one can see the results of bulk electrical tests of the HPK and CiS sensors from different batches of the three smaller sizes up to $62\times62\,\text{mm}^2$.

The candidates for irradiation were tested in the clean room at stable temperature and humidity conditions. In order to compare data from different sensors measured in different environment, the leakage current per unit area was scaled to $20°\text{C}$,
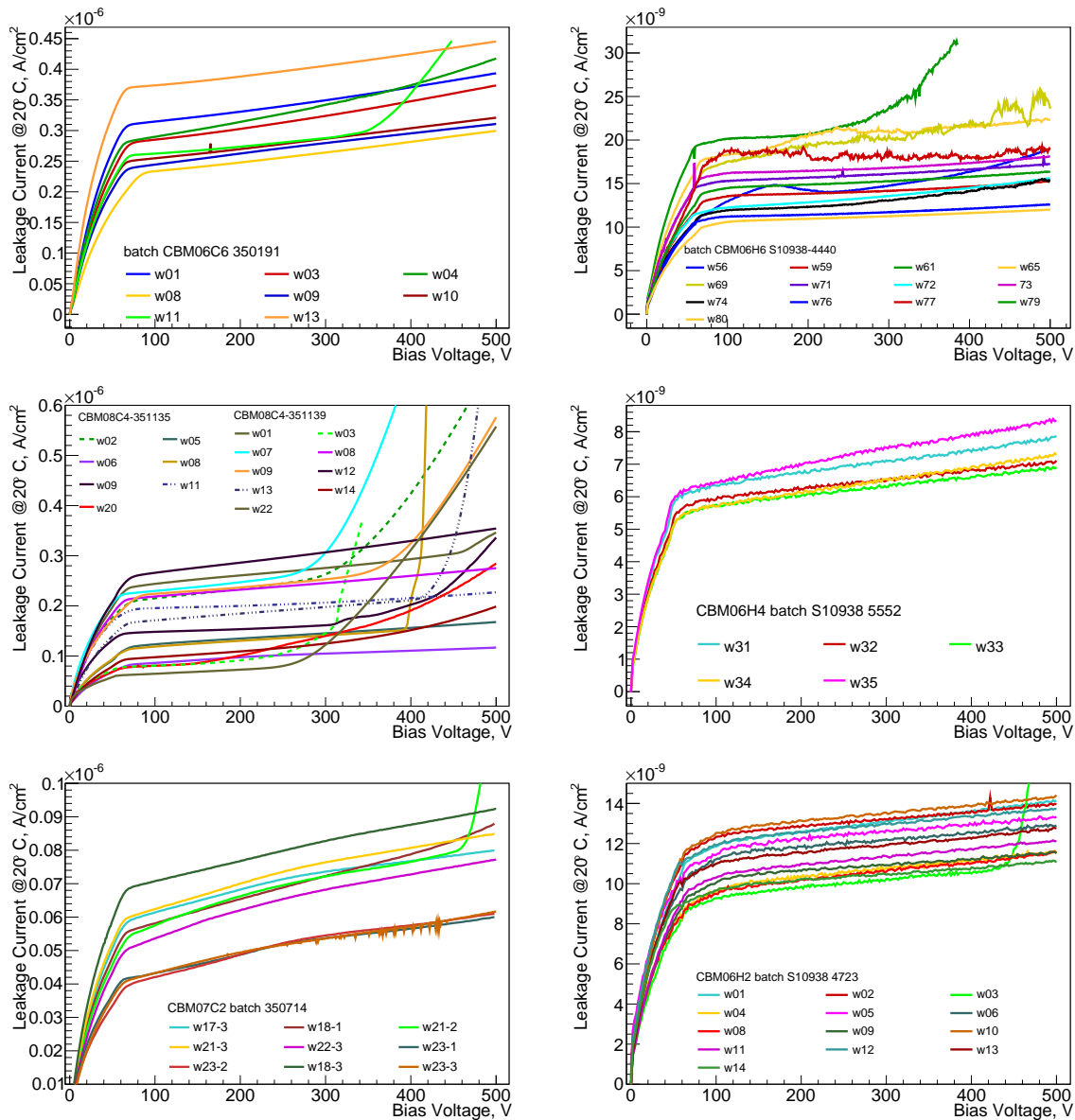
Figure 3.6: Leakage current depending on the applied bias voltage for CiS (left column) and HPK (right column) sensors before irradiation. Tests are performed at the GSI silicon laboratory using a pogo-pin fixture. Sensors in three different form-factors were included in the study (top to bottom): $62 \times 62 \, \mathrm{mm^2}$, $62 \times 42 \, \mathrm{mm^2}$, and $62 \times 22 \, \mathrm{mm^2}$.

and the CV data was normalised to the sensor area. The leakage current strongly depends on the temperature with the known relation:

$$I \propto T^2 \, e^{-\dfrac{E_g}{2k_B T}}, \tag{3.2}$$

where $E_g = 1.12 \, \text{eV}$ is the silicon band-gap width [100] at room temperature and $k_B = 8.62 \, \text{eV/K}$ is the Boltzmann constant. This normalisation is performed with the following ratio:

$$I(T_0) = I(T_1) \times \left(\frac{T_0}{T_1}\right)^2 e^{-\dfrac{E_g}{2k_B}\left(\dfrac{1}{T_0}-\dfrac{1}{T_1}\right)}, \tag{3.3}$$

where $T_0 = 293 \, \text{K}$.

Table 3.1 provides the specifications of the sensors selected for irradiation, denoting the vendor, number of generation and batch, ordinal wafer number, thickness, and fluence.

Two out of ten $62 \times 62 \, \text{mm}^2$ sensors selected for irradiation were chosen to serve as reference specimens with zero fluence. Four others were exposed to $10^{14} \, 1 \, \text{MeV} \, \text{n}_{\text{eq}}\text{cm}^{-2}$ and yet another four received $2 \times 10^{14} \, 1 \, \text{MeV} \, \text{n}_{\text{eq}}\text{cm}^{-2}$.

Numerous $62 \times 42 \, \text{mm}^2$ CiS sensors demonstrate early breakdown, when leakage current increases rapidly in a short amount of time, starting from about 270 V; such sensors were rejected. Out of numerous tested prototypes, three HPK and three CiS sensors were selected to be irradiated to three different fluences: to the half-lifetime, lifetime and double-lifetime fluence. Here, `CBM08C4-w05` and `CBM06H4-w84` were selected as references. Signals from a ^{90}Sr β-source measured with the irradiated sensors were then normalised to the signal from non-irradiated ones for the particular vendor of particular size.

The $62 \times 22 \, \text{mm}^2$ sensor prototypes from the different batches of both vendors showed good performance (see Fig. 3.6) in terms of the leakage current. Twelve sensors were selected for the irradiation. Unlike for the other groups, the $62 \times 22 \, \text{mm}^2$ sensors were tested with a ^{90}Sr source before and after proton irradiation. No reference sensors were chosen out of this group since each sensor has a reference measurements before the irradiation.

The typical value of leakage current for the HPK sensors is about factor of 10-50 smaller then for the CiS sensors. Although all measurements of the current were normalised to the temperature and area of the sensor, the leakage current fluctuates from one batch to another: for CIS sensors it varies in the range of

Size	Vendor and gen.	Batch #	Wafer #	Fluence, 10^{14} 1 MeV $n_{eq}cm^{-2}$	Current at 150 V, nA/cm^2
62×62 mm^2	CiS 06	350191	*09*	*0.0*	253.2
			03	1.0	281.4
			08	1.0	230.8
			01	2.0	309.4
			10	2.0	251.2
	HPK 06	S10938-4440	*72*	*0.0*	12.0
			65	1.0	18.2
			71	1.0	14.9
			59	2.0	13.2
			79	2.0	14.1
62×42 mm^2	CiS 08	351135	*05*	*0.0*	124.0
		351135	11	0.5	190.0
		351135	06	1.0	88.2
		351139	08	2.0	120.9
	HPK 06	S10938-5552	*84*	*0.0*	6.1
			33	0.5	5.7
			32	1.0	5.8
			31	2.0	6.3
62×22 mm^2	CiS 07	350714	22-3	0.5	70.9
			23-1	0.5	55.7
			21-3	1.0	80.4
			23-2	1.0	55.0
			17-3	2.0	78.8
			23-3	2.0	56.6
	HPK 06	S10938-4723	06	0.5	11.2
			04	0.5	9.7
			08	1.0	9.5
			01	1.0	11.8
			02	2.0	12.2
			05	2.0	11.5

Table 3.1: Selected sensors and their characteristics. The reference (zero-dose) sensors of $62\times62\,\text{mm}^2$ and $62\times42\,\text{mm}^2$ groups marked with italic. Each of the $62\times22\,\text{mm}^2$ sensors served as a reference to itself.

$0.05 - 0.35\,\mu\mathrm{A/cm}^2$, for HPK $6 - 18\,\mathrm{nA/cm}^2$. The summary of the detailed sensor characteristics (such as the full depletion voltage, noise, most probable value of signal) can be found in the Appendix A.

3.1.3 Electrical tests after irradiation

In order to evaluate the performance after the irradiation, the sensors were tested again for their IV and CV characteristics. Typical dependencies of leakage current vs. applied voltage (IV) and bulk capacitance vs. applied voltage (CV) of irradiated sensors are shown in Figs. 3.7-3.10. These tests are performed in the GSI STS laboratory using custom printed circuit boards for sensor handling. As one can see from Fig. 3.7 (right) and Fig. 3.10 (right) the bulk capacitance does not depend on the received fluence, while the leakage current (see Figs. 3.8-3.9) increases by few orders of magnitude (see last two columns of Table 3.1 for the quantitative comparison). Measurements of irradiated sensors were done at temperatures of about $-10°\mathrm{C}$, the accuracy of the temperature measurement is $\pm 2°\mathrm{C}$, and leads to an uncertainty of the normalisation of $\pm 2\%$.

The increase of the leakage current per unit volume is linear with respect to the fluence is:

$$\frac{\Delta I}{V} = \alpha \Phi_{\mathrm{eq}}, \tag{3.4}$$

where $\alpha \approx 4 - 6 \times 10^{-17}\,\mathrm{A/cm}$ is a damage coefficient which is independent of the material type, the resistivity or the irradiating particles (neutrons, protons, pions), but depends on temperature, and the time between exposure to radiation and measurement (annealing).

After full depletion, the bulk capacitance saturates at the same level for the sensors before and after irradiation: $\sim 10\,\mathrm{pF/cm}^2$ for sensors from CiS, $\sim 25\,\mathrm{pF/cm}^2$ for HPK prototypes, as expected. Breakdown was not observed before $500\,\mathrm{V}$, irradiated sensors survive up to $800\,\mathrm{V}$ (some of them even up to $1000\,\mathrm{V}$), if no damage occurred. Characteristics of these sensors after irradiation are listed in Table A.1, Appendix A.

The radiation damage of the silicon sensor bulk leads to an increase of the leakage current; together with the high bias voltage (up to $500\,\mathrm{V}$), it causes significant power dissipation in the detector [101]. Since the volume leakage current increases nearly exponentially with the sensor temperature (approximately it doubles every $7°\mathrm{C}$ around room temperature), the thermal runaway may occur if the cooling is not provided during the operation of heavily irradiated sensors [102]. Also, the shot noise depends on the leakage current as $\propto \sqrt{I}$, and can become the dominating noise component for heavily irradiated sensors.

The reverse current and full depletion voltage influence the power dissipation
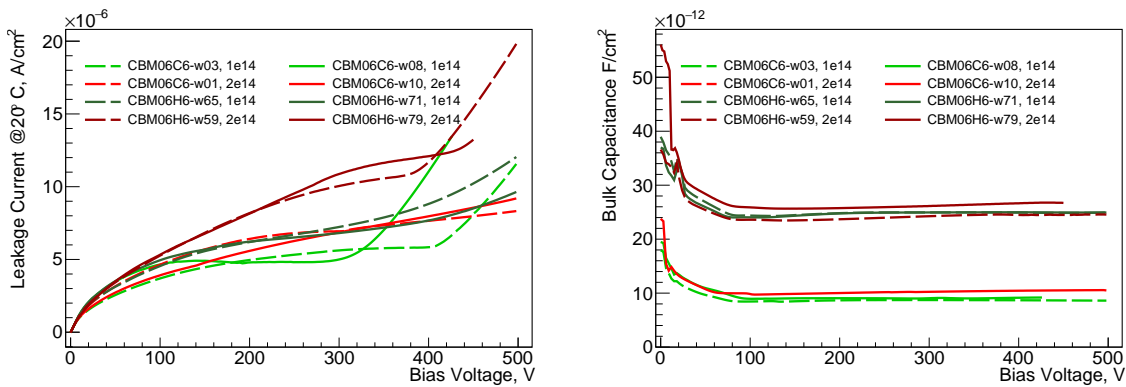
Figure 3.7: Leakage current (left) and bulk capacitance (right) depending on the applied bias voltage for irradiated $62 \times 62\,\mathrm{mm}^2$ sensors.
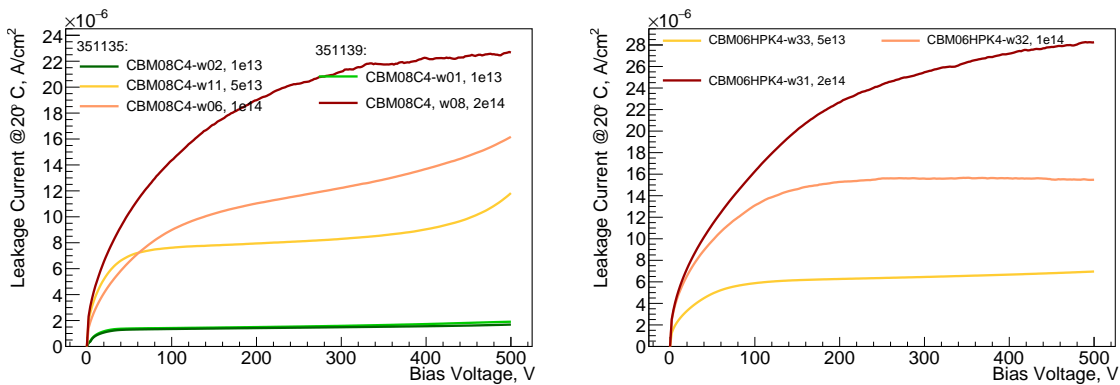
Figure 3.8: Leakage current performance of CiS (left) and HPK (right) $62 \times 42\,\mathrm{mm}^2$ sensors after irradiation, lighter color represents lower received fluence.
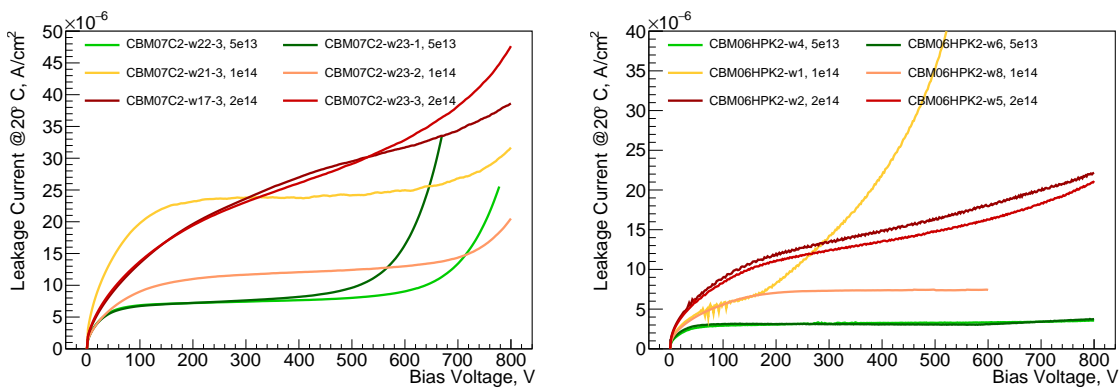
Figure 3.9: Performance of CiS and HPK sensors irradiated to different fluences in terms of leakage current vs. bias voltage up to $800\,\mathrm{V}$ for $62 \times 22\,\mathrm{mm}^2$ prototypes. Some sensors (e.g. CBM06H6-w59, 2e14 and CBM06H6-w79, 2e14 exhibit a "soft" breakdown, i.e. the current continues rising with increasing voltage but less fast than for a full breakdown on a small voltage difference. No breakdown was observed at high voltages. CBM06HPK2-w1, 1e14 was mechanically damaged during measurements.
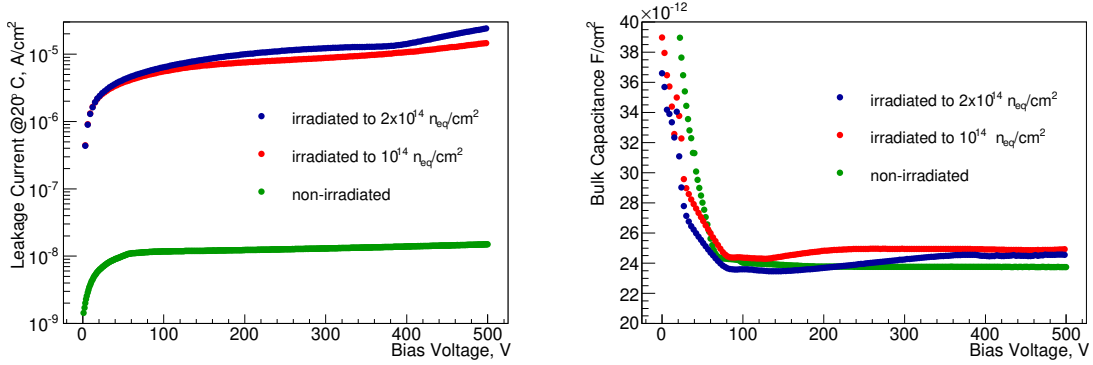
Figure 3.10: Comparison of the leakage current(left) and the bulk capacitance (right) as a function of the applied voltage for non-irradiated and irradiated $62 \times 62\,\mathrm{mm}^2$ sensors produced by HPK.

and the noise of the detector. The power consumption is scaling linearly with the leakage current as well as the bias voltage. From the plots above, one can see that different sensors from both vendors reach the same leakage current per area at $500\,\mathrm{V}$ @20°C with the same fluence: $2\,\mu\mathrm{A/cm}^2$ at fluence 10^{13}, $10\,\mu\mathrm{A/cm}^2$ at fluence 10^{14}, $30\,\mu\mathrm{A/cm}^2$ at fluence $2 \times 10^{14}\,1\,\mathrm{MeV\,n_{eq}cm}^{-2}$. Assuming the STS detector will operate at -10°C, the maximum power dissipation impact from the silicon sensor irradiated to $1 \times 10^{14}\,1\,\mathrm{MeV\,n_{eq}cm}^{-2}$ operated at $500\,\mathrm{V}$ is expected to be at the level of $10\,\mathrm{mW/cm}^2$.

3.1.4 Strip integrity test

Strip integrity tests allow to identify the presence of defective strips in a detector, which are shorts in dielectric layers, an interruption of the metal, or shorts to neighbour strips. Since the CBM-STS microstrip sensors have a capacitively coupled readout, a short defect causes leakage current flowing directly into the readout electronics and drive the channel into saturation, or even cause malfunction of the whole ASIC (Application-Specific Integrated Circuit). Therefore, it is very important to test each strip for such pin-holes. Strips with identified as pin-holes must not be bonded to the readout ASIC [103]. Figure 3.11 depicts examples of shorts in several strips, which show up as high value of current.

This measurement has been done by contacting the strip's DC and AC pads with two needles, and measuring the current after a test voltage of $20\,\mathrm{V}$ is applied. A very low current around $1 - 100\,\mathrm{pA}$ is observed if the insulation layer is intact and the isolation is perfect. A current above $10\,\mathrm{nA}$ indicates a pinhole, and such a strip has to be marked as a bad one.

There is a possibility that the isolation layer can be affected by ionising radiation.
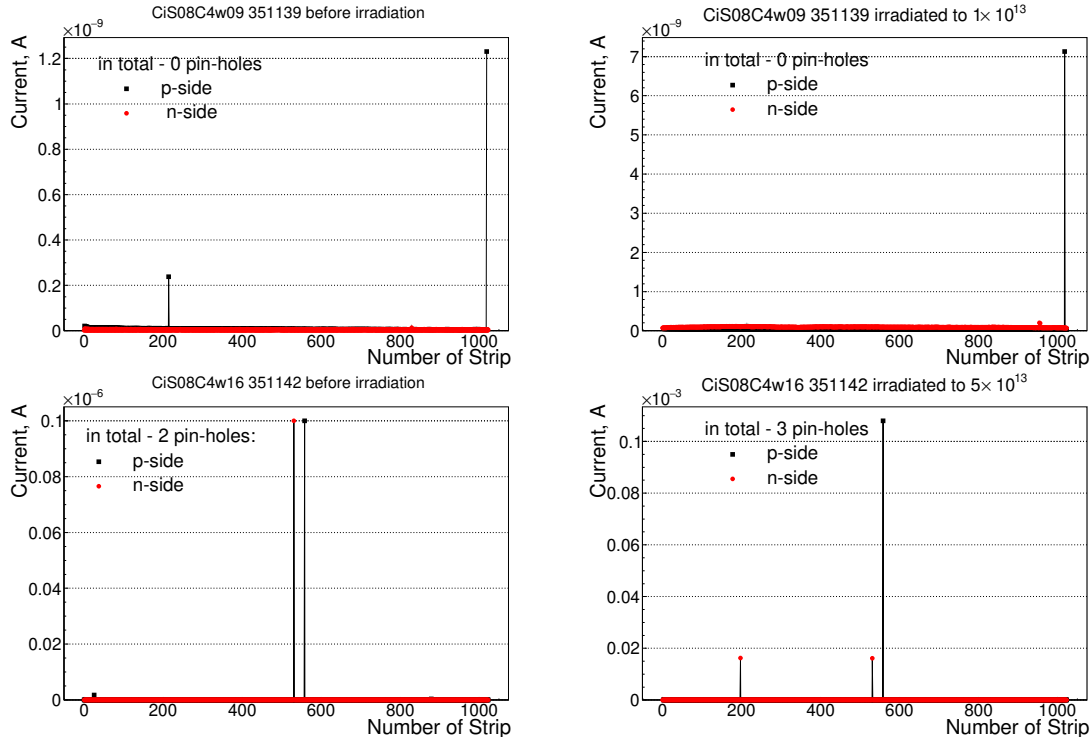
Figure 3.11: Strip integrity tests for sensors before (left) and after (right) irradiation to $10^{13} \, 1 \, \text{MeV} \, \text{n}_{\text{eq}} \text{cm}^{-2}$ (top) and to $5 \times 10^{13} \, 1 \, \text{MeV} \, \text{n}_{\text{eq}} \text{cm}^{-2}$ measured at $20 \, \text{V}$.

It was reported in Ref. [104], that radiation could lead to formation of pin-holes, where the number of defective strips increases with applied dose. Here, additional pin-holes have been created, but total amount remained within the specification of 2 %.

In order to cross-check whether it is still within the specification for the CBM-STS microstrip sensors, integrity test as a part of the QA procedure was realised. Sensors before irradiation were measured at the vendor site at $20 \, \text{V}$, after irradiation they were measured at the same conditions in the clean-room environment at the Tübingen University [105]. In Fig. 3.11, values of current measurements are depicted, the final number of measured pin-holes is presented in Table 3.2.

These results show that the sensor prototypes have a good safety margin even after radiation. The number of pin-holes before and after irradiation are remaining the same. In general, current through the capacitor increases after irradiation (see Fig. 3.12) in 100 times after applied fluence of $10^{13} \, 1 \, \text{MeV} \, \text{n}_{\text{eq}} \text{cm}^{-2}$. The n-side behaves differently compared to the p-side due to the presence of "long" strips interconnected via double metal layer.

Any leakage current flowing into the CSA (Charge Sensitive Amplifier) will affect

Table 3.2: Results on number of pin-holes for sensors before and after irradiation.

Name of sensor	Before		Fluence, $1\,\mathrm{MeV\,n_{eq}cm^{-2}}$	After	
	p-side	n-side		p-side	n-side
cbm08c4w09 351139	0	0	1×10^{13}	0	0
cbm08c4w14 351142	5	1	1×10^{13}	5	1
cbm08c4w14 351139	0	2	5×10^{13}	0	6
cbm08c4w16 351142	1	1	5×10^{13}	1	2
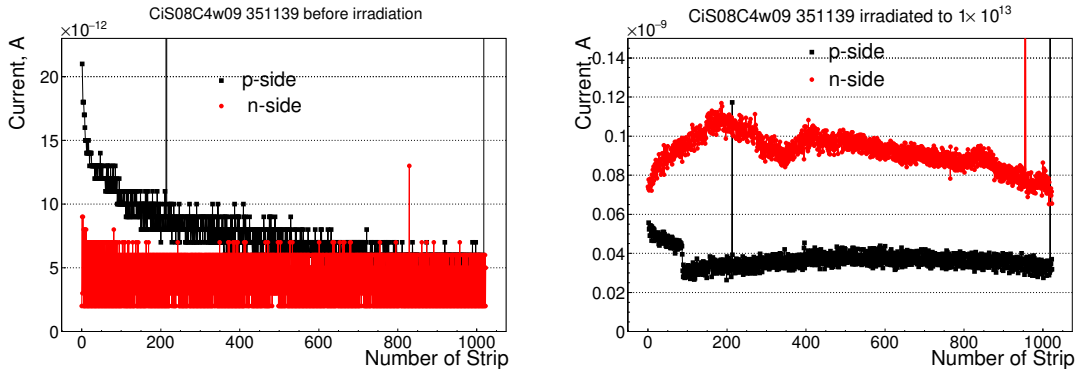
Figure 3.12: Strip integrity tests for sensors before (left) and after (right) irradiation to $10^{13}\,1\,\mathrm{MeV\,n_{eq}cm^{-2}}$, where Y axis is zoomed for illustration purposes. Red points represent the current on the n-side, black – on the p-side.

the ASIC performance, the shift of the DC level at the CSA output, and this will change the feedback resistance value. After irradiation, the leakage current which flows to CSA, increased from $5-10\,\mathrm{pA}$ to $0.12\,\mathrm{nA}$, but stays within the STS-XYTER specifications of 1 nA per strip, and will induce a negligible offset only [106].

3.1.5   Impact of glue

After preliminary electrical tests, the silicon microstrip sensors are installed in the test structures, and attached to the readout electronics. Despite the fact, that detector modules for the final STS setup will be connected via aluminium-polyamide micro-cables to the front-end electronics, PCBs equipped with aluminium-ceramics pitch adapters and four 64-pin ERNI connectors [3] were used to readout the sensors under test. Thus, one can test several dozens of sensors with the same pair of front-end boards. More details on the PCB design and the connection scheme can be found in Sec. 3.2.

A particular aspect of the mechanical integration that could affect the sensor performance is the usage of the epoxy glue. The purpose of the glue is to fix the sensor

---

[3]https://www.erni.com

nested on the PCB opening and to protect the fragile wire bonds from possible mechanical damage. However, the applied glue can unpredictably distort the electrical fields of the detector elements due to its large dielectric constant (typically $\varepsilon \gtrsim 5$ for epoxy compounds). Thus, one can expect an increase of the parasitic capacitance for the readout lines, which would lead to smaller signals and deterioration of the noise performance. Also, previous observations showed that if the glue is applied to the sensor edge, the leakage current increases [107].

In order to check possible problems, a set of tests was performed with two sensors of $62 \times 22\,\mathrm{mm^2}$ size measuring IV and CV curves at different stages of the integration. Two types of non-conductive UV-curing epoxy glue were chosen. Firstly, the glue was applied on the cutting edges of the sensor – to glue it into the PCB cut-out; secondly, the glue was used to protect wire-bonds (glob-top) from the routing lines on the PCB to the pitch-adapter and from the pitch-adapter to the strips of the sensor.

Sensors were tested for leakage current and bulk capacitance at the different stages of the mechanical integration:

1. sensor alone installed to the pogo-pin test socket;

2. sensor mounted into PCB and wire-bonded, small amount of glue applied on the balcony support structure;

3. same as above with glue on top of wire-bonds (so called "glop top") including power-bonds for the bias voltage.
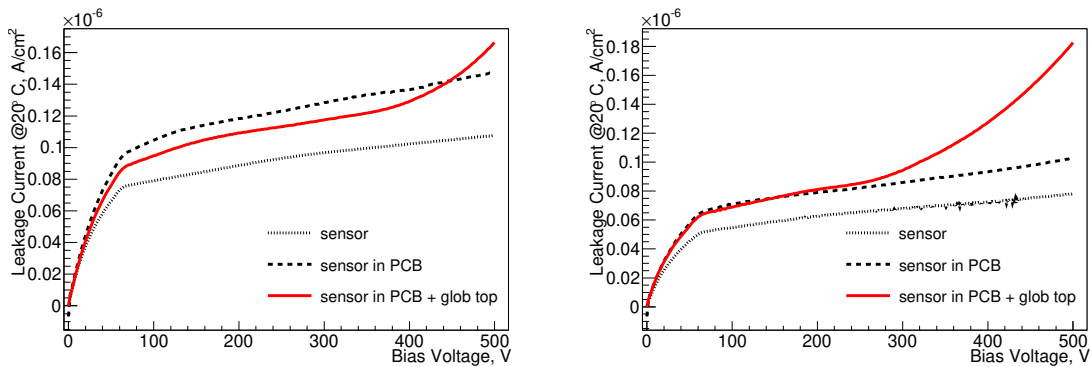
Figure 3.13: Comparison of the leakage current before and after applying the glue for two CiS 6×2 sensors: `cbm07c2_b350191_w21-3` and `cbm07c2_b350191_w23-3`.

The results of the tests are shown in Fig. 3.13 and Fig. 3.14 for the IV and CV measurements, respectively. Selected sensors demonstrated a good performance; no
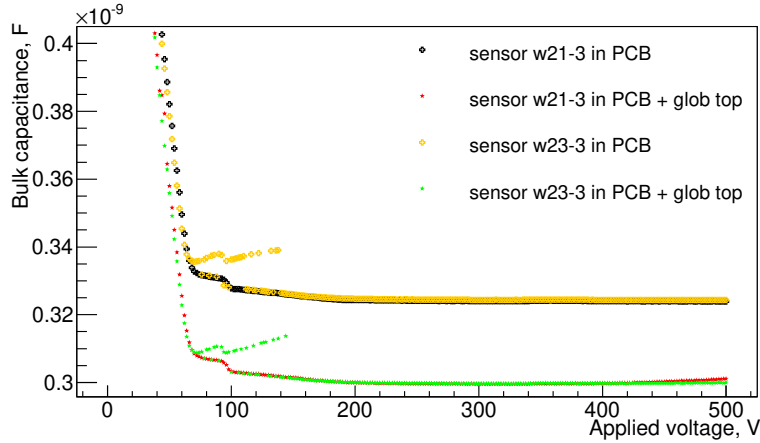
Figure 3.14: Comparison of the sensor's bulk capacitance before and after applying glue.

sign of breakdown was observed below $500\,\text{V}$ for the bare sensors. After they have been installed into PCB, their leakage current increased by about $0.3\,\mu\text{A}$, which anyway allows to apply bias voltage sufficient for over-depletion. The shape of the IV curve remained unchanged, as it is seen in Fig. 3.13. During the third set of tests an occurrence of soft breakdown was observed: the current starts to increase more rapidly in the middle of the range, however the sensor may still be operated up to $500\,\text{V}$. It is remarkable that the bulk capacitance also decreases by about 10% comparing to the measurement without wire-bond protection, although measuring conditions stayed same. This can be explained by effect of the measurement with LCR-meter.

3.2 Studies of the sensor response to minimum ionizing particles

The purpose of the silicon microstrip detectors is to register charge carriers induced by an interaction with a charged particle in the detector sensitive volume. According to the channel map, the signal in particular strips is interpreted as a position of the interaction which then provides information for the tracking and event reconstruction. The typical charged particles expected to cross the STS volume are π^+, K^+, p, e^-, and μ^- together with their antiparticles. An important specification of the CBM operation is that the reaction products are expected to have relatively high momenta (some $\sim 100\,\text{MeV}$ or $\sim 1\,\text{GeV}$); for most of the cases their Lorentz factor will be $\beta\gamma \sim 3$. These charged particles can be considered as Minimum Ionizing Particles (MIPs): the energy loss by electromagnetic interactions reaches its

minimum, followed by the very slow logarithmic increase towards higher momenta. The particular advantage of this assumption is that MIP particles loose energy in thin detector almost independently of the momentum or particle type (assuming the same electrical charge).

Track reconstruction algorithms require information of a charged particle's hit position provided by the detector module. Depending on their trajectory, charged particles may deposit energy in a sensor in a way that the charge is shared between few strips (so-called one-strip, two-strip, three-strip etc., clusters). The hit position is then determined by track reconstruction routines.

Thus, the main characteristic of the detector module (sensor + readout chain) is the quality of its response to MIPs. The SNR has to exceed 10, also for irradiated sensors. This chapter is devoted to the studies of this quantity. MIPS were simulated by ^{90}Sr β-particles with the energies exceeding 1 MeV, selected by the corresponding triggering of the sensor readout chain.

Relativistic electrons from a radioactive source can thus serve as a good reference for the future operation of the STS detectors. Particularly, the ^{90}Sr isotope is a clean and powerful source of high-momentum electrons. It undergoes a β decay into ^{90}Y, with a decay energy of 0.546 MeV. The half-life of ^{90}Sr is 28.79 years and its daughter product ^{90}Y also decays via β^- process with the half-life of 64.1 hours [108]. The energy released in β decays of these two isotopes is 0.55 MeV and 2.28 MeV respectively, see Fig. 3.15 for the energy spectra.
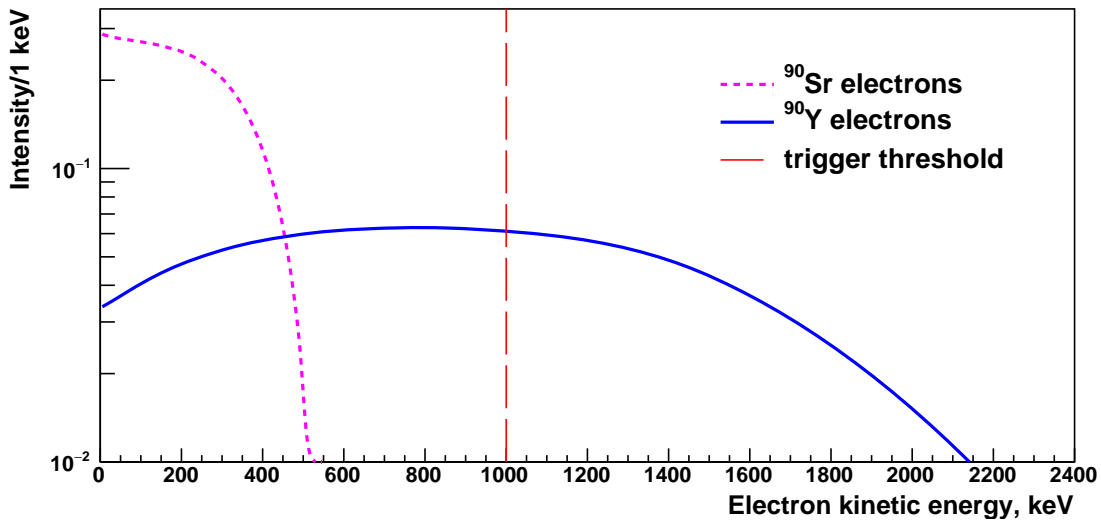
Figure 3.15: The energy distribution of β-electrons emitted by the ^{90}Sr-^{90}Y radioactive source. Data are taken from Ref. [109]. The vertical dashed line represents the threshold applied to reject the soft component of the spectrum.

A sealed ^{90}Sr isotope source with the intensity of 37 MBq was used in these studies. The source is enclosed in the centre of an acrylic cube for radiation shielding and preliminary collimation of the electron beam.

The Landau distribution fails to describe energy loss in thin absorbers such as silicon detectors [110]. Typically, the distribution of the energy loss in thin absorbers appears to be wider; also it has more irregularities than the Landau distribution [111]. Several attempts in the past showed that the Landau-Vavilov distribution, which is commonly used to characterise the response of the particle detectors, fails to describe the spectra [103]. Thus a simplified approach is used for the analysis of the measured energy, loss which involves integral characteristics of the spectrum, such as its mean and median values. To compare the performance of the silicon sensors before and after irradiation, the ratio of the most probable energy loss was used. In this way many systematic effects are expected to be cancelled.

3.2.1 Readout electronics

Because of the unavailability of the final STS readout system, alternative electronics for relative charge collection measurements were employed. For the testing purposes the Alibava readout electronics was used, which is provided by Alibava Systems© [112]. It is a dedicated laboratory test system for silicon strip detectors. It is based on the *Beetle* ASIC which was initially developed for silicon tracking system of the LHCb experiment [113]. The system consists of a front-end board with one *Beetle* chip (Daughter Board, DB) which can be attached to the sensor and the back-end FPGA-board (Mother Board, MB) which hosts a 10-bit ADC, and provides the signal digitisation, data storage and communication with a PC via the USB port [114]. The Mother Board needs an external analogue or digital signal for the validation of the particular event.

The *Beetle* chip integrates 128 channels, each consisting of a low-noise charge-sensitive preamplifier, an active CR-RC pulse shaper and a buffer. It is operated with internal clock frequency of 40 MHz: the input signal is being read out by the DB every 25 ns. The buffer has 160 entries which leads to a full period of $160 \times 25\,\text{ns} = 4\,\mu\text{s}$. If the MB receives a trigger signal during the given buffer cycle, the particular snapshot (defined by the latency register of the chip) is sent for digitisation and storage on the disk.

The Alibava Systems setup is provided with a dedicated data acquisition (DAQ) software. To collect data with a ^{90}Sr source, the Radioactive Source (RS) mode of the Alibava DAQ software was used. In this regime the MB uses an internal Time-to-Digital converter (TDC) to measure the time of the trigger signal within pulse the period of the *Beetle*. Thus one can deduce, which particular part of the signal
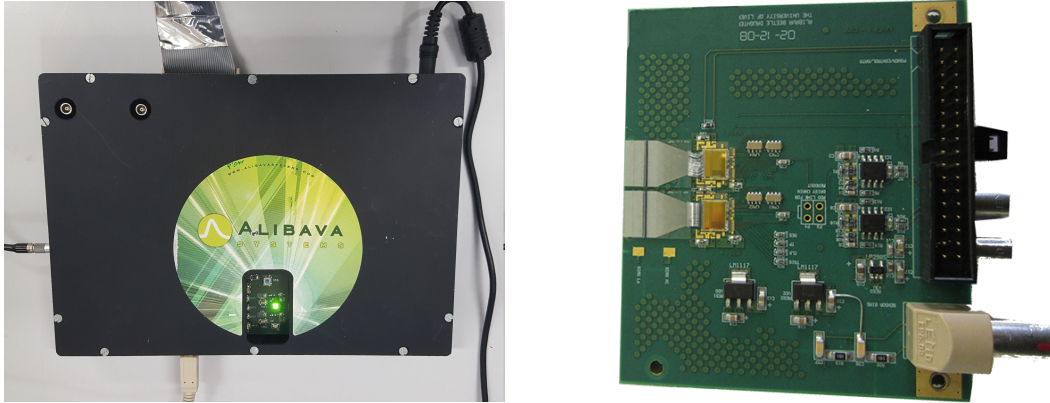
Figure 3.16: The Mother Board (left) and the Daughter Board (right) acquired from Alibava Systems©.

was digitised. It matters a lot if one operates Alibava with the default settings of the chip, the signal falls significantly within the time window of 25 ns. Thus one has to apply offline selection criteria later in order to cut out the very top of the signal pulse.

There are three particular *Beetle* parameters which affect the pulse shape and position most: latency, V_{fp}, V_{fs}. They can be set and cross-checked with the Alibava DAQ software. The V_{fp} value defines the time constant of the preamplifier and the V_{fs} plays the same role for the shaper. Both V_{fp} and V_{fs} can be set in arbitrary units in the range $0 - 255$. In general, higher V_{fs} values give a longer peaking time. The latency value sets the FIFO count to be sent to the ADC: the optimal value depends on the trigger delay and may differ from one setup to another. Particularly, longer cables for the trigger signal lead to higher values of latency. The measured pulse shape for our setup at the default *Beetle* settings ($V_{fp} = 0$, $V_{fs} = 0$, latency 128) is depicted in Fig 3.17, left. The pulse shapes for some alternative chip settings are shown in Fig 3.17, right.

These chip register values can be adjusted such to make the pulse shape long enough to be constant within the 25 ns time window. With the latency parameter the pulse can be shifted in 25 ns steps to compensate the trigger delay.

The optimal values of the chip registers were found to be $V_{fp} = 150$ and $V_{fs} = 20$. Such settings allow to avoid post-selection of the events corresponding to the digitisation of maximum of the signal pulse since the signal pulse is wide enough to be almost constant within the clock period. Also, the optimal chip settings increase the signal amplitude by a factor of $\simeq 2.5$, while the baseline width enlarges only by a factor of $\simeq 1.8$.
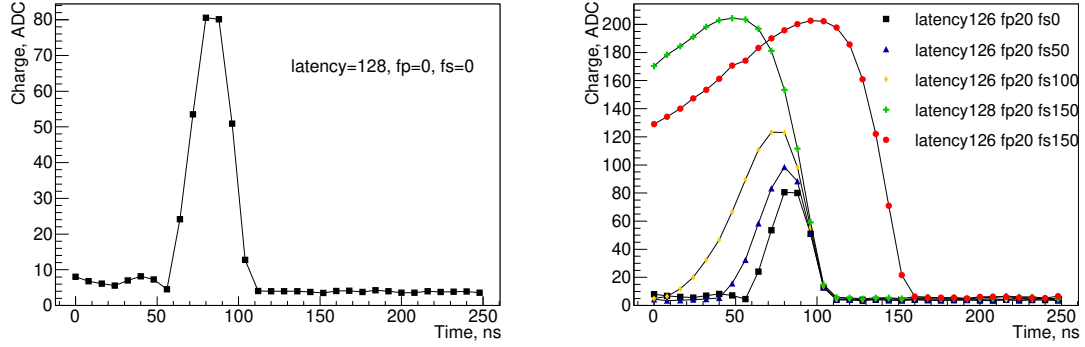
Figure 3.17: Pulse shape for the default (left) and alternative (right) settings of the *Beetle*.
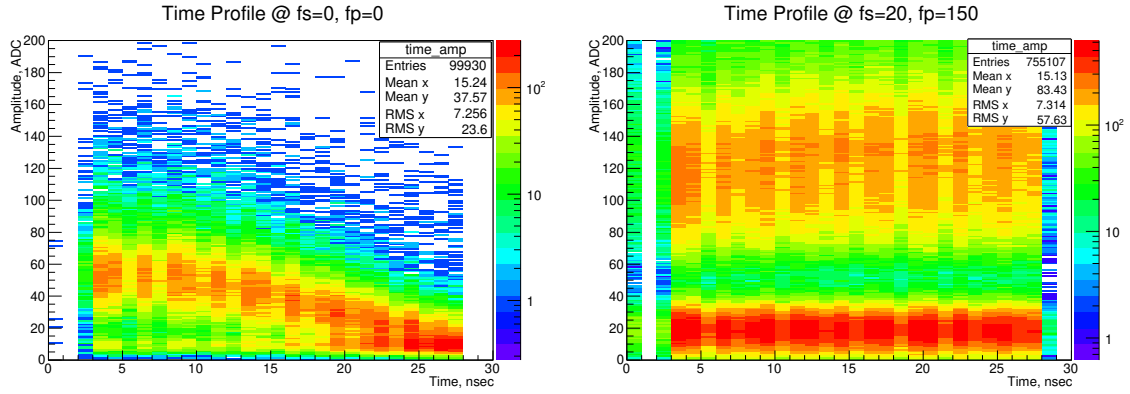
Figure 3.18: Time profile for the default (left) and optimal (right) chip settings.

3.2.2 Measurement setup

Silicon micro-strip sensors are very sensitive to environmental conditions: light, temperature, humidity and dust particles can significantly affect their performance. To avoid this, a light-tight, shielded, thermal enclosure for signal measurements was constructed.

3.2.2.1 Thermal enclosure and mechanical integration

The measurements were performed in a custom-made light-tight thermal enclosure with temperature and humidity control (see Fig. 3.19). As it was shown in Sec. 3.1.2, the leakage current reaches values below $\sim 0.4\,\mathrm{mA}$ at $20°C$ for irradiated sensors. According to Eq. 2.9, the cooling of sensors significantly suppresses the leakage current. Thus all the sensor characteristics including leakage current, bulk capacitance, charge calibration, signal and noise were measured at constant temperature of $-10°C \pm 1°C$ and relative humidity of $\lesssim 40\%$. Despite the cooling is not required for non-irradiated sensors, their study was performed in the same conditions for

consistency.
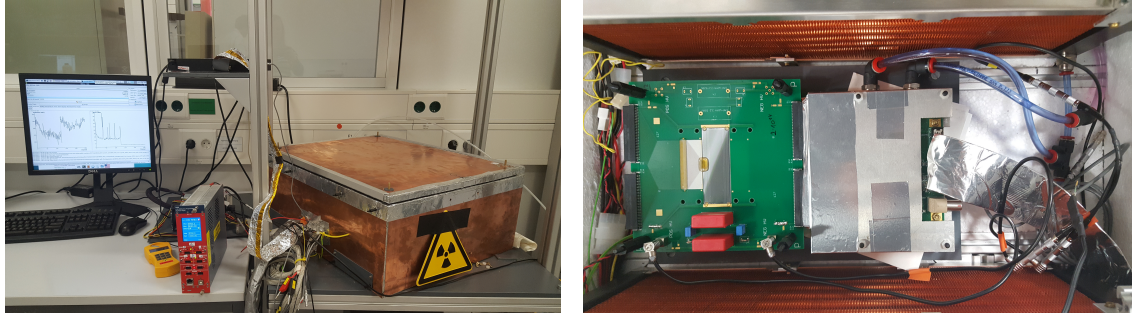
Figure 3.19: External (left) and internal (right) view of the thermal enclosure.

The thermal enclosure consists of a box and a cover; both are made of aluminium profile covered with thick copper foil soldered on the edges. It is additionally insulated with Styrofoam plates on the inside. The cooling power is provided by circulation of the glycol-water mixture through two copper heat exchangers inside the box. Each of the heat exchangers is equipped with two 6 cm fans to enforce air convection in the box volume. The glycol-water mixture is delivered via thermally insulated rubber pipes from the Lauda chiller. The Lauda thermostat can be accessed remotely via USB port with a dedicated software. The lowest possible temperature of the cooling liquid for this setup was found to be $-23°$C which corresponds to an air temperature of about $-13°$C in the box; however, the nominal limit for the chiller is $-40°$C. The thermal cycle from room temperature to $-10°$C in the box takes about 1.5 h. Room temperature nitrogen gas from a pipeline was constantly blown into the box to keep the relative humidity low.

A drawing of the setup is depicted in Fig. 3.20. The sensor PCB is mounted on a PVC (polyvinyl chloride) plate with 20 mm plastic spacers. An aluminium plate of 5 mm thickness with a round hole of 4 mm diameter is put on top of the PCB with 26 mm spacers. The ^{90}Sr source in the acrylic protection is put on another 4 mm thick aluminium plate with a hole of 3 mm diameter; this plate is separated by 15 mm plastic spacers from the bottom one. The point-like radiation source is located in the centre of a $34 \times 34 \times 23$ mm^3 acrylic cube. The source is centred with respect to the hole with a help of the PVC aligner (on top of the second aluminium plate): it has a rectangular pocket which fits the acrylic case of the source. There is a 25 mm thick plastic scintillator beneath the bottom PVC plate with a photomultiplier (PMT) attached via a light-guide to its side. There is a hole of $d = 8$ mm diameter in the PVC platform to let electrons from the source be absorbed by the scintillator without intermediate energy loss.

Electrons emitted by the ^{90}Sr source pass two aluminium collimators before they
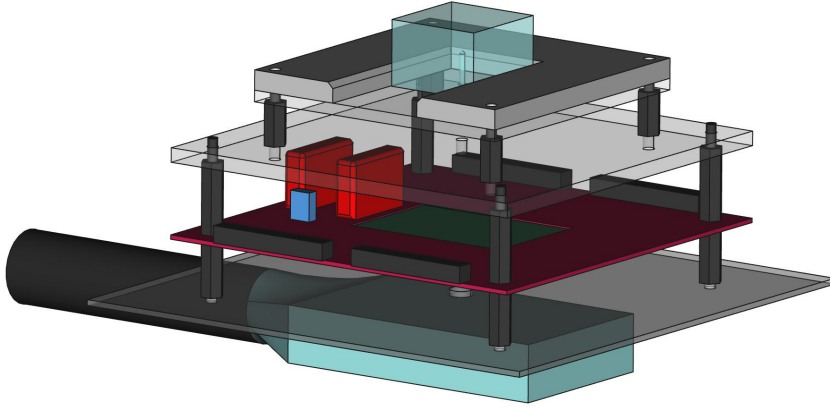
Figure 3.20: Schematics of the internal setup for sensor tests with a β-source.

reach the silicon sensor. In this way the electron beam is almost perpendicular to the sensor surface. The angular spread of the electron beam can be roughly estimated with the following relation:

$$\Delta\theta = \arctan\left(\frac{2l_2}{d_2}\right),\tag{3.5}$$

where $l_2 \simeq 35\,\text{mm}$ is a distance to the second collimator and $d_2 = 4\,\text{mm}$ is the diameter of its hole. Thus, $\Delta\theta \simeq 57\,\text{mrad}$, and the angle electrons cross the sensor surface is $\theta = 0°\pm3.3°$. With the distance $L \simeq 61.5\,\text{mm}$ from the source to the sensor the beam spot on the sensor surface is expected to be about of $\simeq 7.4\,\text{mm}$ diameter which is well consistent with a width of the readout sensor area $w = 128 \times 58\,\mu\text{m} = 7.42\,\text{mm}$. The solid angle under which the electrons cross the the sensor surface for the given setup configuration is $0.010\,\text{sr} = 8.3\times10^{-4} \times (4\pi)$.

As it was discussed in Chapter 2, the energy deposition in thin detectors almost does not depend on the particle total energy starting from values of $\gamma\beta = 1$. A thick plastic scintillator used to serve two purposes: to provide a trigger signal with a time-stamp which is required by the readout electronics (see Sec. 3.2.1) and to select only the electrons energetic enough to satisfy the above criterion.

The PMT attached to the scintillator was mainly operated at the voltage of $1.35\,\text{kV}$; being exposed to the ^{90}Sr source, it provided signals up to $\lesssim 120\,\text{mV}$ with the a rising edge of $\simeq 2\,\text{ns}$. The thickness of $25\,\text{mm}$ was estimated to be sufficient for the total absorption of $2.28\,\text{MeV}$ electrons emitted by the decaying ^{90}Y isotope. The signal amplitude was assumed to be linearly proportional to the electron energy.

The Alibava Systems© DAQ software allows to set a threshold up to $200\,\mathrm{mV}$ for the input analogue trigger signal. The threshold of $60\,\mathrm{mV}$ cuts the electron spectrum roughly in the middle: it corresponds to the selection of particles with kinetic energy above $\approx 1\,\mathrm{MeV}$ as it is shown in Fig 3.15. Variation of the threshold by $\pm 10\,\mathrm{mV}$ did not show any significant effect on the signal in the silicon detector; this observation is consistent with a flat dependency of the energy loss with respect to the particle energy in this region.

3.2.2.2 Customisation of the Daughter Board

The DBs provided by Alibava Systems© are designed to be directly wire-bonded to the micro-strip sensor. Each of the two *Beetle* chips is equipped with an aluminium-glass pitch-adapter with an outer pitch of $80\,\mu\mathrm{m}$. Some early prototypes of the *Beetle*-based STS test modules were directly connected to this pitch-adapters; however, the uneven pitch ratio $80\,\mu\mathrm{m}/58\,\mu\mathrm{m} = 1.38$ did not allow a proper one-to-one connection of the micro-strips to the *Beetle* channels. In order to test multiple sensors with the same DB without reassembling of the bonded set-up, the DBs were equipped with a ERNI connector board fan-out. A photo of the customised DB is shown in Fig. 3.21.
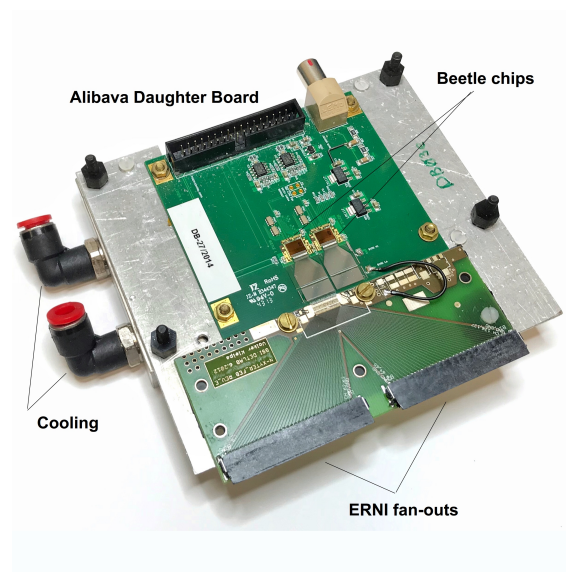
Figure 3.21: Customised DB of Alibava Systems©: the two ERNI connector fan-outs is mounted on the aluminium plate and wire-bonded to one of the *Beetle* chips.

Another particular issue of the DB operation is, that two ASICs produce heat during the system operation. Since the sensors had to be tested under cryogenic

conditions, an additional cooling of the DB had to be foreseen. For this purpose aluminium cooling blocks with glycol-water mixture circulation were used.

The DB was mounted on a 2 mm thick aluminium plate covered with Mylar© film to prevent accidental electrical contact. The insulation film was cut out in the region behind two *Beetle* chips: a layer of thin ($\simeq 0.2$ mm) thermally conductive rubber covered with heat-conductive paste was put. The PCB cut-off with two-ERNI connectors was mounted on the same support plate. The pitch-adapter of one of the chips was wire-bonded to the two-layer PCB with an effective pitch of $100\,\mu$m. This structure was attached to the cooling block and shielded with the aluminium cover for mechanical and electromagnetic protection of the electronics.

3.2.2.3 Printed circuit board for the sensor readout

The readout electronics preamplifier inputs have to be attached to the sensor strips. For the STS sensors the strip width is $58\,\mu$m; special tools are required to enlarge the pitch to a more convenient scale. For this purpose dedicated printed circuit boards (PCB) in three form-factors to host micro-strip silicon sensor prototypes were designed. A layout of the particular PCB for 62×42 mm^2 sensor is shown in Fig. 3.22.
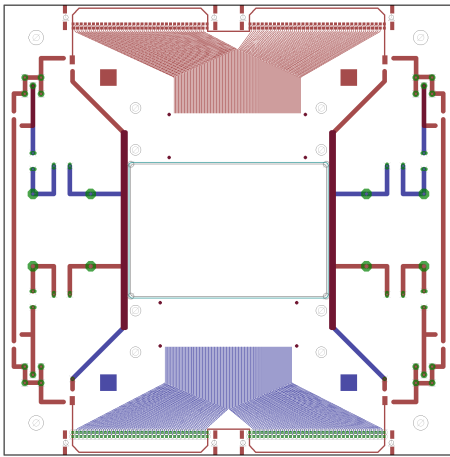
Figure 3.22: The layout of the PCB for a 62×42 mm^2 sensor.
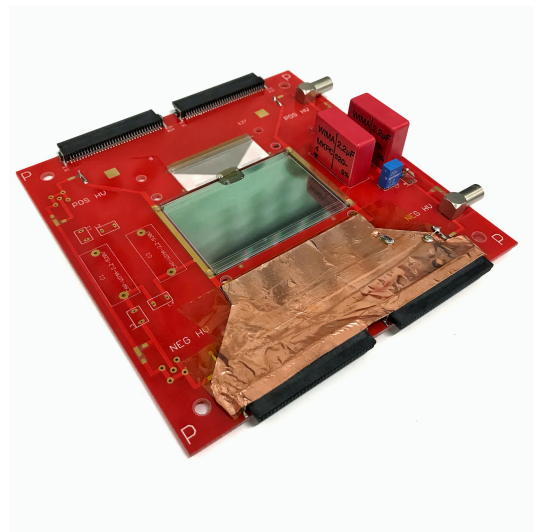
Figure 3.23: PCB with a 62×42 mm^2 sensor; the signal lines are partially covered with copper foil. The elements of the voltage filter are mounted on the right-hand side.

The outer dimensions of the PCBs are $140 \times 140 \times 1.7$ mm^3. They have a sufficient area to hold four 64-pin ERNI connectors attached to the two ceramic-aluminium

pitch adapters. They scale the pitch size from $58\,\mu$m on the sensor side to $200\,\mu$m on the PCB. The pitch adapters are connected to the PCB and to the sensor connection pads with $20\,\mu$m thick aluminium wire-bonds using the ultra-sonic welding technique. The sensor is placed in the centre of the PCB in the milled-out rectangular hole. The edge of the hole has a balcony structure to glue the sensor on; in this way the sensor is placed symmetrically with respect to the horizontal plane of the PCB. Fig. 3.24 depicts three sensors of different size installed in the corresponding PCBs.
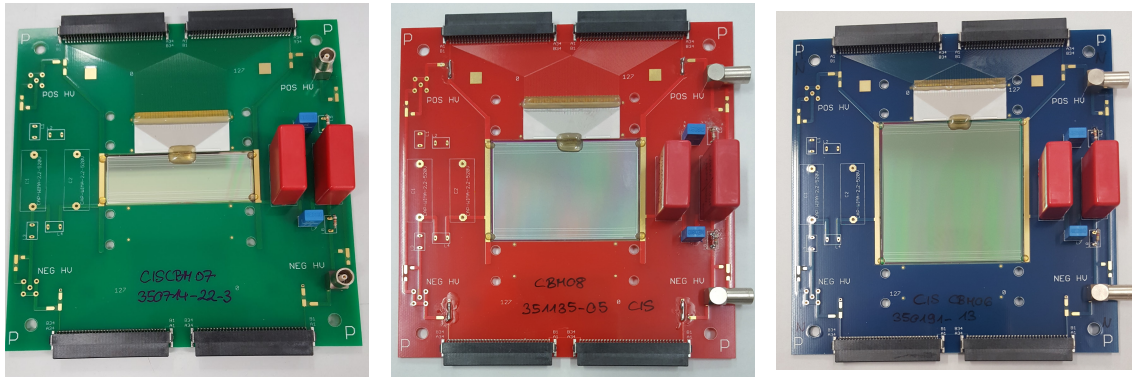
Figure 3.24: Sensors of three form-factors installed in the custom made PCBs (left to right): $62\times22\,\text{mm}^2$, $62\times42\,\text{mm}^2$, $62\times62\,\text{mm}^2$.

Such a configuration allows to read 128 central strips of each sensor side. The position of the pitch-adapter on the p-side is shifted to account for the strip stereo angle of $7.5°$. Thus the overlapping area of the p-side and n-side strips is located strictly in the centre of the sensor. The value of the horizontal shift of the p-side pitch-adapter alters from $1.32\,$mm to $3.95\,$mm, from the smallest to the largest STS sensor, see Fig. 3.25.

The sensors are glued into the PCB balcony with Araldite 2011. Then the UV-curing Epoxy, Polytec UV-2249 (for the contour dam) and Polytec UV-2257 (infill of the glob-top) was used to protect the wire-bonds. The glob-top protection was applied with an automatic dispenser for the dam and manually for the fill. The impact of the glue on the sensor performance was studied in Sec. 3.1.5.

The bias voltage is provided to the sensor via the wire-bonds on its corners. There is a low-pass LCR filter on the PCB to prevent the high-frequency contamination entering the sensor. The schematics of the filter is shown in Fig. 3.26. The large resistors at the input of the filter are important for the proper operation of the high-voltage source. With such a filter we observed a significant suppression of the HF noise coming from the voltage source.

The copper traces on the PCB conducting the signal from the sensor, together
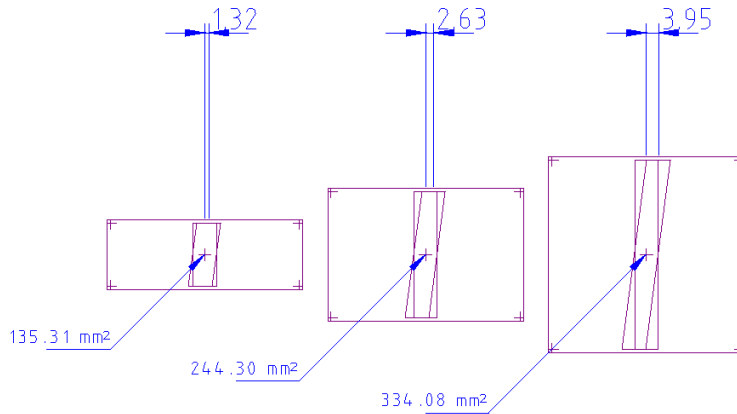
Figure 3.25: The horizontal offset and the area of the overlapping hexagonal area of the connected 128 central strips for the three main form-factors of the STS sensors.
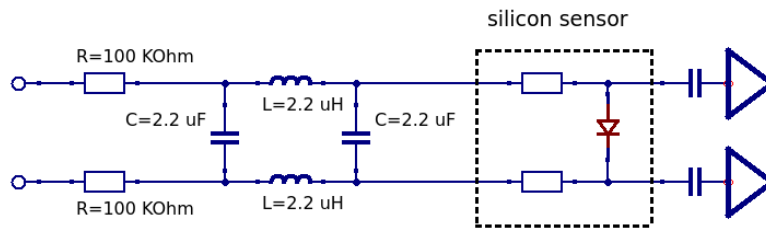
Figure 3.26: The schematics of the low-pass filter on the sensor PCB; the components in the dashed black box represent the sensor.

with the pitch-adapters were covered with grounded copper foil. It was done in order to protect the signal lines from the ambient RF contamination. The partially covered PCB with a $62 \times 42\,\mathrm{mm}^2$ sensor is shown in Fig. 3.23.

3.3   Evaluation of the sensor signal

The Alibava Systems$^©$ electronics allows to perform an internal charge calibration of the *Beetle* chip with or without external capacitive load (which is a silicon microstrip sensor in our case). The internal pulse generator produces pulses of current of known amplitude and duration; after the delay they are read out by the adjusted preamplifier and are digitised. In this way one can find a proportionality between the charge induced by an incident particle, and an amplitude in ADC units registered in the detector [115]. The typical set of calibration curves for 128 connected channels of the detector module is shown in Fig. 3.27.

Assuming a linear dependence of the voltage amplitude on the incident charge
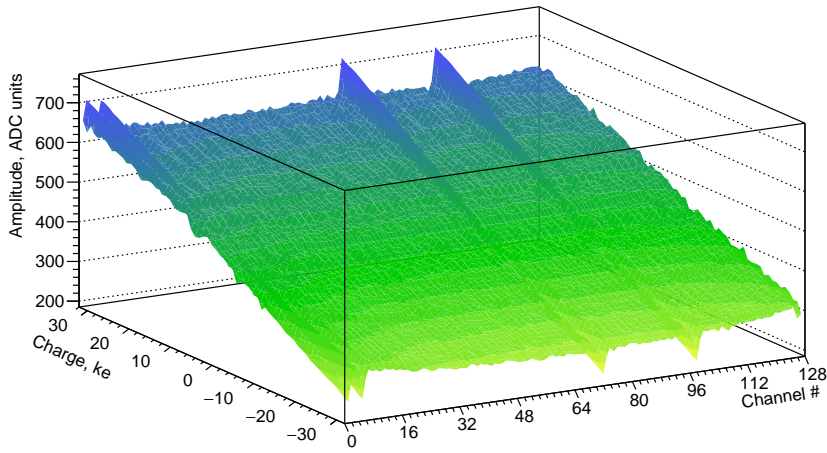
Figure 3.27: Typical plot for the calibration procedure for a *Beetle* chip with an attached silicon micro-strip sensor. For each of the 128 channels there is a set of probe charges being injected to obtain the corresponding amplitude in ADC units.

one can make a set of 128 fits with a first order polynomial function. The slope of such a function is shown in Fig. 3.28 for $62 \times 42 \, \text{mm}^2$ and $62 \times 62 \, \text{mm}^2$ sensors. The slope of the calibration line (also referred to as channel gain) significantly depends on the capacitive load of the preamplifier.
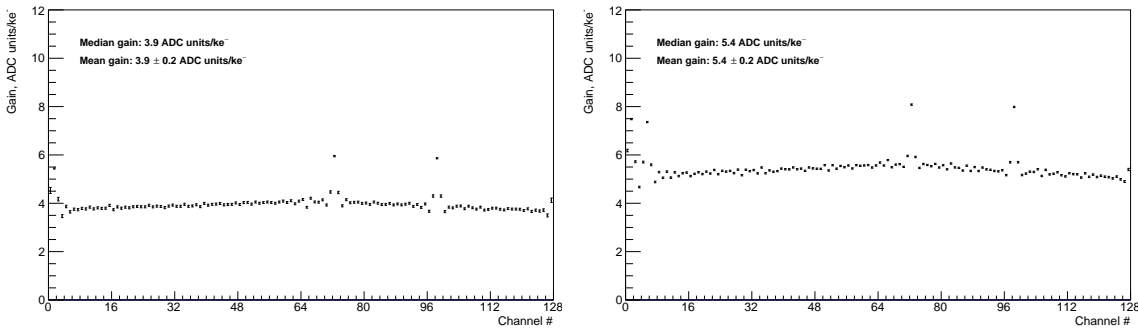
Figure 3.28: Typical gain values for $62 \times 42 \, \text{mm}^2$ and $62 \times 62 \, \text{mm}^2$ sensors.

The bulk capacitance of the sensor remains unchanged after irradiation; thus the calibration curves for the given sensor also do not change. The typical values of the channel gain are found to be $(3.9 \pm 0.2) \, \text{ADC units/ke}$ and $(5.4 \pm 0.2) \, \text{ADC units/ke}$ for $62 \times 42 \, \text{mm}^2$ and $62 \times 62 \, \text{mm}^2$ sensors, respectively (default *Beetle* settings).

3.3.1   Noise estimation

In general, the noise is a property of the integrated system; it may depend on various
parameters: impedance of the circuit elements, quality of shielding, geometry and
length of the signal and bias voltage lines. Particularly, it is known that the 64-
pin ERNI connectors can introduce additional noise to the system because of the
capacitance and RF pick-up. Also, the integration time of the preamplifier defining
the bandwidth of the readout electronics leads to different sensitivity to particular
noise frequencies. Thus, a wider bandwidth makes the system more sensitive to
the HF noise component. The further analysis is based on a factorisation approach
which will be assumed for different noise components: the resulting noise consisting
of independent components is a quadratic sum of the individual inputs:

$$\Delta q_\Sigma = \sqrt{\sum_i \Delta q_i^2}. \tag{3.6}$$

Figure 3.29 shows noise patterns for the readout itself and with sensor attached.
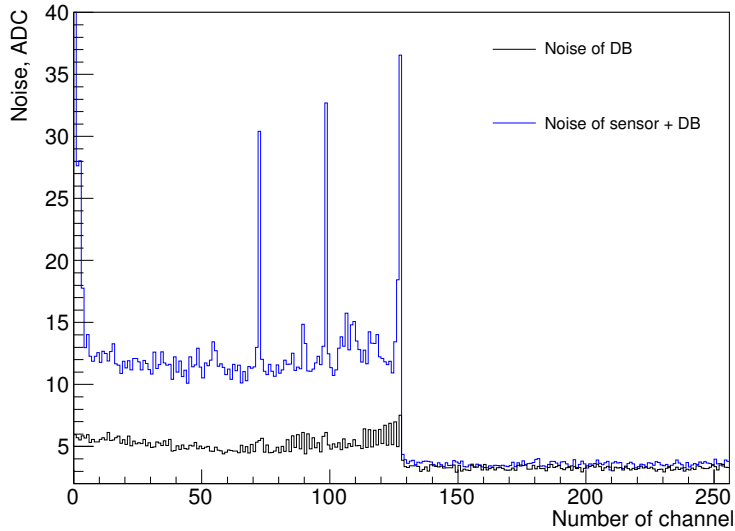
Figure 3.29: Noise patterns for the disconnected readout electronics (black line) and an irradiated
$62 \times 62 \, \text{mm}^2$ sensor at $500 \, \text{V}$ connected to the DB (blue line).

Here the increase of the noise with larger capacitive load is illustrated: silicon
sensor in PCB being attached to the readout electronics (channels 0 - 127) causes

about 13 ADC units of effect noise charge (ENC) while the DB itself is about half noisy. Channels 128 - 255 on the right hand side of the plot correspond to the second, disconnected *Beetle* chip and serve as a reference. One can see that the blue line in Fig. 3.29 exhibits two pronounced peaks around channels 0 - 2 and 126 - 127, which correspond to the edge of the ERNI-connectors. The edge channels act like antennas picking up RF from outside, additional shielding is required for them. Channels 72 and 98 were detached from the readout chip, thus high noise is present there.

In the further studies, a quadratic subtraction of the median DB noise value from the total noise for each channel will be performed. In this way it is expected to have an estimated value of the sensor intrinsic noise regardless of the DB contribution. Such a method is based on the factorisation approach; it is simplified, though it gives a valid estimation of the sensor ENC, which may later be used in the detector response simulation that involves different readout electronics.

To estimate the noise of the detector, data was collected with a pedestal mode of the Alibava Systems© DAQ software. These data fill 256 histograms; the full width of half maximum (FWHM) of each of the histogram is an estimate of the ENC for each channel. The root-mean-square (RMS) is estimated because of higher robustness against the out-lies: common baseline jumps and accidental signal events. The noise of individual channels for irradiated and irradiated sensors is illustrated in Fig. 3.30.
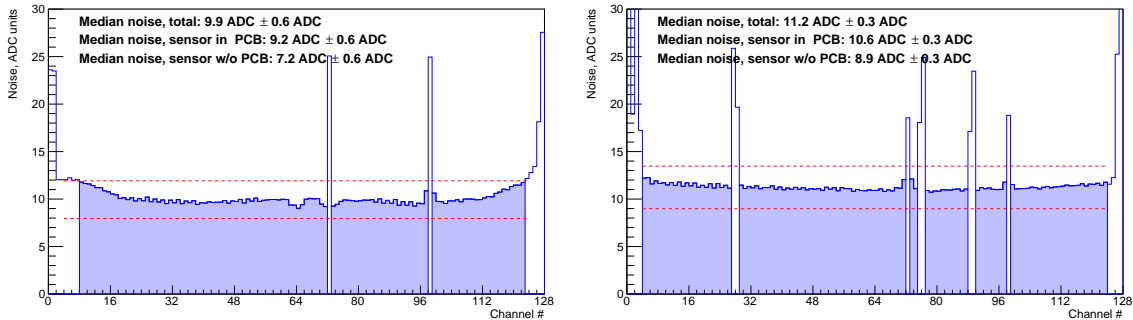
Figure 3.30: Individual channel noise for the non-irradiated `cbm06h6w72` sensor (left) and the double-lifetime irradiated `cbm06h6w79` sensor (right). The horizontal dashed red line indicates an acceptance window for the channels: those filled with blue are involved in the further data analysis.

The position of the baseline can vary from channel to channel for the particular setup (sensor in PCB and readout electronics). A mode (the value that appears most often) of the baseline distribution is used to estimate a baseline; it is then subtracted from the amplitude, thus a 0 ADC value correspond to zero induced charge.

There can be fluctuations of the overall baseline level due to an imperfect bias voltage source, a contamination of the grounding, RF pick-up and other factors. These issues do not provide an information about the sensor quality, but rather are the property of the given setup, the quality of its components, and the laboratory environment. To correct for base-line jumps, a common mode correction was performed in the following way: for each event median value was calculated for every 64 channels (one ERNI connector) and then subtracted from every amplitude in the given event. The measurement of the individual channel noise is also useful for the evaluation of the channels for the further data analysis. Channels with a noise deviating by more than 20% from the median noise for a given configuration are excluded from the analysis.

In Fig. 3.31 one can see the change of the noise level with applied voltage of the irradiated HPK and CiS sensors.
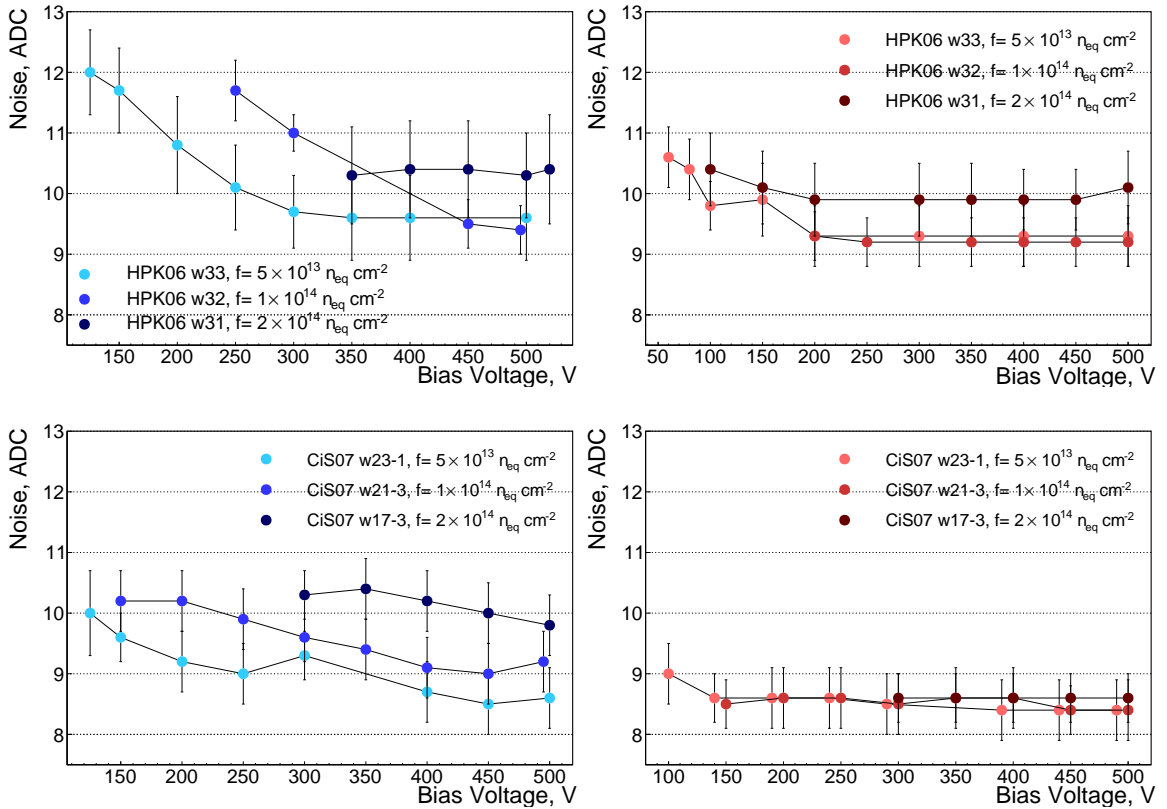
Figure 3.31: Median noise as a function of the bias voltage for p-side (left) and n-side (right) for sensors irradiated to different fluences: $62 \times 42 \, \mathrm{mm^2}$ HPK (top) and $62 \times 22 \, \mathrm{mm^2}$ CiS (bottom).

The noise level reaches saturation only after sufficient voltage applied. Lighter colour represents sensors exposed to lower dose $0.5 \times 10^{14} \, 1 \, \mathrm{MeV} \, n_{eq} \mathrm{cm^{-2}}$, bright

colour is for the lifetime fluence $1.0 \times 10^{14}\,1\,\text{MeV}\,\text{n}_{\text{eq}}\text{cm}^{-2}$ and the darkest colour denotes the double-lifetime fluence $2.0 \times 10^{14}\,1\,\text{MeV}\,\text{n}_{\text{eq}}\text{cm}^{-2}$. One can see that for the high fluences the noise on the p-side of the sensor continues to decrease even after $300\,\text{V}$ which is in the well over-depleted region. This effect is not pronouncing for the n-side of the same sensors.

Such a dependency can be partially explained by the decreasing sensor bulk capacitance with increased bias voltage. However, it does not explain the shift of the noise-voltage curve towards higher voltages after receiving more hadron fluence.

3.3.2   Signal induced by the ^{90}Sr source

Electrons from the ^{90}Sr radioactive source interact with silicon by generating electron-hole pairs (charge carriers) in the detector volume. The charge carriers start to drift in the electric field which is created in the depleted region because of the bias voltage. Drifting charge carriers induce currents on the readout strips of the detector; the pulse of current collected by charge sensitive amplifier (CSA) is then turned to the pulse of voltage with an amplitude proportional to the total collected charge.

Several effects influence the charge collection by the CSAs. The cloud of charge carriers broadens because of diffusion. Also, a parasitic interstrip capacitance leads to signal crosstalk in neighbouring channels. Thus, the signal charge is often spread between multiple strips (multistrip clusters), rather than being collected by a single readout channel (one- strip clusters). Both diffusion and cross-talk effectively decrease the total collected charge: residuals of the signals on the neighbouring strip may be too small to be considered as baseline fluctuations.

Another important issue is the geometrical suppression of the charge collected in the single channel: a particle with a significantly inclined track would cross several strips spreading the total induced charge over several channels. This effect is not expected in the present studies since collinearity of the electrons is within $\Delta\theta = 3.3°$, see. Sec. 3.2.2.1 for detailed explanations.

A few channels with an abnormal noise behaviour are excluded from the analysis; particularly, these are the edge strips and strips with broken or improper connections. The events with a single channel amplitude higher than $5 \times \sigma$ of the noise level are considered for further analysis. If the amplitude in the neighbouring channel exceeds the threshold of $3 \times \sigma$, it is also added to the resulting amplitude value; then it fills the signal distribution histogram.
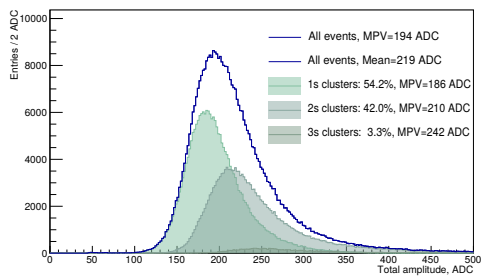
cbm06h2w06, f=0, MPV=194 ADC
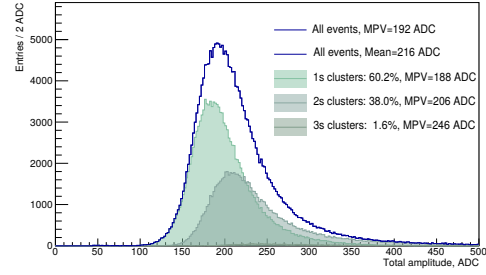
cbm06h2w06, f=5×10^{13}n$_{eq}$/cm^2,
MPV=192 ADC
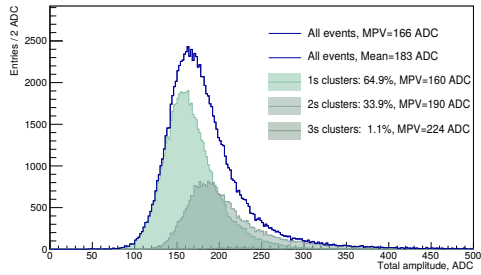
cbm06h2w08, f=1×10^{14}n$_{eq}$/cm^2,
MPV=166 ADC
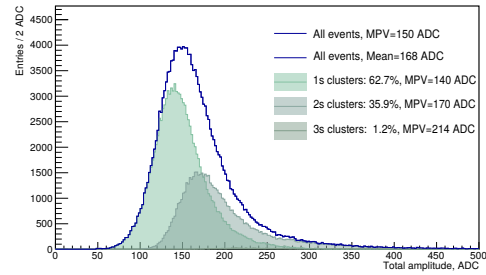
cbm06h2w02, f=2×10^{14}n$_{eq}$/cm^2,
MPV=150 ADC

Figure 3.32: Signal amplitude distribution and it's MPV (Most Probable Value) for the p-side of HPK 2×6 cm^2 sensors irradiated to different fluences.
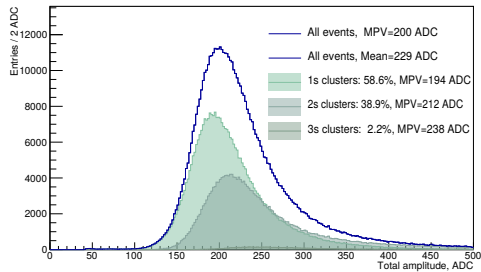
cbm07c2w21-3, f=0, MPV=200 ADC
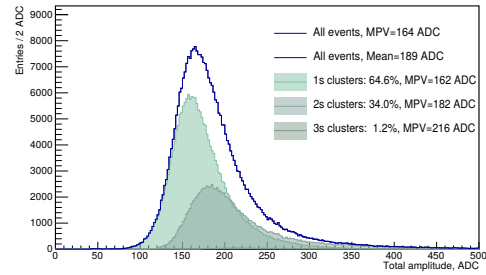
cbm07c2w22-3, f=5×10^{13}n$_{eq}$/cm^2,
MPV=164 ADC
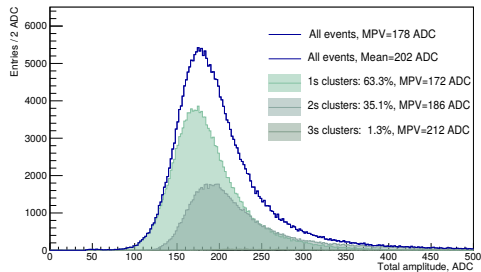
cbm07c2w21-3, f=1×10^{14}n$_{eq}$/cm^2,
MPV=178 ADC
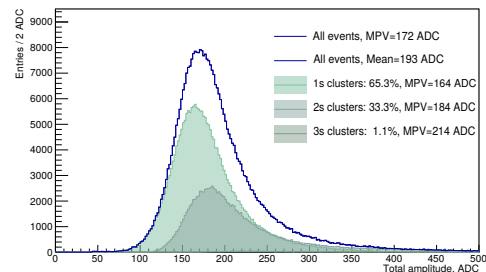
cbm07c2w17-3, f=2×10^{14}n$_{eq}$/cm^2,
MPV=172 ADC

Figure 3.33: Signal amplitude distribution and it's MPV (Most Probable Value) for the n-side of CiS 2×6 cm^2 sensors irradiated to different fluences.

The searching algorithm of the clusters starts from the strip with the highest signal-to-noise ratio and then moves to the left and to the right, stopping whenever the signal falls below the threshold.

Examples of the collected spectra a given in Figs. 3.32-3.33. One can notice a deterioration of the signal collected with irradiated sensors with respect to the non-irradiated ones. The signal of the irradiated to CBM lifetime dose sensor at $450\,\mathrm{V}$ bias is larger than 90% of that from the non-irradiated sensor. One can see, that most of the events are gathered by one strip; around $33\% - 38\%$ of events are registered in two-strip clusters. When particles crosses the detector perpendicularly, the number of three-strip cluster events is very small: $1\% - 3\%$. The results are similar for p- and n-side.

3.4 Data analysis and results

3.4.1 Most probable value of the signal

As an estimation of the collected charge, the MPV (most probable value) of the signal amplitude distribution for the given sensor is taken. The signal MPV can be compared to some model expectations (in charge or energy units) or to the reference measurements. The simplest approach, usually used for the comparison with already measured MPV, is to assume the full conversion of the energy loss in the silicon sensor to electron-hole pairs with further charge collection by CSA (about $24\,\mathrm{ke^-}$ for MIP crossing $300\,\mu\mathrm{m}$ of silicon). However, this approach is not used here.

Two quantities are used as a reference for the signal MPV: the baseline width in ADC units (noise estimation) and the MPV of the reference sensor (signal estimation). In this way, the signal-to-noise ratio (SNR) and the charge collection efficiency (CCE) are obtained. The values obtained for $62\times62\,\mathrm{mm^2}$ and $62\times42\,\mathrm{mm^2}$ sensors after irradiation were normalised to the non-irradiated reference from the same batch for the particular vendor of particular size. Sensors $62\times22\,\mathrm{mm^2}$ were measured before irradiation, thus were normalised to itself. The most probable value of each sensor is given in Fig. 3.34. Detailed characteristics of the signal spectra of all measured sensors are listed in Appendix A.
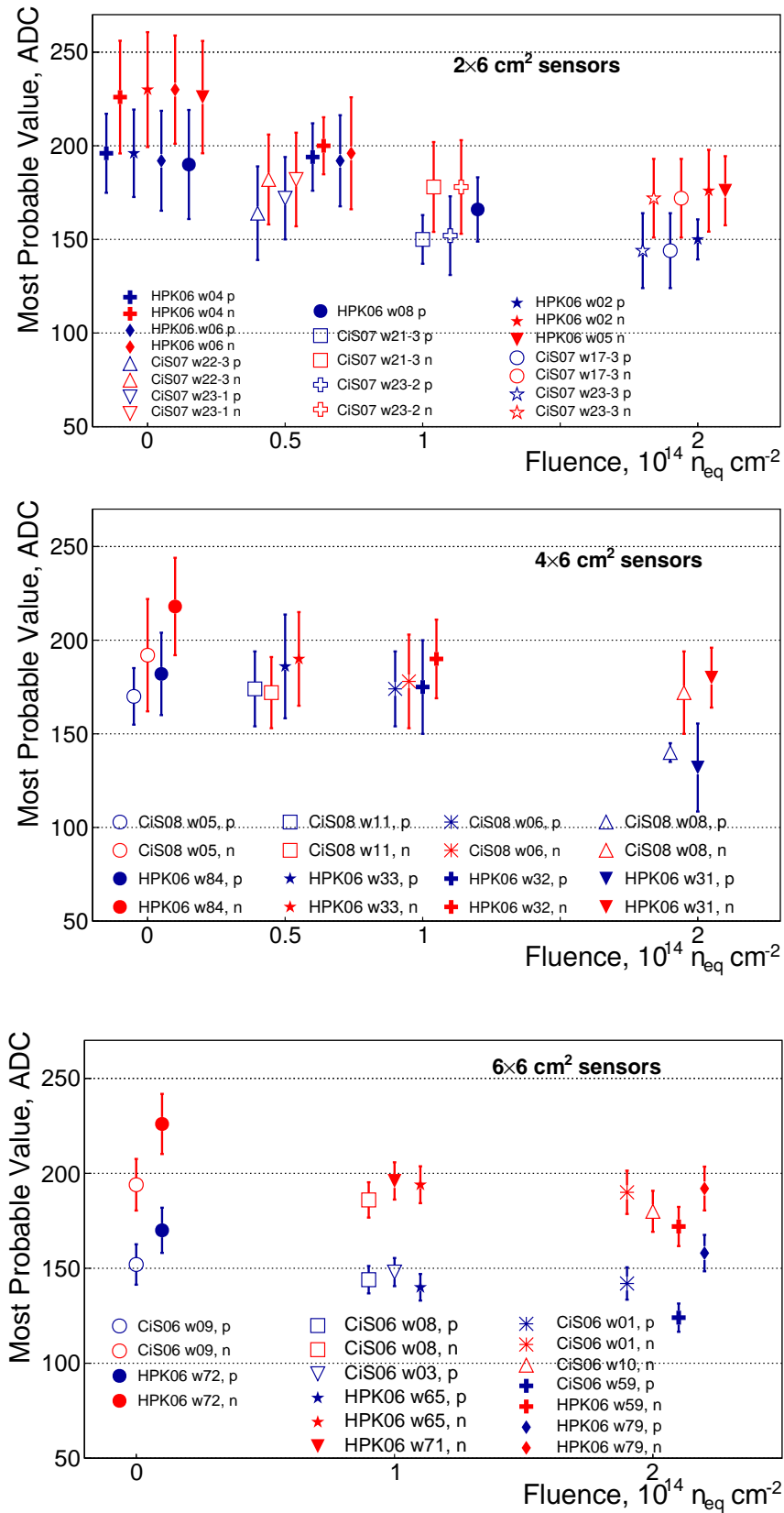
Figure 3.34: Most probable values of signal spectra for $62 \times 22\,\mathrm{mm}^2$, $62 \times 42\,\mathrm{mm}^2$ and $62 \times 62\,\mathrm{mm}^2$ sensors (from top to bottom) in ADC units as a function of the received fluence. Points corresponding to the same fluence are spread horizontally for illustration purpose.

3.4.2 Signal-to-noise ratio

For any application of silicon sensors in tracking detectors the focus is on the operating voltage needed to guarantee a sufficiently large signal-to-noise ratio (SNR) for detection of MIPs. The noise is controlled by operating the detectors at low temperatures. Typically the SNR value is expected to be lager than 10 for reliable operation of the tracking detectors [116]. The signal-to-noise ratio dependence for non-irradiated $62 \times 22 \, \text{mm}^2$ sensors on the bias voltage is shown in Fig. 3.35.
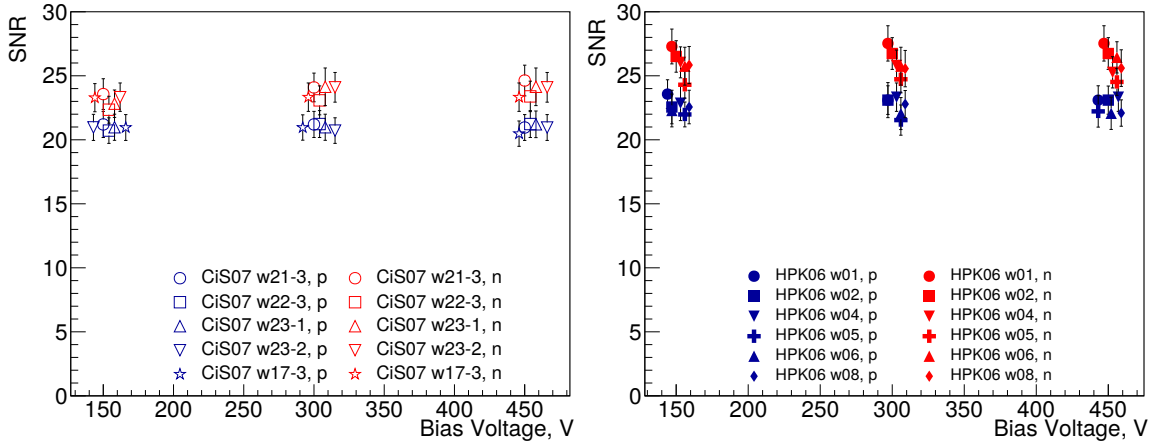
Figure 3.35: Signal-to-noise ratio for one-strip cluster events measured with non-irradiated CiS (left) and HPK (right) $62 \times 22 \, \text{mm}^2$ sensors in the ALIBAVA setup.
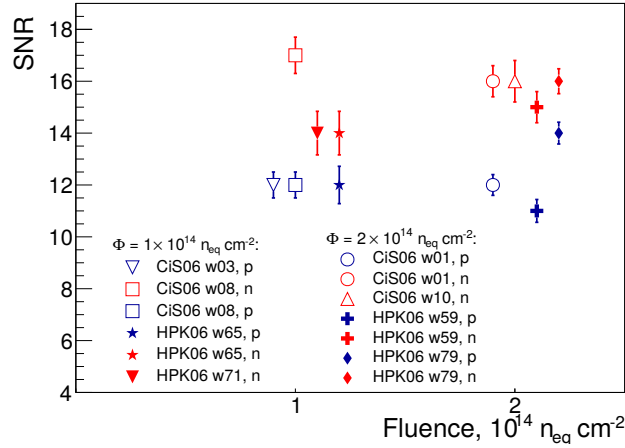
Figure 3.36: Signal-to-noise ratio for one-strip cluster events measured with $62 \times 62 \, \text{mm}^2$ sensors irradiated with a fluence of $10^{14} \, 1 \, \text{MeV} \, \text{n}_{\text{eq}} \text{cm}^{-2}$ (measured at $300 \, \text{V}$), and with $2 \times 10^{14} \, 1 \, \text{MeV} \, \text{n}_{\text{eq}} \text{cm}^{-2}$ (measured at $500 \, \text{V}$). Points corresponding to the same fluence are spread horizontally for illustration purpose.

Signal over noise of the system was calculated for one strip cluster events, where signal is the MPV of the spectra obtained from one strip events, noise is the median of channel baseline fluctuation [117]. All values were measured in ADC. It was measured at $150\,\mathrm{V}$, $300\,\mathrm{V}$ and $450\,\mathrm{V}$, which shows the same level of SNR at different bias voltages after full depletion.

In Fig. 3.36 signal-over-noise estimations for the irradiated $62\times62\,\mathrm{mm}^2$ sensors are shown. For a values $1\times10^{14}\,1\,\mathrm{MeV}\,\mathrm{n_{eq}cm^{-2}}$, the impact of the received fluence can be compensated by increasing bias voltage; however, the rising noise level deteriorates the SNR. Here, the sensors irradiated to life-time fluence have been measured at $300\,\mathrm{V}$, and for double life-time fluence the applied voltage was $500\,\mathrm{V}$.

3.4.3   Charge collection efficiency (CCE)

The CCE (Charge Collection Efficiency) of a non-irradiated sensor is defined to be 100%. The CCE for irradiated sensors was calculated as a ratio of the MPV measured after irradiation Δ_{irr} to the value observed before irradiation $\Delta_{\mathrm{non\text{-}irr}}$:

$$\varepsilon_q = 100\% \times \frac{\Delta_{\mathrm{irr}}}{\Delta_{\mathrm{non\text{-}irr}}} \tag{3.7}$$
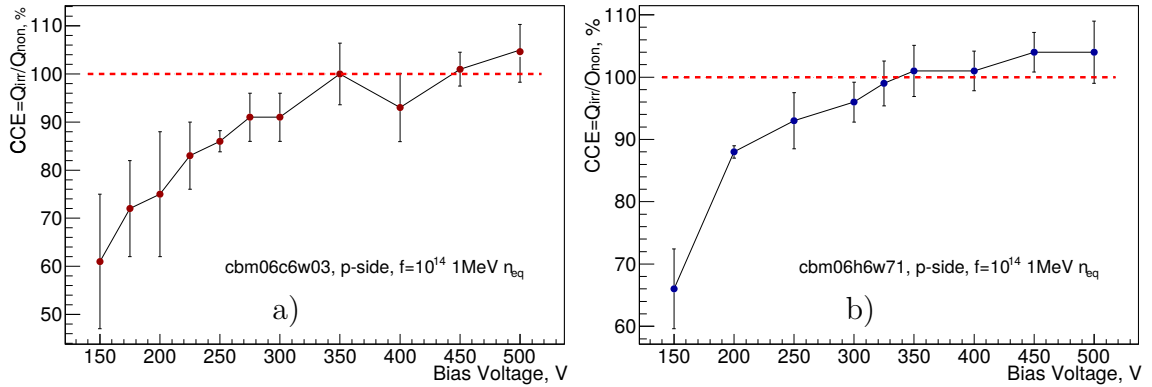
Figure 3.37: CCE as a function of the bias voltage for $62\times62\,\mathrm{mm}^2$ sensors irradiated to $1\times 10^{14}\,1\,\mathrm{MeV}\,\mathrm{n_{eq}cm^{-2}}$: a) `cbm06c6w03` (CiS); b) `cbm06h6w71` (HPK).

The CCE significantly depends on the sensor bias voltage. A particular reason is that the full collection of the charge deposited by interaction with MIPs can be only achieved in case of full depletion of the sensor when the electric field is spread through the sensor volume.

Non-ionising radiation causes defects in the silicon lattice; they act as traps for the charge carriers. To compensate this effect one has to apply higher bias voltage

in order to speed up the charge collection in the sensor medium. In Fig. 3.37 one can see how charge collection efficiency saturates at 100% when sufficient bias voltage is applied. At $\approx 350\,\text{V}$ the collected charge reaches saturation for the p-side of the sensors from CiS (left) & HPK (right) irradiated to $1 \times 10^{14}\,1\,\text{MeV}\,\text{n}_{\text{eq}}\text{cm}^{-2}$. When CCE exceeds 100%, this mean that normalisation was done not for this specific non-irradiated sensor, but for a sensor from the same batch and generation.

The depletion voltage after high fluences follows the Hamburg model [80]; after the inversion of the silicon type from n-doped to p-doped, the full depletion voltage monotonically rises with fluence.

Voltage scan results for sensors irradiated to different fluences are shown in Figs. 3.38 - 3.39 for p-side and n-side of the sensors. The colour gradient represents a higher level of fluence.
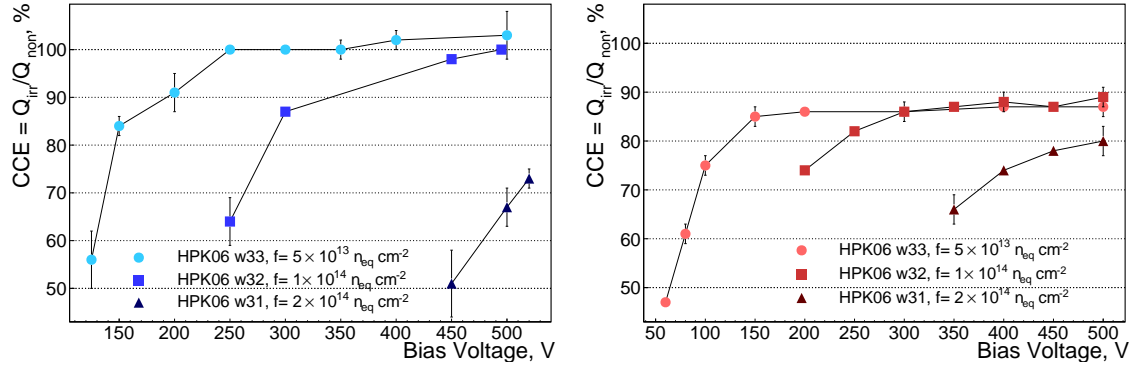
Figure 3.38: CCE as a function of the bias voltage for the p-side (left) and for the n-side (right) of $62 \times 42\,\text{mm}^2$ HPK sensors irradiated with fluences from 5×10^{13} to $2 \times 10^{14}\,1\,\text{MeV}\,\text{n}_{\text{eq}}\text{cm}^{-2}$.
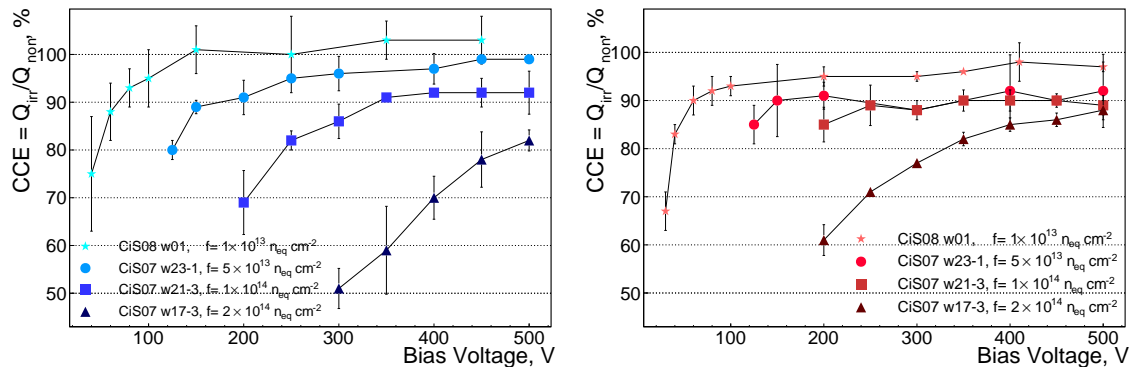
Figure 3.39: CCE as a function of the bias voltage for the p-side (left) and for the n-side (right) of $62 \times 22\,\text{mm}^2$ CiS sensors irradiated with fluences from 1×10^{13} to $2 \times 10^{14}\,1\,\text{MeV}\,\text{n}_{\text{eq}}\text{cm}^{-2}$.

One can see that sensor irradiated to $1 \times 10^{13}\,1\,\mathrm{MeV\,n_{eq}cm^{-2}}$ demonstrates the full depletion already at $150\,\mathrm{V}$. For sensors irradiated to $0.5 \times 10^{14}\,1\,\mathrm{MeV\,n_{eq}cm^{-2}}$ one has to apply at least $300\,\mathrm{V}$ in order to reach full collection of charge. Sensors irradiated up to $1 \times 10^{14}\,1\,\mathrm{MeV\,n_{eq}cm^{-2}}$ operate after $450\,\mathrm{V}$ of applied voltage. At double lifetime fluence one needs to apply at least $500\,\mathrm{V}$ in order to obtain reasonable signal from charged particles, but to make sensor depleted at these fluences becomes complicated. The p-side does not loss any charge at lower fluences, however the n-side collects 95% at most. It is also notable that the p-side performs differently at various fluences, meanwhile the n-side collects not more than 95% for all considered fluences [118].

The CCE results of $62 \times 22\,\mathrm{mm}^2$, $62 \times 42\,\mathrm{mm}^2$, $62 \times 62\,\mathrm{mm}^2$ sensors for different fluences is presented in Fig. 3.40. Sensors from both vendors behave similarly at the same fluence.

The final measurements for 36 irradiated sensors were performed at voltage of $450\,\mathrm{V} - 500\,\mathrm{V}$ which above the full depletion voltage of irradiated sensors. The performance of the $62 \times 22\,\mathrm{mm}^2$, $62 \times 42\,\mathrm{mm}^2$, $62 \times 62\,\mathrm{mm}^2$ sensors irradiated up to twice lifetime fluence is illustrated in Fig. 3.41. Blue colour represents charge collection on the p-side, red colour for the n-side. Empty markers are used for sensors produced by CiS, full markers are for HPK sensors. Triangle shaped markers denotes $62 \times 22\,\mathrm{mm}^2$, circles $62 \times 42\,\mathrm{mm}^2$ and squares $62 \times 62\,\mathrm{mm}^2$ sensors. Every single point corresponds to a separate measurement. When measurements from p- and n-side are presented below each other, these results belong to one individual sensor. Additional pictures of relative charge collection efficiency for both vendors at different fluences and method of error bars estimation are presented in Appendix B.

The results are consistent with the measurements performed for the miniature sensors irradiated to ta variety of doses, and for full-size sensors from older generations [92], [119], [120].
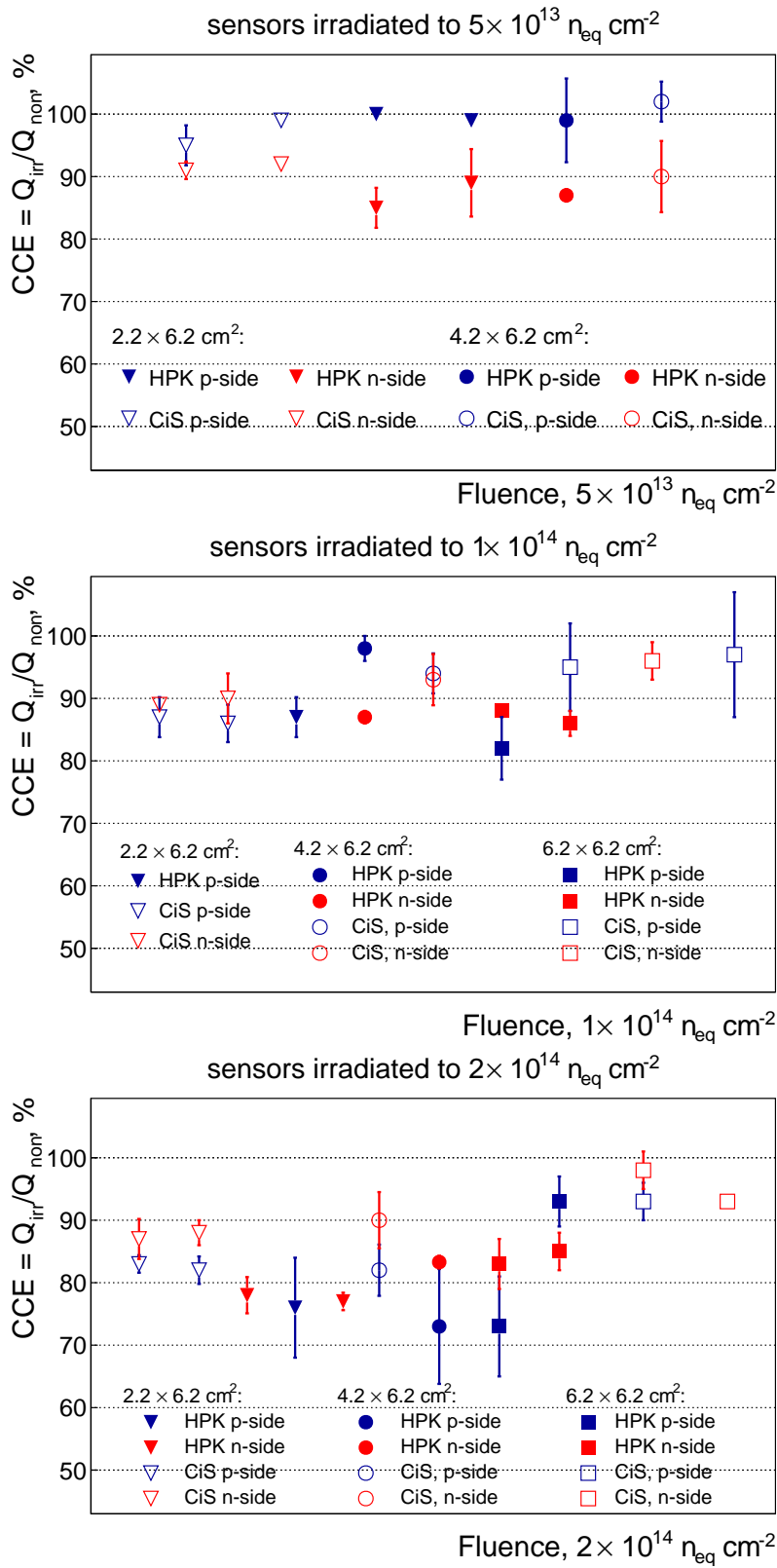
Figure 3.40: Charge collection efficiency as a function of fluence for sensors irradiated to 5×10^{13} (top), 1×10^{14} (middle) and $2 \times 10^{14} \, 1 \, \mathrm{MeV} \, n_{eq} \mathrm{cm}^{-2}$ (bottom).
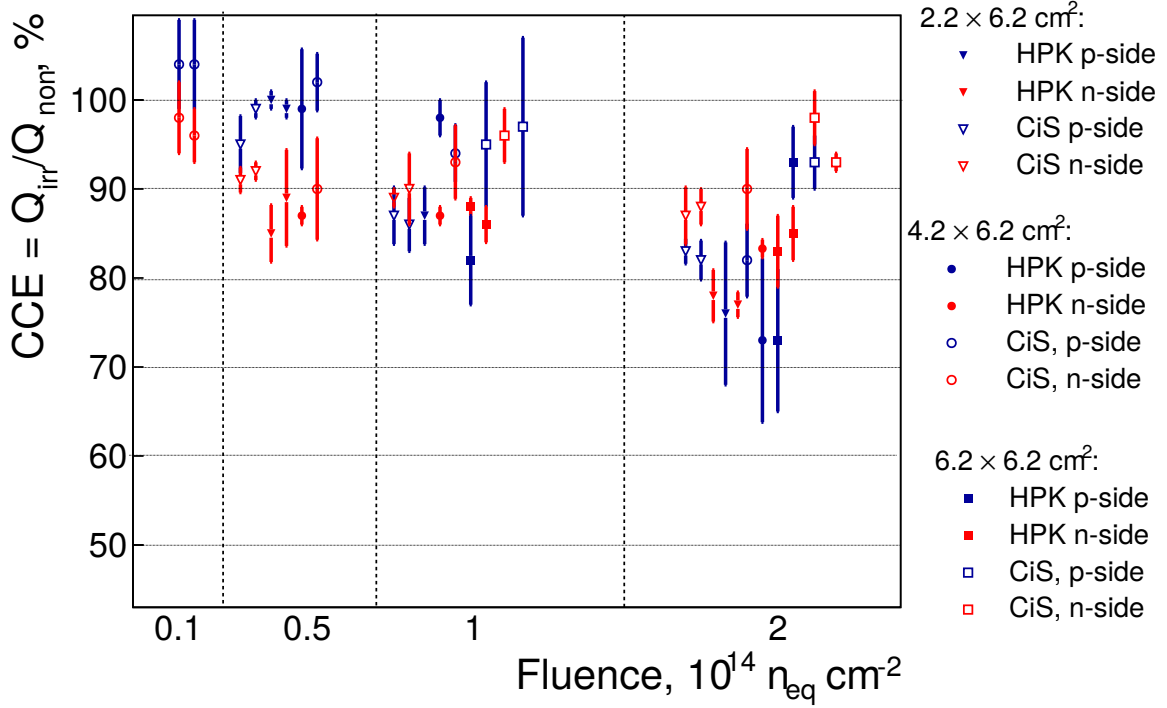
Figure 3.41: Charge collection efficiency as a function of the fluence for all studied STS sensor prototypes. Here, bias of $450\,V$ was applied to sensors irradiated to 0.1×10^{14}, 0.5×10^{14}, $1 \times 10^{14}\,1\,MeV\,n_{eq}cm^{-2}$; $500\,V$ of bias was applied to sensors irradiated to $2 \times 10^{14}\,1\,MeV\,n_{eq}cm^{-2}$. Points corresponding to the same fluence are spread horizontally for illustration purpose.

3.5 Influence of radiation damage on the STS performance

The key aspect of the STS performance is its ability to provide reliable tracking information which is then used for the measurement of the momentum of charged particles. The main requirements for STS are:

- high track reconstruction efficiency ($> 95\%$);

- precise momentum determination ($\Delta p/p \sim 2\%$).

Simulations involving a realistic detector response model [121], which includes several important parameters, could shed light on the expected STS performance. Signal-to-noise ratio significantly affects track reconstruction efficiency and momentum resolution. During the operation of the CBM experiment, silicon sensors will be exposed to high radiation fluences, which will lead to a decrease of charge collection efficiency (CCE) and to enhanced noise. Within these studies, for sensors

irradiated up the lifetime fluence, it was found that the relative charge collection efficiency drops to 85% - 90% and noise increases by 10%. The absolute value of the noise level obtained from these studies cannot be applied to simulations, because the measurement system based on the readout with external trigger, whereas the final STS will be read out by the STS-XYTER chip which works in self-triggering mode. Therefore, as noise input to the simulations a realistic value obtained with final readout electronics has to be taken into account. According to the latest noise measurement of the fully integrated system (non-irradiated sensor + microcable + readout electronics), the level of noise is around $1500\,e^-$ - $2000\,e^-$ [122]. Thus, after irradiation, the level of noise possibly could increase to $2200\,e^-$. In order to be conservative, noise levels of up to $3000\,e^-$ has been used for the simulation.

Figure 3.42 demonstrates momentum resolution and track reconstruction efficiency as a function of momentum for different signal and noise levels. In these plots, black, red and green points correspond to 100%, 90% and 80% CCE, respectively. One can see, that for noise level of $2000\,e^-$, the STS performs like for non-irradiated sensors: the mean value of momentum resolution is about 1.5% - 1.6% and track reconstruction efficiency of 95.5% for fast tracks ($p > 1\,\text{GeV}/c$) are reached, even for the worst-case scenario with the CCE decrease by 20%.

At the noise level of $2500\,e^-$, the three CCE scenarios show a slightly different STS behaviour, although within acceptable margins: 1.6% momentum resolution and $\sim 94\%$ reconstruction efficiency. The inefficiency is prevalent at noise levels of $3000\,e^-$. While, the momentum resolution is still 1.6 - 1.8%, the reconstruction efficiency drops to 90% and 80% for a CCE of 90% and 80% respectively.
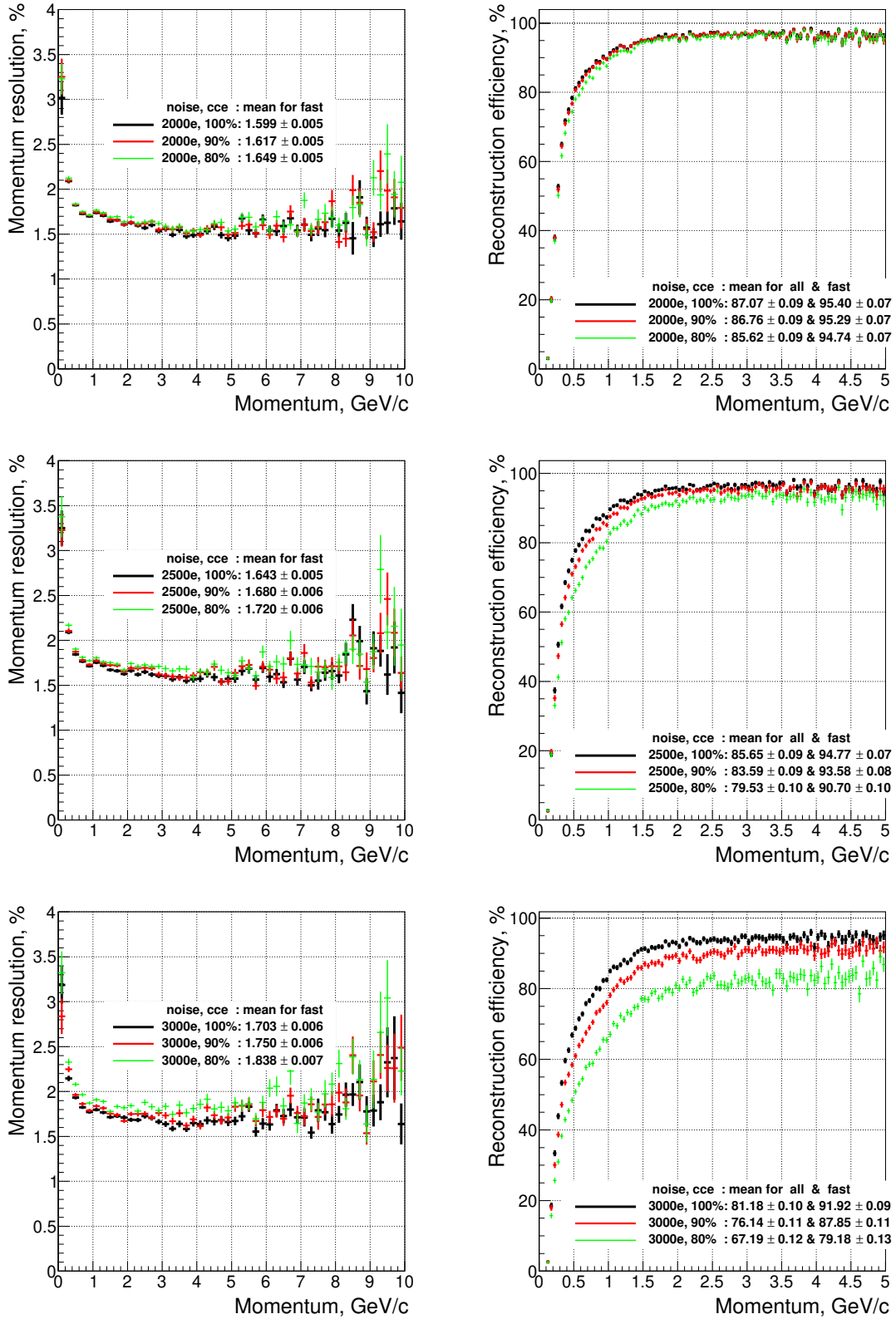
Figure 3.42: Momentum resolution (left) and track reconstruction (right) for all & fast ($p >$ $1\,\mathrm{GeV}/c$) tracks simulated at different noise levels: 2000 e$^-$ (top), 2500 e$^-$ (middle), 3000 e$^-$ (bottom) and at different collected charge levels: 100% (black), 90% (red), 80% (green points). Plots based on the realistic detector response model [121] simulation.

3.6 Summary

An extensive irradiation campaign was performed to evaluate the performance of irradiated sensors. Sensors from CiS and HPK, of different form-factors were studied for electrical characteristics and the charge collection efficiency (CCE). Because of the unavailability of the final readout electronics during the time of this thesis, Alibava Systems with external trigger was used to read out sensors.

The sensors from both vendors satisfy the performance requirements up to twice the expected lifetime fluence of $2 \times 10^{14}\,1\,\mathrm{MeV}\,\mathrm{n_{eq}cm^{-2}}$ in terms of leakage current and charge collection efficiency. All tested sensors survived high applied voltages up to $800\,\mathrm{V}$, although only voltages of up to $500\,\mathrm{V}$ are needed to operate sensors at CBM fluences. One of the prerequisites is to provide sufficiently low temperatures from $-5°\mathrm{C}$ to $-8°\mathrm{C}$ to minimize leakage current and to avoid annealing during sensor exploitation.

An absolute value of the 100% CCE has been defined as a signal amplitude of non-irradiated sensors for the particular vendor and size. CCE is calculated as a ratio of the charge collection measured after the irradiation to the value observed before the irradiation.

According to the realistic detector response model, with the decrease of charge collection efficiency up to 80% - 90% and expected increased level of noise due irradiation, the STS subsystem meets requirements in track reconstruction efficiency and momentum resolution.

4

Readout granularity at the periphery of the STS

The STS aperture covers polar angles from 2.5° to 25°. A readout strip pitch of $58\,\mu$m was chosen to match the design requirement of spatial resolution. About 900 sensors will be installed in the 8 stations of the STS, which translates into about 1.8×10^6 readout channels. To investigate, whether the amount of readout channels can be reduced in the outer aperture, and possibly increase the signal-to-noise ratio where tracks are inclined with respect to the sensor surface and the signal is shared by several neighbouring strips, different readout configurations between the sensor strips and electronics have been studied.

In order to check the detector performance with different strip pitch, a simulation with a realistic detector response model has been conducted. In Fig. 4.1, efficiency and momentum resolution for strip pitch of $58\,\mu$m, $116\,\mu$m and $174\,\mu$m are shown. The increase of the strip pitch leads to a drop of reconstruction efficiency from 96.5% to 92.2% for tracks with momenta above $1\,\text{GeV}/c$, and the momentum resolution deterioration from 1.6% to 1.9%. In particular, momentum determination for high momentum particles above $4.5\,\text{GeV}/c$ becomes more difficult and leads to a performance degradation.
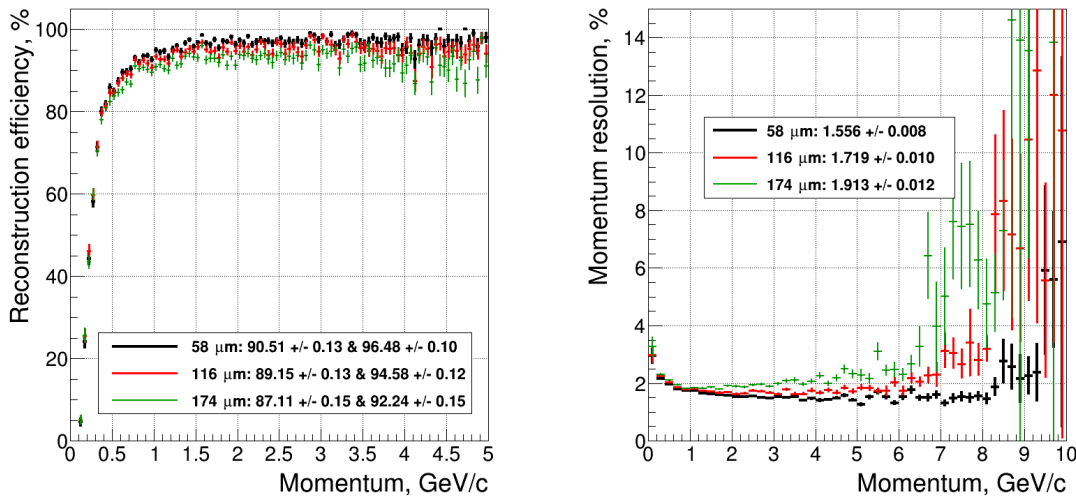
Figure 4.1: Track reconstruction efficiency (left) and momentum resolution (right) simulated for 500 Au+Au minimum bias events at $10\,A$GeV using realistic detector response model [123] with different sensor pitch: $58\,\mu$m, $116\,\mu$m, $174\,\mu$m.

4.1 Overview of interconnection schemes in other experiments

All high energy physics experiments, which use silicon microstrip sensors as tracking systems, are trying to find a compromise between sufficient spatial resolution and the amount of readout channels. Thus, detectors with larger readout pitch may be applied where incident particles cross the sensitive volume at larger angles. A short overview of interconnection schemes realized in different experiments is discussed below.

Belle experiment at KEK. The SVD [124] of the Belle experiment consists of concentric cylindrical layers of silicon sensors and covers full BELLE acceptance in the polar angle range $23° < \theta < 139°$. The strip pitch is $25\,\mu$m on the ϕ-side and $42\,\mu$m on the z-side. Adjacent strips are connected to one readout trace on the z-side which gives an effective strip pitch of $84\,\mu$m. The n-side strips are used for the z-coordinate measurement. Every other sensor strip is connected to readout electronics on the ϕ-side. Signals collected by floating strips are read out from adjacent strips by means of capacitive charge division.

D$_0$ experiment at Fermilab. The outer layers are consist of silicon sensors with $60\,\mu$m readout strip pitch, and provide hits essential for improved pattern recognition in a high occupancy environment [125]. In addition, two inner layers constructed with $50/58\,\mu$m readout pitch silicon sensors with intermediate strips at $25/29\,\mu$m,

provide precise coordinate measurements essential for good secondary vertex separation and excellent impact parameter resolution in the $r - \phi$ plane.

Double-sided silicon microstrip detectors for the PAMELA. The detector for the satellite mission [126] is based on a tracking system using a $300\,\mu$m thick n-type silicon wafers, with p-type strips of $25.5\,\mu$m pitch on the junction side. The readout pitch is actually $51\,\mu$m, since one strip is floating. Charge collected by this strip influences the output of the adjacent readout channels. On the other side (ohmic) n-type strips, orthogonal to the p-side segmentation, are implanted with $66.5\,\mu$m pitch. Spatial resolution was achieved at the level of $3\,\mu$m (junction side) and $12\,\mu$m (ohmic side).

Silicon Vertex Tracker (SVT) of the BABAR experiment at SLAC. The SVT [127] consist of double-sided silicon microstrip sensors with different interconnection schemes between readout electronics and sensors, as well as different strip pitch. To achieve the required spatial resolution, while keeping the number of readout channels as low as possible, most of the modules have a floating strip between two readout strips. Layers 1 and 2 are bonded at $100\,\mu$m and $110\,\mu$m pitch, respectively, with one floating strip. For the sensors of the last two layers, two strips are ganged to a single electronics channel.

4.2 Studies in the lab with perpendicular incident electrons

4.2.1 Configuration of the sensor under test

To conduct feasibility studies, three types of connections were realized on the p-side of a test board with a double-sided silicon microstrip sensor (see Fig. 4.2):

- each strip is read out by one electronics channel ($1 \rightarrow 1$);

- only every second strip is read out ($2nd \rightarrow 0$);

- when two strips are bonded to one readout channel ($2 \rightarrow 1$).

The interconnection schemes between sensor and readout are shown in Fig. 4.3. To investigate these three possibilities of interconnection, 384 sensor strips were divided in 7 groups and bonded to 256 readout channels of two Beetle chips. The bonding procedure was arranged to use all sensor strips, without any intervals between the connection groups. The same amount of 64 readout strips was used for each connection. One to one interconnection comprises four groups of 32 channels connected,

one omitted or floating scheme made of two groups of 64 sensor strips bonded to 32 readout strips, two to one realised on 128 sensor strips ganged to 64 readout channel

To reduce the number of readout channels only every second or third strip may be read out. Due to the large capacitance between neighbouring strips, the floating strips (when every second sensor strip is readout) contribute to the centre-of-gravity value [128].
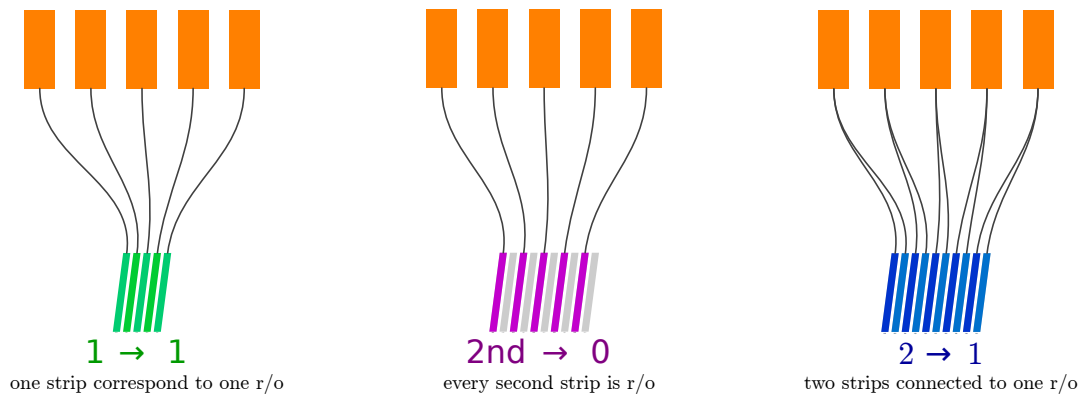
Figure 4.2: Schematic representation of different connection schemes: each strip is read out by one electronics channel ($1 \rightarrow 1$), when only every second strip is read out ($2nd \rightarrow 0$), and when two strips are bonded to one readout channel ($2 \rightarrow 1$).
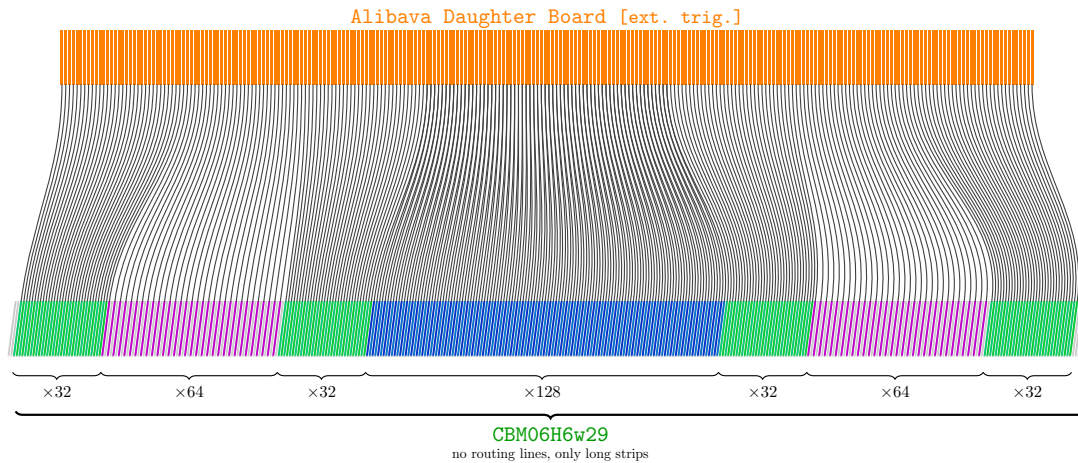
Figure 4.3: Schematic representation of the sensor strips bonded to readout (orange strips). Each group of connection represented via different color: $1 \rightarrow 1$ (green), $2nd \rightarrow 0$ (magenta), $2 \rightarrow 1$ (blue).

If sensor is readout only by every second strip, then charge collected on intermediate strip is seen by two neighbouring amplifiers. Because of the charge division between them, it is possible to reconstruct charge by the ratio of capacitances (in-

cluding the network of interstrip and decoupling[1] capacitances) of the neighbouring strip. This means that reconstruction of the hit occurring near a floating strip is also possible with high precision during the offline analysis. On the other hand, loss of charge is possible, because readout channels may suffer from higher capacitance of these connections.

4.2.2 Laboratory setup

The laboratory setup built for these studies is presented in Fig. 4.4. The assembly was mounted inside a light tight aluminium box, which has a movable support for a radioactive source on the top and a trigger scintillator on the bottom. The scintillator, sensor and collimated source were aligned for mainly perpendicular particles registration.
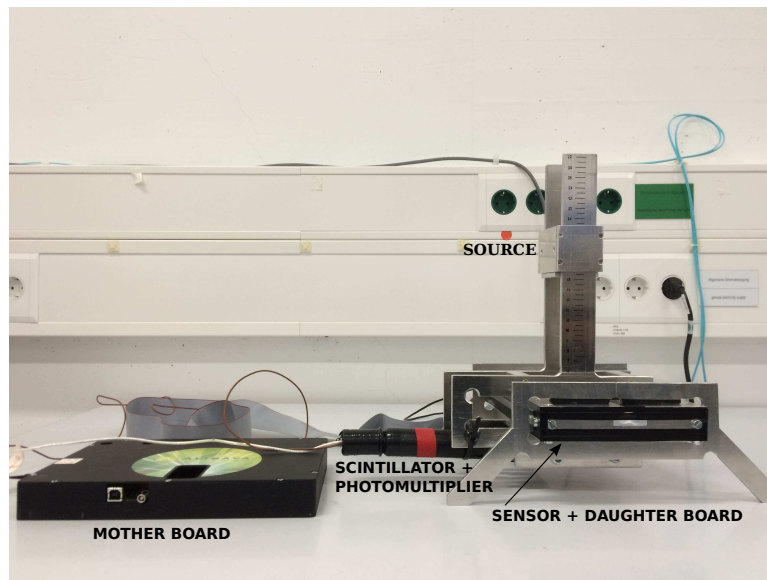
Figure 4.4: View of the experimental setup for perpendicular incident particles of a ^{90}Sr source.

The source and the scintillator are mechanically interconnected and can move simultaneously in the X and Y direction. The height of the source above the sensor can be independently adjusted. As a readout the Alibava system [114] was used. It employs the Beetle chip which was developed for the tracking system of the LHCb experiment [129]. The realisation of the bonding configuration is shown in Fig. 4.5. Here the central strips of the single-metal silicon sensor (left) were directly attached to the two Beetle ASICs (right) via intermediate pitch adapters.

---

[1]between strip and readout electronics

Figure 4.5: View of the microstrip sensor (left) directly bonded to the daughter board (right) of the Alibava system.
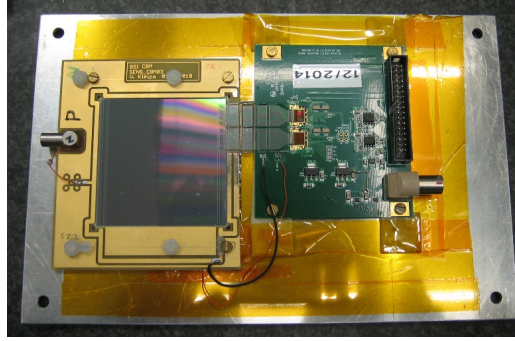
Figure 4.6 shows a calibration histogram for 256 connected channels, where different readout schemes were established. One can clearly see how gain values change with interconnection, because of introduction (in case of $2nd \to 0$) or deduction (in case of $2 \to 1$) of capacitance.
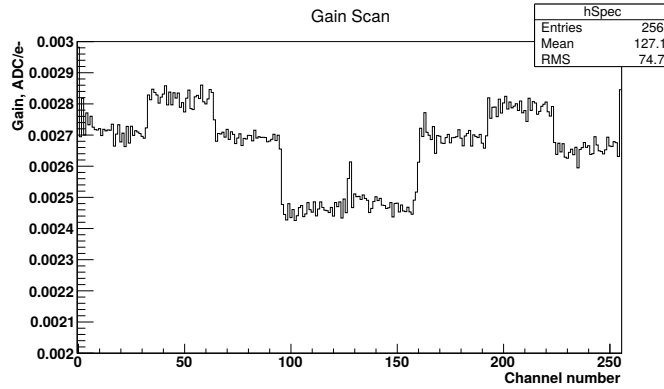
Figure 4.6: Calibration histogram for 256 sensor strips interconnected with channels of readout chip.

4.2.3 Noise

The noise is calculated as a fluctuation of the baseline for a given channel number. The noise for a particular connection type was determined from the mean value of all connected strips of this type:

- one to one: 2.58 ± 0.02 ADC;

- one omitted: 2.27 ± 0.04 ADC;

- two to one: 3.05 ± 0.05 ADC.

The noise histogram is presented as a function of the strip number in Fig. 4.7. Here, the noise measurement of the daughter board is shown by a black line; the blue line corresponds to the noise after the sensor was bonded to the readout electronics.
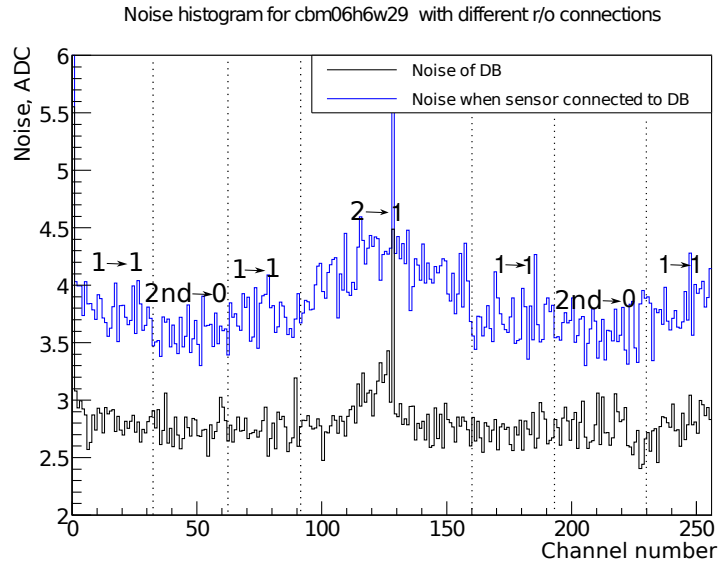
Figure 4.7: Noise as a function of strip number for `cbm06h6w29` biased to $150\,\mathrm{V}$ with three types of readout schemes indicated on the top of the histogram. Black dashed lines point to connection regions. Black curve represents noise of readout daughter board (DB) only, blue curve indicates noise of full system, when sensor is directly bonded to the readout electronics.
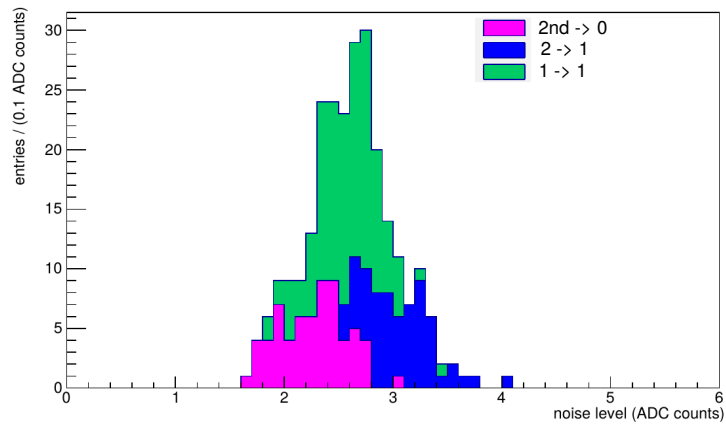
Figure 4.8: Noise histogram for `cbm06h6w29` sensor with three readout connection schemes.

Different kinds of connections are clearly distinguishable by the different levels of noise. Noise directly depends on the additional capacitance. When two sensor strips are connected to one readout strip the capacitance load is larger, than in the other two cases. One floating strip introduces less capacitance, than the connection of one sensor strip to one readout strip.

One can see in Fig. 4.8 the noise representation for three interconnections relatively one to another on the ADC scale. The green area depicts $1 \rightarrow 1$, blue shows $2 \rightarrow 1$ and magenta $2nd \rightarrow 0$.

4.2.4 Signal amplitude

The pulse shape can be reconstructed with help of the internal Time Digital Converter (TDC) in the range of 100 ns and a system clock with a period of 25 ns. The full pulse shape is restored by plotting the average of the signal as a function of the TDC measured. The time profile of the measured signal is shown in Fig. 4.9. One can see that collected charge lies in the range between $60 - 80$ ADC. To collect only the maximum of the signal, a time threshold range from 3 ns to 8 ns is applied for these studies.
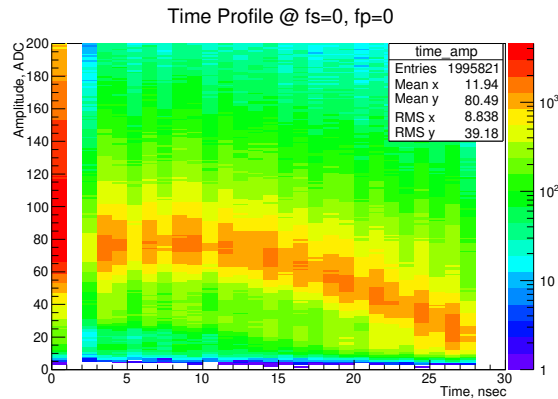
Figure 4.9: Signal time profile for the sensor bonded to the readout board at standard Beetle settings.

The obtained cluster charge spectrum was fitted with a Landau-Gaussian convolution. The most probable value (MPV) is interpreted as the collected charge. Examples of the obtained spectra for different cluster sizes are shown in Fig. 4.10. In this case, where most of the tracks are perpendicular, the signal is collected mainly by one-, two- or three strips. To realise the cluster finding algorithm, a threshold of $5 \times \sigma$ for the seed strip (strip with maximum signal amplitude) was applied, then the search was moved to the left or to the right neighbouring strip, and stopped when the signal amplitude fell below the threshold of $3 \times \sigma$.
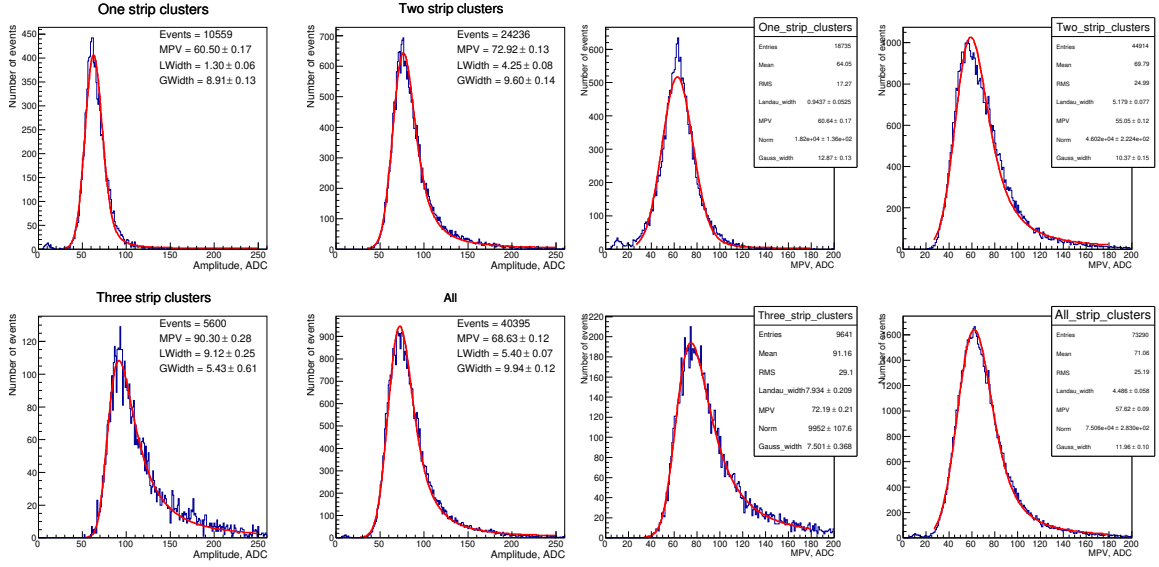
(a)

(b)
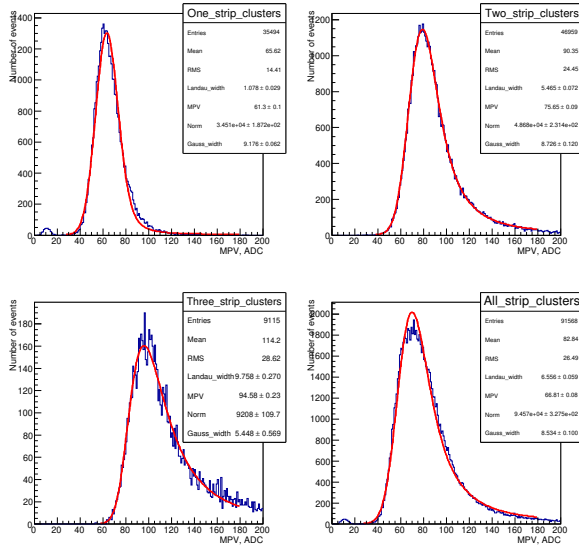
(c)

Figure 4.10: Signal amplitude for one-, two-, three- and all-strip cluster events with depleted sensor measured at $150\,\text{V}$ for different connection schemes: a) $1 \to 1$, b) $2nd \to 0$, c) $2 \to 1$.

4.2.4.1 Charge distribution between neighbouring strips

For the runs with normally incident particles, one can clearly observe charge division between neighbouring strips. This depends on the following sensor parameters: thickness, resistivity and applied voltage. In order to ensure over-depleted bias, the sensor was operated at $150\,\text{V}$; although V_{FD} for this particular sensors is $65\,\text{V}$. Non-linearity of charge division in the interstrip gap for perpendicular tracks in the case of 2-strip cluster events, can be shown with help of the η-function. It is defined as

the ratio between the charge collected on the left strip (Q_L) to the sum of charge amplitude on a both strips (Q_L and Q_R):

$$\eta = \frac{Q_L}{Q_L + Q_R} \tag{4.1}$$

Figure 4.11 shows examples of η-distribution for 2-strip cluster events in different connection schemes. As expected, the distributions are quite symmetric.
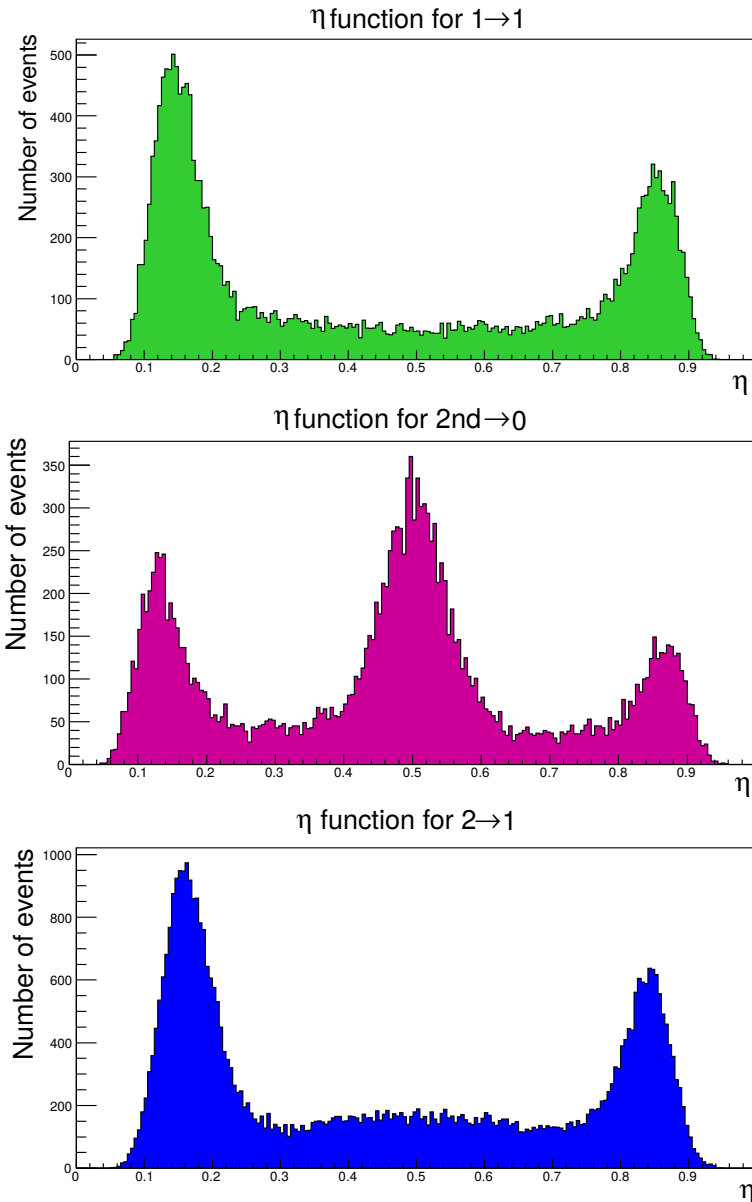
Figure 4.11: Eta-distribution for different readout bonding configurations: $1 \rightarrow 1$ (top), $2nd \rightarrow 0$ (middle), $2 \rightarrow 1$ (bottom) connections.

The η-distribution depends on the coupling capacitance, which moves the peaks closer to the center ($\eta = 1/2$) and on the noise of the detector, which broadens the peaks, as one can observe in the histograms above. The broader the peak of the η-function, the more difficult it is to determine the position of the passage of the charged particle, which complicates the track reconstruction procedure.

If charged particles cross the sensor in the middle of the two strips, then its charge is equally divided between them. But if particle deviates from the middle, then its charge will be collected mostly by the left or the right strip (see Fig. 4.11 top), which means in terms of η-function closer to 0 or 1. The peak at $\eta = 1/2$ appears, when a floating strip is introduced (see Fig. 4.11 middle), so that the hit reconstruction remains possible with a floating strip. When two sensor strips are connected to one readout strip, coupling the capacitance increases and loads the readout circuit much more than in the other connection schemes. Here, the charge cloud is observed between two readout strips (see Fig. 4.11 bottom). Although only two readout strips are used, effectively four sensor strips are readout.

4.2.4.2   Charge collection dependence on applied voltage

The signal dependence on the applied voltage is presented in Figs. 4.12-4.13. Here, the plateau after full depletion is observed, the charge collection curve has quite similar behaviour for the $1 \rightarrow 1$ and $2 \rightarrow 1$ connection scheme, while for the floating strips the saturation occurs earlier. Although the full depletion voltage for non-irradiated sensors of this type is about $65\,\mathrm{V}$, the charge collection reaches its plateau after $100\,\mathrm{V}$ for a $2nd \rightarrow 0$ scheme, and at $120\,\mathrm{V}$ for the $1 \rightarrow 1$ and $2 \rightarrow 1$ connections.
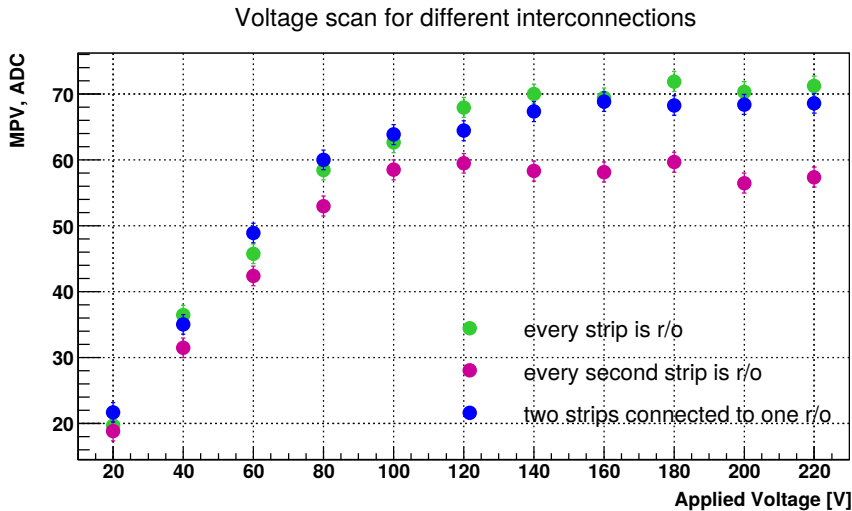
Figure 4.12: Signal amplitude dependence on the applied voltage for all-strip cluster events.

(a)

(b)

(c)
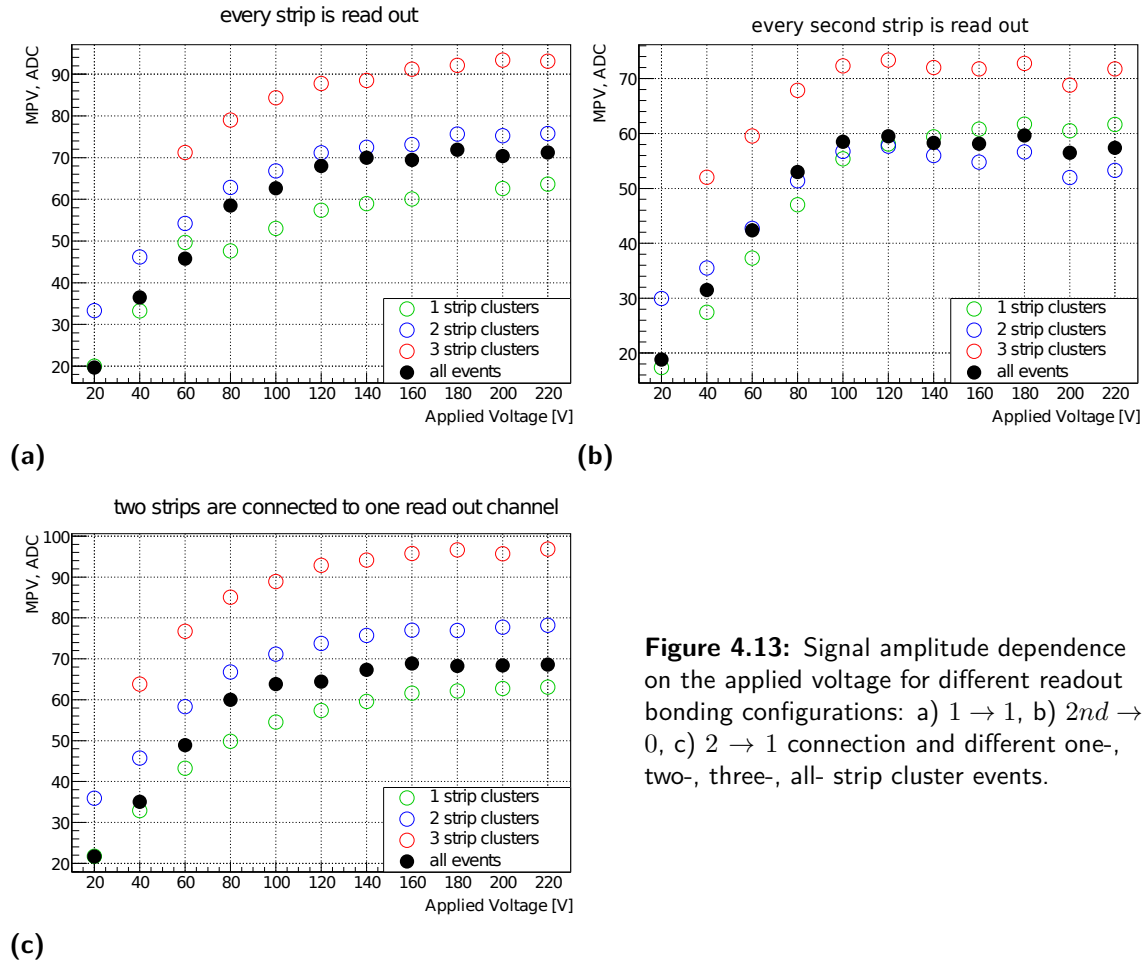
Figure 4.13: Signal amplitude dependence on the applied voltage for different readout bonding configurations: a) $1 \rightarrow 1$, b) $2nd \rightarrow 0$, c) $2 \rightarrow 1$ connection and different one-, two-, three-, all- strip cluster events.

4.2.5 Signal-to-noise ratio

The spatial resolution of silicon microstrip sensors is mainly determined by the pitch between sensor strips, and by the signal-to-noise ratio. If the charge of the incident non-perpendicular particles is not shared between strips, then the spatial resolution of 1-strip clusters arising from geometrical considerations is:

$$\sigma^2 = \frac{p^2}{\sqrt{24}} \tag{4.2}$$

If charge sharing is present, and the signal is distributed over several neighbouring strips, then the intrinsic detector resolution has two main contributions:

$$\sigma_{meas}^2 = \sum_{i=1}^{n} \left(\frac{\partial x_{rec}}{\partial q_i} \right)^2 \Delta q_i^2 \tag{4.3}$$

$$\Delta q_i^2 = \sum_{sources} \sigma_j^2 = \sigma_{noise1}^2 + \sigma_{noise2}^2 + ... \tag{4.4}$$

where σ_{meas} is the error of the charge measurement, x_{rec} is the reconstructed value of the cluster position, q_i is the measured charge in strip i with index i denoting the strip number in the cluster of n strips and Δq_i^2 is the noise from different sources [116].

According to the approximation for a linear distribution of charge, one can assume how spatial resolution depends on signal-to-noise ratio:

$$\sigma \approx \frac{1}{SNR} \tag{4.5}$$

Consequently, a figure of merit in these studies is the signal-to-noise ratio. In order to calculate the signal-to-noise for different cluster sizes, it is assumed that the noise is uniform over the full range of connecting scheme:

$$SNR_{cluster} = \frac{S_{cluster}}{\sqrt{m} \times N} \tag{4.6}$$

where S is the sum of signals in the cluster, N is noise of one strip and m is the cluster size.

Based on this approximation, the result on signal-to-noise ratio for 1-strip, 2-strip and 3-strip clusters of different configuration is presented in Table 4.1.

Table 4.1: Signal-to-noise ratio for perpendicular tracks.

Cluster size:	1-strip	2-strip	3-strip
One to one	$60.09/2.58 \sim 23$	$73.42/3.65 \sim 20$	$91.2/4.47 \sim 20$
One omitted	$60.8/2.27 \sim 27$	$56.01/3.21 \sim 18$	$71.79/3.93 \sim 18$
Two to one	$62.18/3.05 \sim 20$	$76.93/4.31 \sim 18$	$96.64/5.28 \sim 18$

Studies with perpendicular electron tracks, where 1-strip and 2-strip cluster events dominate, favour the $2nd \rightarrow 0$ connection scheme for 1-strip cluster events only, where a SNR of 27 is reached, whereas the $1 \rightarrow 1$ and the $2 \rightarrow 1$ reach values of SNR=23 and 20, respectively. For 2-strip clusters, the SNR is 20 for direct and 18 for the other connections.

4.3 Studies with inclined tracks in a proton beam facility

In order to test current set-up at aperture which mimics STS conception, the proton beam at the COSY facility was used. Measurements at proton accelerators allow to perform tests under conditions close to those in the CBM experiment. Due to the very low momentum spread of the proton beam at the COSY accelerator in Jülich, Germany [130], one can perform precise studies of the angular dependence of the sensor response. A proton beam with a kinetic energy of 2.4 GeV has been used, which is close to the minimum ionising regime.

4.3.1 Setup at the proton beam facility

The measuring station (see Fig. 4.14) was placed on a movable platform, which allowed a manual vertical adjustment. The platform was equipped with two step motors in a way that one could remotely control the transverse position and the azimuthal angle of the station. The aluminium box which holds the sensor directly bonded to readout electronics was installed inside the main station. Data taking for this device was conducted at $T = +10°C$ to remove heat generated by the readout electronics. The movable platform was used for the angular scan procedure.
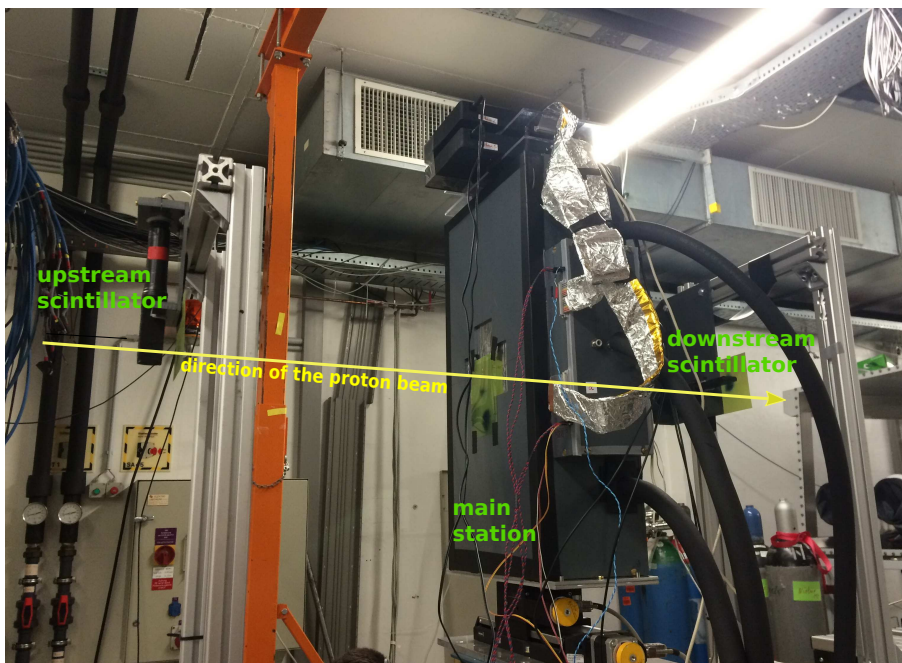
Figure 4.14: Beam test setup in the Jessica cave at COSY (Research Center Jülich).

Since the setup could be operated in the external trigger mode only, a trigger chain based on a pair of plastic scintillation detectors was designed. The time-to-digital converter of the Alibava system provides a relative time between the trigger occurrence over the all readout channels within the 25 ns time window. Before the main measurements, a latency scan had to be done, studying the signal amplitude with respect to the time delay. Two rectangular ($5{\times}20{\times}100$ mm^3) plastic scintillators with photomultiplier tubes were included in the trigger chain. They were mounted on two aluminium frames upstream and downstream the station. The scintillators were positioned cross-like in plastic holders; in that way they constrained a square cross-section of 5×5 mm^2 for the incident particles. In order to cover the active region of the sensor with different connection schemes (22.2 mm wide) the main station had to be moved along the X-axis. The coincidence of two signals within a window of 40 ns was done using NIM electronics. Then the logical signal was fed to the Alibava Mother Board

4.3.2 Data analysis

4.3.2.1 Data reduction

In order to study the performance of the detector, the first step was to locate active time slices, identify and remove bad and corner channels. Once a time cut on the signal of $3\,\text{ns} \leqslant \tau \leqslant 8\,\text{ns}$ is established, the data are scanned for noisy or dead strips. The corner strips for each group of interconnection should be eliminated from the analysis, because they potentially could pick up noise. One can see in Fig. 4.15 (left) an example of multiple events during data-taking caused by the complicated micro-spill structure of the beam. During these multiple-hit events not only events
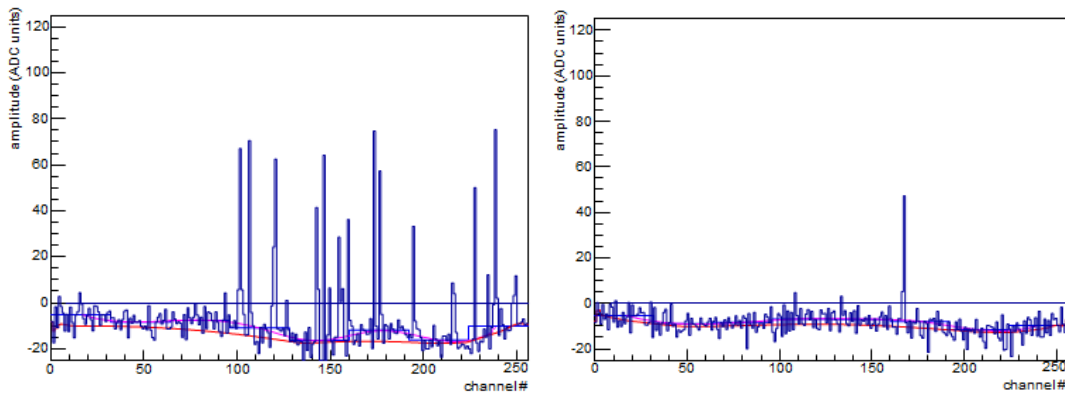
Figure 4.15: Example of multi-hit (left) and single-hit (right) events during data taking at proton beam.

with larger cluster size occur, but also events with multiple interactions (thus one can not associate a time-stamp to a given interaction). The total amplitude of obtained signal doesn't correspond to real signal from the charged particle. For this, an algorithm which rejects multiple-hit events had to be implemented, as these type of events can not be considered and later analysed. In Fig. 4.15 a single-hit event is shown, which is used for further analysis.

Figure 4.16 shows the hit multiplicity of events. One can see that most of the events contain a single hit, but there are also some which have up to twenty hits. Only events with one hit per event were taken into consideration, almost half of the events were rejected.
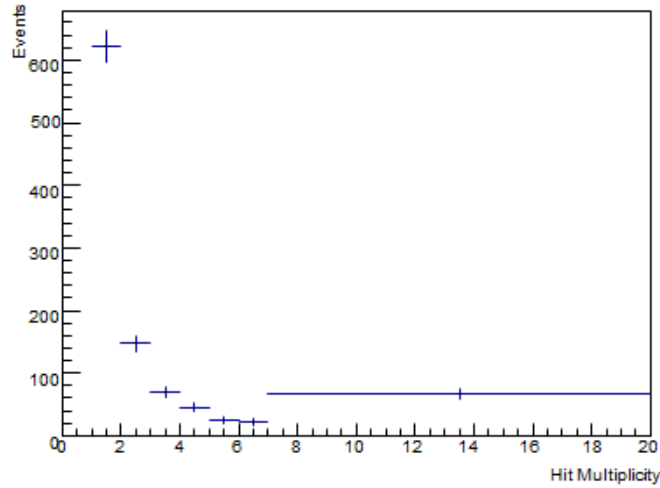
Figure 4.16: Hit multiplicity during data taking with proton beam.

4.3.2.2 Signal amplitude

Due to charge sharing between strips, the distribution for a mixture of all three connection schemes does not follow exactly a Landau-Gauss convolution. The difference is clearly visible at large angles, where more events with large cluster sizes appear. This has also been observed in Ref. [131]. In this case, the Gauss distribution becomes more pronounced in the fitting function: for perpendicular and inclined tracks the width of Landau parameter changes moderately from 6.81 ± 0.10 to 8.46 ± 0.08, but the width of the Gauss increases twice up to 31.89 ± 0.49 after broadening of spectra. Charge spectra at zero angle and at $25°$, with respect to the beam direction, are presented in Fig. 4.17. One can see, that the size of clusters increases with the beam incidence angle, as expected from geometrical considerations.
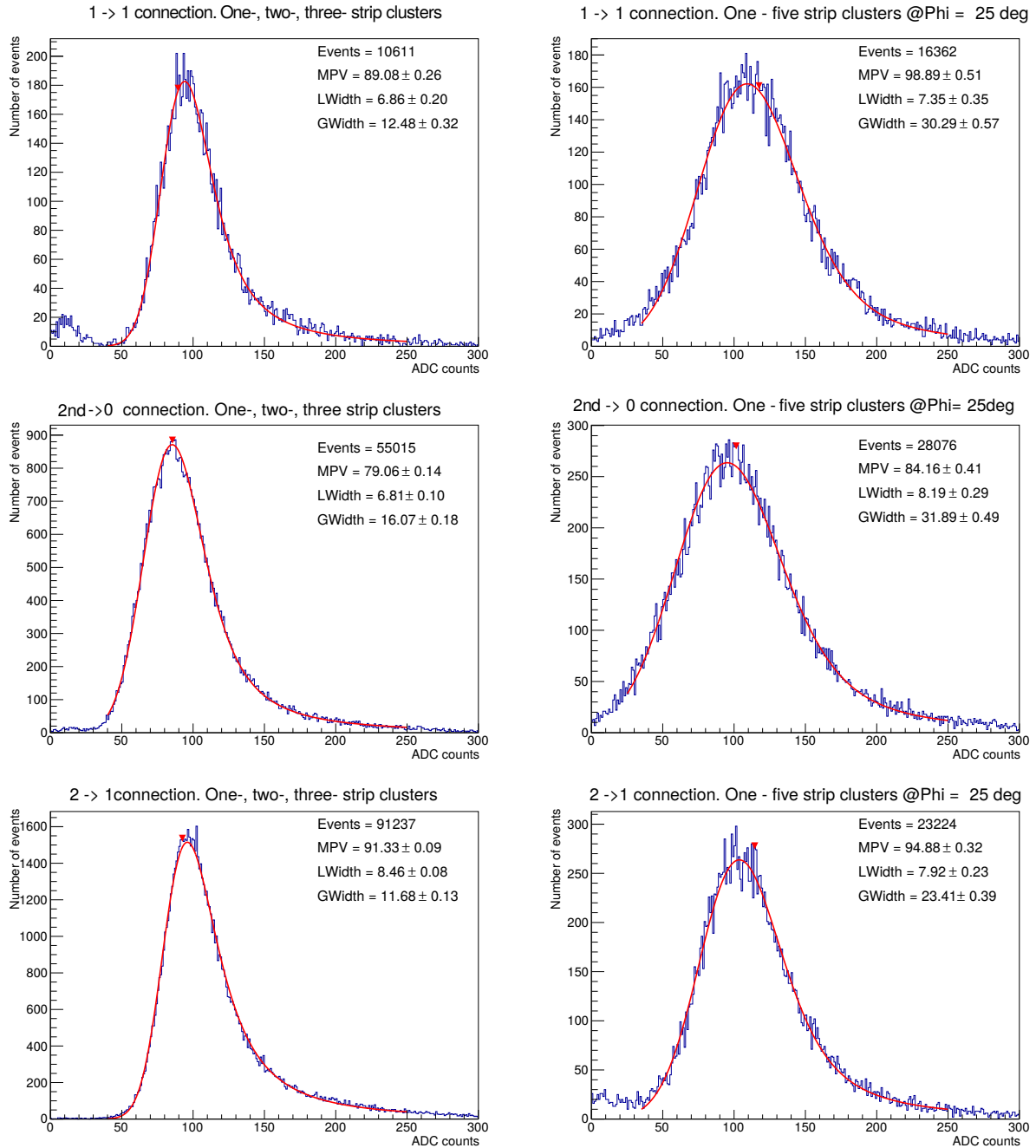
Figure 4.17: Charge collection spectra of 3-strip cluster events and 5-strip cluster events for $0°$ (left column) and $25°$ incidence angles (right column), with respect to the beam direction, for different interconnection schemes: $1 \rightarrow 1$ (top), $2nd \rightarrow 0$ (middle), $2 \rightarrow 1$ (bottom). The parameters of Landau convoluted by Gauss fit are presented in the legends.

The signal amplitude increases by 10 ADC channels for direct connection, because the real cluster size increases; for the other connections the amplitude increases only

by ~ 5 ADC channels, because their effective contributors are up to 5 readout-strip clusters, which translates into 10 sensor strips.

The cluster size distributions for different incidence angles are shown in Fig 4.18. Here, perpendicular particles, with respect to the sensor surface, create mostly 1-strip and 2-strip clusters (70% and 25% respectively), where 3-strip clusters produced in $\sim 3.5\%$ of events and 4-strip in $\sim 1\%$. Presence of noise, cross-talk and diffusion induce charge sharing effects between neighbouring strips, thus not only 1-strip clusters are presented here.

At the maximum aperture of the STS (25°), the size of the cluster increases due to geometrical considerations and main contributors to the signal become 2-strip ($\sim 36\%$ of events), 3-strip clusters ($\sim 57\%$), 4-strip clusters ($\sim 6\%$) and 5-strip clusters ($\sim 1.5\%$). Bigger clusters up to 10-strip are also involved, but their impact the total charge collection is negligible. For large cluster sizes, the spectra become broader. At the same time, the noise increases because of the larger capacitative load.
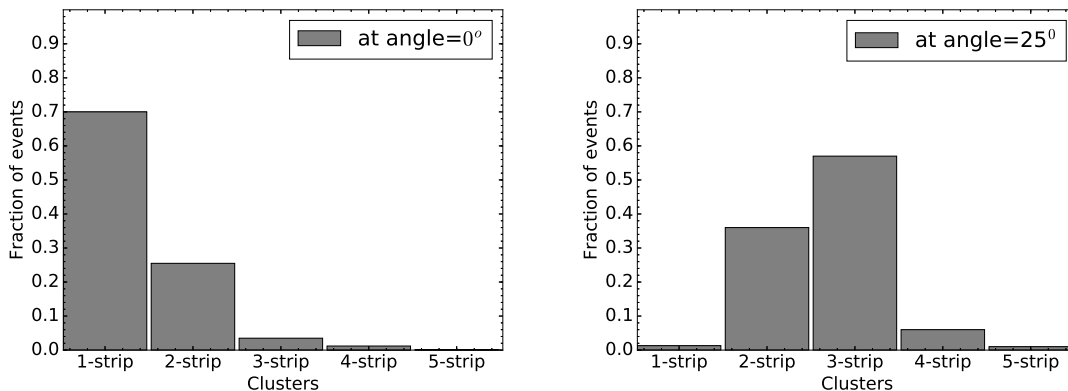
Figure 4.18: Cluster size distributions for perpendicular tracks (left) and for inclined 25° on the p-side of the sensor.

4.3.2.3   Signal-to-noise ratio

The signal-to-noise ratio for the most abundant cluster sizes of perpendicular and inclined proton tracks is shown in Table 4.2 below. Here, the SNR for up to three strip cluster events was used for particles with normal incidence, and from two to four-strip cluster events for inclined tracks.

Studies carried out with perpendicular protons confirm the results obtained in the laboratory condition with electrons from ^{90}Sr source. For 1-strip cluster events

$2nd \to 0$ connection performed with the highest SNR, while for larger cluster sizes
all three schemes represent similarly.

Table 4.2: Signal-to-noise ratio for perpendicular ($0°$) and inclined ($25°$) tracks.

Angle:	at angle = 0°		
Cluster size:	1-strip	2-strip	3-strip
One to one	54.59/2.58 ~ 21	71.65/3.65 ~ 20	77.17/4.47 ~ 17
One omitted	59.74/2.27 ~ 26	60.02/3.21 ~ 19	71.34/3.93 ~ 18
Two to one	57.02/3.05 ~ 19	76.53/4.31 ~ 18	85.16/5.28 ~ 16
Angle:	at angle = 25°		
Cluster size:	2-strip	3-strip	4-strip
One to one	75.12/3.65 ~ 21	92.48/4.47 ~ 21	96.25/5.16 ~ 19
One omitted	71.48/3.21 ~ 22	81.16/3.93 ~ 21	83.98/4.54 ~ 18
Two to one	86.82/4.31 ~ 20	95.38/5.28 ~ 18	97.49/6.1 ~ 16

During the in-beam measurement with inclined tracks, SNR(2-strip clusters) was
found to be at the level of 21 for direct interconnection, while two to one SNR=19
and one omitted SNR=22. For higher cluster size no significant difference was
observed between $1 \to 1$ and $2nd \to 0$ connections, while $2 \to 1$ performed the
lowest SNR values.

4.4 Summary

Three interconnection schemes between sensor strips and readout electronics have
been evaluated:

- each strip is read out by one electronics channel ($1 \to 1$);

- only every second strip is read out ($2nd \to 0$);

- when two strips are bonded to one readout channel ($2 \to 1$).

These different schemes have been tested in the laboratory and in-beam conditions
with perpendicular and inclined tracks of charged particles, with inclination angles
corresponding to the aperture of the STS.

Results obtained for perpendicular particles are in agreement with measurements
conducted with electrons from ^{90}Sr and 2.4 GeV proton beam. Here, connection

$2nd \to 0$ performs higher SNR of 26 for 1-strip clusters, and for 2-strip and 3-strip cluster SNR values are at a comparable level for all three connections.

The measurements with incident particles inclined at 25°, where most of the signal is collected by 2-strip, 3-strip and 4-strip clusters, performed similar results of SNR ~ 20 for direct and one omitted connections, scheme with two strips connected to one readout showed worse values than latter two.

Although schemes $1 \to 1$ and $2nd \to 0$ are similar in terms of signal-to-noise ratio for the larger cluster sizes, connection of every second strip could save amount of routine lines between sensor and readout electronics, but will not save total amount of ASICs. A connection when every second sensor strip is readout, requires additional challenge in the production and further technical implications during module assembly.

An advantage of using a different type of connection scheme than the direct one at the outer aperture of the STS was not confirmed. Therefore, the $1 \to 1$ connection scheme is preferable in the modules for the entire STS detector, which simplifies the fabrication considerably.

5

Summary and conclusions

The major part of this thesis is devoted to the characterization of the radiation hardness of the final version of double-sided silicon microstrip sensors for the CBM Silicon Tracking System.

An extensive irradiation campaign was undertaken at the Irradiation Center Karlsruhe to study the sensor properties as a function of the accumulated fluence. To induce non-ionising radiation damage, sensors were irradiated by 23 MeV protons to fluences up to the double-lifetime of the CBM experiment.

In total, 36 sensors from the final prototype production were characterized. Sensors from two vendors, CiS (Germany) and HPK (Japan), of different form-factors ($62 \times 22\,\text{mm}^2$, $62 \times 42\,\text{mm}^2$, $62 \times 62\,\text{mm}^2$), irradiated with different fluences were studied in detail. A dedicated experimental setup for characterization of the irradiated sensors was designed and built. The measurements were performed in a custom made a light-tight thermal enclosure with temperature and humidity control. In order to suppress the leakage current during the data taking, and to avoid annealing, sensors were permanently kept at a temperature of $-10°$C and at a relative humidity of $30 - 50\%$.

Sensors were characterized by performing a set of tests before and after irradiation. These tests included measurements of leakage current and capacitance dependence as a function of applied voltage, pin-hole tests, charge collection efficiency (CCE) and signal-to-noise ratio (SNR). Characterization studies have confirmed theoretically

expected degradation of sensor properties after irradiation. Namely, the increase of the leakage current, the increase of the full depletion voltage, increase of the noise and the drop of the charge collection efficiency have been observed.

The relative charge collection efficiency of irradiated sensors with respect to non-irradiated drops down to $82\% - 98\%$ for the lifetime fluence (10^{14} $1\,\mathrm{MeV}\,\mathrm{n_{eq}cm^{-2}}$), and down to $73\% - 93\%$ for the double lifetime fluence (2×10^{14} $1\,\mathrm{MeV}\,\mathrm{n_{eq}cm^{-2}}$), both for the p-side and n-side. To provide the highest possible CCE it was necessary to apply an increased biasing voltage, sufficient for the total depletion of a sensor. It was found that the sensors are operational at biasing voltages up to $800\,\mathrm{V}$ and no breakdown occurred at this level. At the level of fluence expected at SIS100 (10^{13} $1\,\mathrm{MeV}\,\mathrm{n_{eq}cm^{-2}}$) no significant charge collection loss was observed for p- and n-side. Measurements of charge collection efficiency demonstrated that sensor prototypes from different vendors perform in the same way within the error bars, although some of them exhibit a stronger CCE drop at high fluences due to the different thickness of sensors.

Studies with ^{90}Sr sources have have been performed to measure response of sensors to MIPs and evaluate their SNR performance. For non-irradiated sensors the SNR was measured to be in the range of $20 - 25$, whereas for irradiated sensors it dropped down to the level of $12 - 17$.

All characterized sensors are found to be radiation hard. They will survive the CBM operation scenario without critical performance degradation.

In accordance with the realistic detector response model, deterioration of the main detector parameters after irradiation like increase of noise (to $2000\,\mathrm{e^-} - 2500\,\mathrm{e^-}$) and drop of CCE (to $90\% - 80\%$), the STS subsystem still meets requirements in track reconstruction efficiency of about 95% and momentum resolution of about 1.5%. However, keeping noise as low as possible for the whole STS is crucial for successful operation during the experiment to produce signal relevant for the CBM physics case.

In addition to the sensor characterization, a part of this thesis was devoted to the optimisation of the sensor readout scheme. In order to investigate, whether the signal-to-noise ratio (SNR) can be increased and the amount of readout channels can be reduced in the outer aperture of STS, three versions of routing lines (direct connection between sensor and readout strips, two strips connected to one readout strip and when every second sensor strip is omitted) have been realized on the p-side readout of the sensor prototype, and have been tested in the laboratory and under beam conditions. The tests have been performed with different inclination angles between beam direction and sensor surface, corresponding to the polar angle acceptance of the CBM experiment, which is from $2.5°$ to $25°$. The signal-to-noise

ratio was taken as a figure of merit for these studies.

Investigations with particles incident perpendicularly to a sensor surface, where one- and two-cluster events are dominating, show that connection, when every second strip is readout, is only favourable for 1-strip clusters (SNR = 26, compared to the other connection schemes where SNR $\sim$ 20), but for larger clusters this scheme does not improve the level of SNR.

During the in-beam measurements with inclined proton tracks, where 2-strip and 3-strip clusters are the most abundant, SNR was found to be at the level of 21 for direct and one omitted connection schemes, while for the two-to-one connection SNR is lower. It was found, that schemes with two sensor strips connected to one readout and reading every second strip, do not have any greater advantage in terms of SNR over the direct connection. It is worthwhile to mention that connection, where every second strip is readout, allows to save the number of readout channels and stay within the same level of SNR at the outer aperture of the STS, however, implementation of different routing lines in microcable masks and TAB-bonding procedure becomes very complicated and eventually does not save the number of readout ASICs and front-end-boards. Therefore $1 \rightarrow 1$ connection scheme is preferable, which simplifies the fabrication considerably.

The studies carried out in this thesis established that the radiation hardness requirements for the CBM STS are met in a part of its final prototype version of the double-sided silicon microstrip sensors. This allowed starting the tendering process for sensor series production in industry, an important step towards the construction of the detector in the coming years. It was also confirmed that the readout scheme using every sensor channel fulfills the performance requirements of the STS detector. The chosen sensor module structure is approved for application throughout the entire detector area.

Zusammenfassung

Die Erforschung der Eigenschaften von Kernmaterie bei sehr hohen Dichten, wie sie etwa im Inneren massenreicher Neutronensterne vorkommen, findet weltweites grosses wissenschaftliches Interesse, kann sie doch zum Verständnis der Formung von Materie aus Elementarteilchen, den Quarks und Gluonen, beitragen. Mit Hilfe von beschleunigten schweren Atomkernen, lassen sich in Kollisionsexperimenten kurzzeitig hochdichte Materiezustände herstellen und detailliert untersuchen. Dabei spielt die Suche nach möglichen Phasenübergängen zwischen hadronischer und partonischer Phase eine wichtige Rolle. Der Ringbeschleuniger SIS-100 der im Bau befindlichen Facility for Antiproton and Ion Research (FAIR) in Darmstadt, wird intensive Schwerionenstrahlen im Energiebereich von 2 bis 15 GeV pro Kernladungszahl liefern. Bei diesen Energien wird die Materie in der Kollisionszone auf bis zu achtfacher Kerndichte komplimiert. In den Stößen werden bis zu 1000 Teilchen erzeugt, die als experimentelle Observable dienen. Als besonders sensitive Sonden dichte Kernmaterie gelten zum Beispiel mehrfach seltsame Teilchen, die jedoch nur äußerstselten produziert werden. Um auch diese Teilchen mit genügender Statistik beobachten zu können, wurde das Compressed Baryonic Matter (CBM) Experiment konzipiert. Es wird mit seinen innovativen Detektorkomponenten und speziellem Datennahmesystem so ausgelegt, dass es bisher unerreichte Kollisionsraten bis zu 10^7 pro Sekunde verarbeiten kann.

Das Compressed Baryonic Matter (CBM) Experiment

Das Experimentprogramm CBM ist eine der wissenschaftlichen Säulen des FAIR-Forschungszentrums in Darmstadt. Die internationale CBM Kollaboration, ein Zusammenschluss von derzeit 460 Wissenschaftlern an 56 Instituten aus 11 Ländern, beabsichtigt, das QCD-Phasendiagramm im Bereich hoher Baryonen-Dichten und moderate Temperaturen unter Verwendung von Schwerionenkollisionen zu untersuchen. Zu den experimentellen Herausforderungen zählt insbesondere, selten produzierte Teilchen in einem grossen Teilchenuntergrund mit ausreichenden Statistiken zu vermessen. Dies erfordert schnelle und strahlungsfeste Detektorsysteme,

die bei hohen Kern-Kern-Kollisionsraten arbeiten können. Das CBM-Experiment umfasstmehrere Detektorsysteme, darunter zwei räumlich hochauflösende Spur- und Vertexdetektoren (Silicon Tracking System, Micro Vertex Detector) in einem starken Dipolmagnetfeld. Weitere Detektoren dienen zur Leptonidentifikation (Ring Imaging Cherenkov Detektor, Transition Radiation Detektor für Elektronen sowie Muon Chambers für Myonen, alternativ installiert) und zur Hadronenmessung (Time of Flight Detektor). Zwei Kalorimeter dienen zur Messung von Photonen (Electromagnetic Calorimeter) und der Zentralitätsbestimmung der Kollisionen (Projectile Spectator Detector). Alle Detektoren werden mit selbstauslösender Ausleseelektronik versehen, welche die Signal-Messwerte der Detektorkanäle mit Zeitstempeln versehen an eine sehr leistungsfähige Computerfarm leiten, wo eine Rekonstruktion der nuklearen Wechselwirkungen und eine Herausfilterung von physikrelevanten Information erfolgt.

Das STS Detektorsystem

Das STS Detektorsystem ist als die zentrale Komponente des CBM Experiments anzusehen, da es als einziger Detektor die Spurmessung der am Target erzeugten geladenen Teilchen durchführt und die Impulse der Teilchen durch Messung der Bahnkrümmung im Dipolmagnetfeld bestimmt. Diese Aufgabe soll mit hoher Effienz ($> 95\,\%$ for $p > 1\,\mathrm{GeV/c}$) und Auflösung ($\Delta p/p < 1.5\%$ for $p > 1\,\mathrm{GeV/c}$) geleistet werden. Der Detektor wird daher aus 8 Spurrekonstrultionsebenen ("Stationen") zwischen 30 und 100 cm strahlabwärts vom Target bestehen, die mit doppelseitigen Silizium-Mikrostreifensensoren belegt sind. Die Sensoren haben vier dabgestufte Streifenlängen von etwa 2, 4, 6 und 12 cm, angepasst an die Teilchendichten in den verschiedenen Aperturbereiche (Polarwinkel 2.5 bis 25 Grad um das Strahlrohr). Der Streifenabstand beträgt 58 μm in der Ablenkrichtung des Magneten. Jeder Sensor ist 62 mm breit und fasst daher 1024 Streifen pro Seite. Insgesamt sind 896 Sensoren im STS verbaut. Jeder Sensor wird mit dedizierten mikroelektronischen Schaltungen ausgelesen.

Die Elektronik befindet sich außehalb aktiven Flähe des Detektors, nur elektrisch durch sehr dünne Mikrokabel mit dem Sensor verbunden. Die STS Stationen sind komplexe Strukturen, bei denen die so gebildeten Sensormodule auf massearme Karbonfaserstrukturen montiert werden. Somit kann innerhalb des Akzeptanzbereichs ein geringes Materialbudget (maximal 1.8% einer Strahlungslänge) erzielt werden, das eine Voraussetzung für hohe Impulsauflösung ist. Infrastruktur und damit verbundene massive Materialien, etwa Kühlstrukturen zur Leistungsabfuhr der Auslese- und Stromversorgungselektronik, liegen ausserhalb montiert auf mechanischen Rahmen. Die Sensoren sind auf eine Strahlungshärte von bis zu $10^{14}\,1\,\mathrm{MeV\,n_{eq}cm^{-2}}$

Equivalent ausgelegt, wie sie im CBM-Betrieb am SIS-100 bzw. an einem späteren SIS-300 Beschleuniger auftreten warden. Dazu müssen sie gekühlt betrieben und der STS Detektor in einer thermischen Isolationsbox eingebaut werden.

Motivation dieser Arbeit

Die Strahlungshärte der STS Sensoren ist eine entscheidende Voraussetzung für einen leistungsfähigen Detektor, der eine zentrale Rolle im CBM Physikprogramm spiel. Durch die in den Kern-Kern-Wechselwirkungen erzeugten geladenen Teilchen wird nicht nur elektrische Ladung in den Sensoren freigesetzt, die zum Nachweis der Teilchen selbst genutzt wird, sondern auch eine Schädigung des Silizium-Kristallgitters in den Sensoren bewirkt, die bei erhöhter Strahlenbelastung die Sensoreigenschaften verschlechtert und die Detektionseffizienz reduziert. Die Sensoren müssen jahrelang im Experiment betrieben werden, wo die Zugangs- und Reparaturmöglichkeiten begrenzt sind.

Das Studium der Strahlenhärte erforderte eine detaillierte Untersuchung der Ladungssammlungseigenschaften und Strahlungstoleranz von Prototypen der STS-Mikrostreifensensoren. Simulationsstudien zum CBM Physik-programm haben gezeigt, dass die Sensoren Schäden aus nichtionisierendem Energieverlust bis 10^{14} 1 MeV $n_{eq}cm^{-2}$ und aus ionisierender Dosis bis 11 kGy widerstehen müssen.

In dieser Arbeit wurden umfangreiche Untersuchungen zum Verhalten der Mikrostreifen-Sensoren auf nichtionisierenden Energieverlust durchgeführt. Die Folgen von Strahlenschäden an Sensoren des Silicon Tracking Systems sind in Kapitel 2-3 zusammengefasst und diskutiert. Es konnte demonstriert werden, dass die Sensoren die Anforderungen erfüllen, wenn sie bei Temperaturen unter $-7°C$ betrieben werden, um strahlungsinduzierte Leckströme zu minimieren.

Ein weiterer Teil dieser Arbeit ist eine Untersuchung der Auslesekonfiguration der Sensoren. In den Aussenbereichen der STS-Stationen, wo der Durchtrittswinkel der geladenen Teilchen von 90 Grad deutlich abweicht, wird Ladung in mehr als einem Auslesestreifen freigesetzt. Das kann dazu führen, dass bei zu hoher Schwelle in der Ausleseelektronik einzelne Kanäle keine Signalmessung durchführen und somit Messfehler entstehen. Untersuchungen zu unterschiedlichen Verbindungsschemata zwischen Sensorstreifen und Auslesekanälen wurden im Hinblick auf das Signal-Rausch-Verhältnis durchgeführt und in Kapitel 4 beschrieben. Die direkte Zuordnung eines jeden Sensorstreifens zu einem Elektronikkanal für die gesamte Detektorfläche erwies sich als optimale Lösung, und fand daher Eingang in das Detektordesign.

Untersuchungen zur Strahlungshärte von CBM-STS Mikrostreifensensoren

Die Strahlungshärte der Mikrostreifensensoren wurde in einer umfangreichen Untersuchung an zuvor strahlungsexponierten Prototypen bestimmt. Zwei grundsätzliche Schädigungen können unterschieden werden. Zum einen Oberflächenschäden durch Ionisationseffekte an der Oberfläche oder in der Passivierungsschicht, und zum anderen Volumenschäden durch nichtionisierenden Energieverlust von durch den Sensor laufenden Teilchen.

Die Auswirkung von Volumenschäden, nämlich die Zunahme des Leckstroms, ändert sich durch strahlungsbedingte Veränderung der Dotierungskonzentration. Dadurch verändert sich auch die Höhe der Sperrspannung, die zur vollständigen Sensitivierung des Detektorvolumens benötigt wird. Kann sie nicht mehr erreicht werden, führt die verringerte Ladungssammlung zu einer beeinträchtigten Leistung des Detektors. Der genaue Verlauf dieses Prozesses ist theoretisch bzw. auch experimentell gut verstanden, muss aber an tatsächlich vorliegenden Sensorprototypen überprüft werden.

Die Sensoren wurden in Zusammenarbeit mit zwei Herstellern (CiS, Deutschland und Hamamatsu Photonics, Japan) entwickelt. Am Bestrahlungszentrum Karlsruhe wurden 36 repräsentative Exemplate mit 23 MeV Protonen bei verschiedenen Fluenzen bis zu 2×10^{14} 1 MeV n_{eq}cm^{-2} equivalent, entsprechend dem zweifachen der erwarteten Lebensdauer im CBM Experiment, bestrahlt und anschliessend auf ihre Betriebs- und Ladungssammlungseigenschaften hin überprüft.

Die Messungen wurden in einem thermisch kontrollierten Laboraufbau und trockener Stickstoffatmosphäre bei -10 Grad Celsius durchgeführt, um die Detektorleckströme zu unterdrücken. Diese Tests umfassten die Abhängigkeit von Strom und Sensorkapazität als Funktion der angelegten Spannung, Streifenintegritätstests, Prüfung des Signal-Rausch-Verhältnisses (SNR) und schliesslich Bestimmung der Ladungssammeleffizienz (CCE). Hier wurde die relative Ladungssammlung, d.h. das Verhältnis von bestrahlten zu unbestrahlten Sensoren betrachtet. Bei wie erwartet vorgefundenem Anstieg von Verarmungsspannung, Leckstrom und Rauschen mit zunehmender Fluenz wurden keine Einbußen der Ladungssammlung bis zu Fluenzen von 1×10^{13} 1 MeV n_{eq}cm^{-2} vorgefunden. Bei 1×10^{14} 1 MeV n_{eq}cm^{-2}, der erwarteten Lebensdosis, betrug die Ladungssammlung 82% - 98% des ursprünglichen Wertes. Bei doppelter Fluenz wurden 73% - 93% ermittelt. Die Sensoren beider Hersteller verhielten sich dabei weitgehend gleich. Somit konnte festgestellt werden, dass alle Sensoren strahlungshart sind und den Betrieb im für das CBM Experiment vorgesehen Szenario ohne kritischen Leistungsabfall überstehen.

Untersuchungen zur Auslesegranulatität der CBM-STS Mikrostreifensensoren

In den Außenbereichen des STS Detektors treten die Teilchenspuren unter größeren Winkeln durch die Sensoren als in den Bereichen nahe des Strahlrohres. Dies kann einerseits dazu führen, dass mehrere Sensorstreifen pro Spurpunkt ein Signal sammeln, und andererseits zu einem gerigerem Signal pro Streifen, und somit zu verschlechterter Nachweiseffizienz.

Um dies zu untersuchen, wurden drei Verbindungsschemata zwischen Sensorstreifen und Ausleseelektronikkanälen vermessen. Neben der standardmäßigen direkten Verbindung, wo jeder Streifen durch einen eigenen Elektronikkanal ausgelesen wird $(1 \rightarrow 1)$, wurde auch getestet, dass nur jeder zweite Streifen ausgelesen wird $(2nd \rightarrow 0)$. Ebenso wurden auch zwei Sensorstreifen zusammen durch einen Auslesekanal gelesen $(2 \rightarrow 1)$. Diese Schemata wurden auf einer Adapterplatine zwischen Sensoren und Ausleseelektronik implementiert. Diese Struktur wurde im Labor getestet und unter Bedingungen im Teststrahlexperiment mit senkrechten und geneigten Teilchenspuren, bei denen die Neigungswinkel denen im STS Detektor entsprachen.

Ein Vorteil der Verwendung einer anderen Art von Verbindungsschemata als der direkten Verbindung an der äußeren Öffnung von STS wurde nicht gefunden. Daher konnte bestätigt werden, dass nur ein einziges Anschlussschema in den Modulen für den gesamten STS Detektor benötigt wird, was die Herstellung wesentlich vereinfacht.

Die erzielten Ergebnisse trugen wesentlich dazu bei, das Design des STS Detektors festzulegen, und die Ausschreibung der Serienfertigung der Mikrostreifensensoren in der Industrie zu ermöglichen.

A

Selected sensors and their specifications

On the next tables, specifications of sensors after irradiation are presented. Prototypes were fabricated by CiS and Hamamatsu (HPK) from different generations. Each generation was produced in different batches on wafers in order number. The fluence to which prototypes were exposed is indicated. Table A.1 shows operational voltage and value of the leakage current at $500\,\mathrm{V}$. Operational voltage differs from the full depletion voltage and is defined after charge collection efficiency reaches plateau with the applied bias voltage. Charge collection efficiency saturates only when sufficient bias voltage was applied. One has to apply more voltage to operate HPK sensors compared to CiS due to the larger thickness and lower values of initial effective impurity concentration.

Noise, signal (most probable value at $5 \times \sigma$ threshold), charge collection efficiency for p- and n-side after irradiation are presented In Tables A.2-A.4. Some of the prototypes have shown spoiled signal by noise, that is why it was hard to obtain its MPV, for these sensors CCE indicated as a blank.

Size	Vendor and gen.	Batch #	Wafer #	Fluence, $10^{14}\mathrm{n_{eq}/cm^2}$	Current at $500\,\mathrm{V},\mu\mathrm{A/cm^2}$	Operation voltage, V
$62\times62\,\mathrm{mm^2}$	CiS 06	350191	*09*	*0.0*	*0.253*	150
			03	1.0	5.7	350
			08	1.0	14.3	350
			01	2.0	8.7	≥ 500
			10	2.0	9.7	≥ 500
	HPK 06	S10938-4440	*72*	*0.0*	*0.012*	150
			65	1.0	12.7	400
			71	1.0	10.2	400
			59	2.0	20.1	≥ 500
			79	2.0	14.1	≥ 500
$62\times42\,\mathrm{mm^2}$	CiS 08	351135	*05*	*0.0*	*0.124*	150
		351135	02	0.1	1.7	150
		351139	01	0.1	1.9	150
		351135	11	0.5	11.8	300
		351135	06	1.0	16.2	350
		351139	08	2.0	22.7	≥ 500
	HPK 06	S10938-5552	*84*	*0.0*	*0.006*	150
			33	0.5	7.0	300
			32	1.0	15.4	400
			31	2.0	28.2	≥ 500
$62\times22\,\mathrm{mm^2}$	CiS 07	350714	22-3	0.5	8.0	300
			23-1	0.5	9.6	300
			21-3	1.0	24.2	350
			23-2	1.0	12.4	350
			17-3	2.0	29.5	≥ 500
			23-3	2.0	29.1	≥ 500
	HPK 06	S10938-4723	06	0.5	4.7	300
			04	0.5	5.1	300
			08	1.0	11.4	400
			01	1.0	54.2	400
			02	2.0	25.1	≥ 500
			05	2.0	22.7	≥ 500

Table A.1: Selected sensors and their characteristics after irradiation. The reference (zero-dose) sensors of $62\times62\,\mathrm{mm^2}$ and $62\times42\,\mathrm{mm^2}$ groups marked with italic, here their current presented before irradiation. Each of the $62\times22\,\mathrm{mm^2}$ sensors served as a reference to itself.

Table A.2: Selected 2×6 cm^2 HPK sensors, their specifications and measured values. Absolute values as Noise and MPV are in ADC counts.

Vendor	Gen.	Batch	Wafer	Fluence, $n_{eq}/$cm^2	Noise @p	MPV @p	CC @p	Noise @n	MPV @n	CC @n
HPK	06	4723	01	1×10^{14}	–	–	–	–	–	–
			02	2×10^{14}	9.6±0.5	150	76±8 %	9.4±0.6	176	77±1 %
			04	5×10^{13}	9.3±0.7	194	99±1 %	9.6±0.8	200	89±5 %
			05	2×10^{14}	–	–	–	9.6±0.6	176	78±3 %
			06	5×10^{13}	8.5±0.5	192	100±1 %	9.0±0.6	196	85±3 %
			08	1×10^{14}	9.2±0.6	166	87±3 %	9.8±0.5	–	–

Table A.3: Selected 4×6 cm^2 sensors, their specifications and measured values. Absolute values as Noise and MPV are in ADC counts.

Vendor	Gen.	Batch	Wafer	Fluence, $n_{eq}/$cm^2	Noise @p	MPV @p	CC @p	Noise @n	MPV @n	CC @n
CiS	08	351135	05	0 – reference	8.9±0.6	170	100 %	9.0±0.8	192	100 %
		351135	06	1×10^{14}	10.3±0.6	160	94±3 %	9.1±0.4	178	93±4 %
		351139	08	2×10^{14}	11.8±0.8	140	82±4 %	9.5±0.3	172	90±5 %
		351135	11	5×10^{13}	9.9±0.7	174	102±3 %	12.0±0.8	172	90±6 %
HPK	06	5552	84	0 – reference	8.7±0.6	182	100 %	9.0±0.8	218	100 %
			31	2×10^{14}	10.4±0.9	132	73±9 %	10.1±0.6	180	83±3 %
			32	1×10^{14}	9.5±0.4	178	98±2 %	9.2±0.4	190	87±2 %
			33	5×10^{13}	9.6±0.7	186	99±7 %	9.3±0.5	190	87±2 %

Table A.4: Selected 6×6 cm^2 sensors, their specifications and measured values. Absolute values as Noise and MPV are in ADC counts.

Vendor	Gen.	Batch	Wafer	Fluence, $n_{eq}/$cm^2	Noise @p	MPV @p	CC @p	Noise @n	MPV @n	CC @n
CiS	06	350191	09	0 – reference	9.7±0.5	152	100 %	8.1±0.4	194	100 %
			01	2×10^{14}	11.7±0.4	142	93±3 %	10.7±0.4	190	98±3 %
			03	1×10^{14}	12.5±0.4	150	97±10 %	–	–	–
			08	1×10^{14}	11.9±0.4	144	95±7 %	10.3±0.4	186	96±3 %
			10	2×10^{14}	–	–	–	10.9±0.5	180	93±1 %
HPK	06	4440	72	0 – reference	9.9±0.6	182	100 %	9.0±0.8	218	100 %
			59	2×10^{14}	10.4±0.9	132	73±8 %	10.1±0.6	180	83±4 %
			65	1×10^{14}	9.5±0.4	178	82±5 %	9.2±0.4	190	86±2 %
			71	1×10^{14}	9.6±0.7	186	–	9.3±0.5	190	87±1 %
			79	2×10^{14}	11.2±0.3	158	93±0.4 %	11.7±0.4	192	85±3 %

B

Additional plots of the CCE

The charge collection efficiency plots separately for HPK and CiS sensors of different outer dimensions are presented below in Fig. B.1-B.2. Figure B.3 shows a performance of the $62 \times 22\,\text{mm}^2$, $62 \times 42\,\text{mm}^2$, $62 \times 62\,\text{mm}^2$ sensors irradiated up to twice lifetime fluence.

Charge collection efficiency was defined as a ratio between charge collected by irradiated to the collected charge of the same non-irradiated sensor. Measurement from the same sensors placed one marker under another. Blue color represent p-side and red – n-side.

Estimation of the systematic errors

Systematic uncertainty for the CCE is estimated using following approaches for the measurement of its central value:

- MPV at $3 \times \sigma$ threshold;

- MPV at $5 \times \sigma$ threshold;

- Mean value at $5 \times \sigma$ threshold.

Thus, with 3 values that slightly differ from each other, we get error bars that were calculated as follows: $\Delta\varepsilon_{\text{syst}} = \sqrt{(\varepsilon_{3 \times \sigma} - \varepsilon_{5 \times \sigma})^2 + (\varepsilon_{\text{mean}} - \varepsilon_{5 \times \sigma})^2}$.

During these studies result for charge collection was presented as: $\varepsilon_{5 \times \sigma} \pm \Delta\varepsilon_{\text{syst}}$.
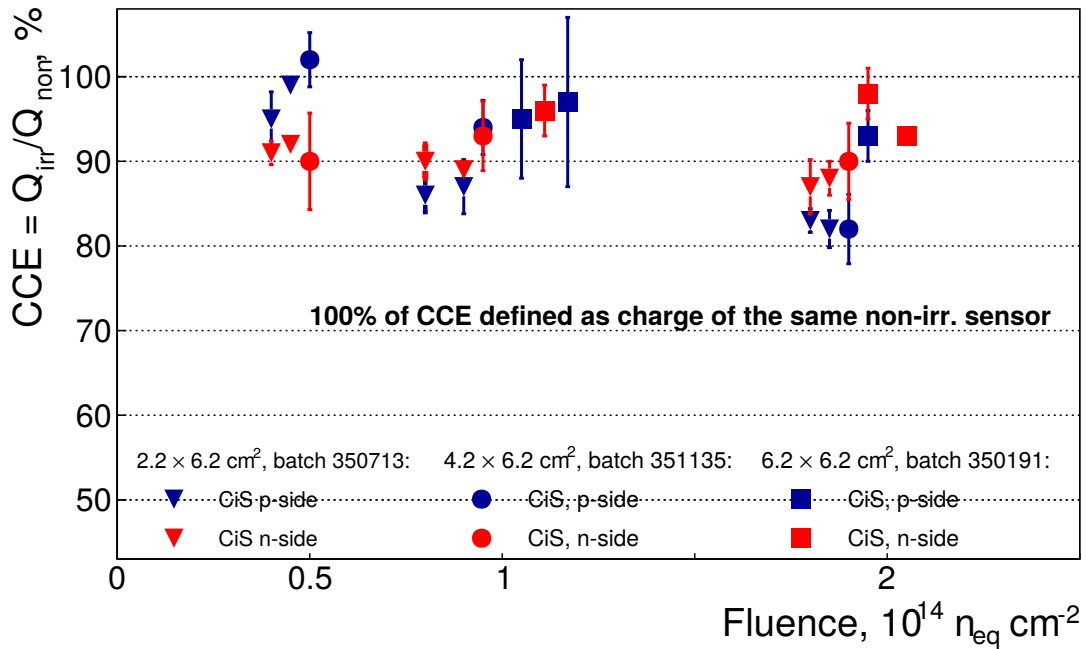
Figure B.1: Charge collection efficiency as a function of fluence for CiS sensors.
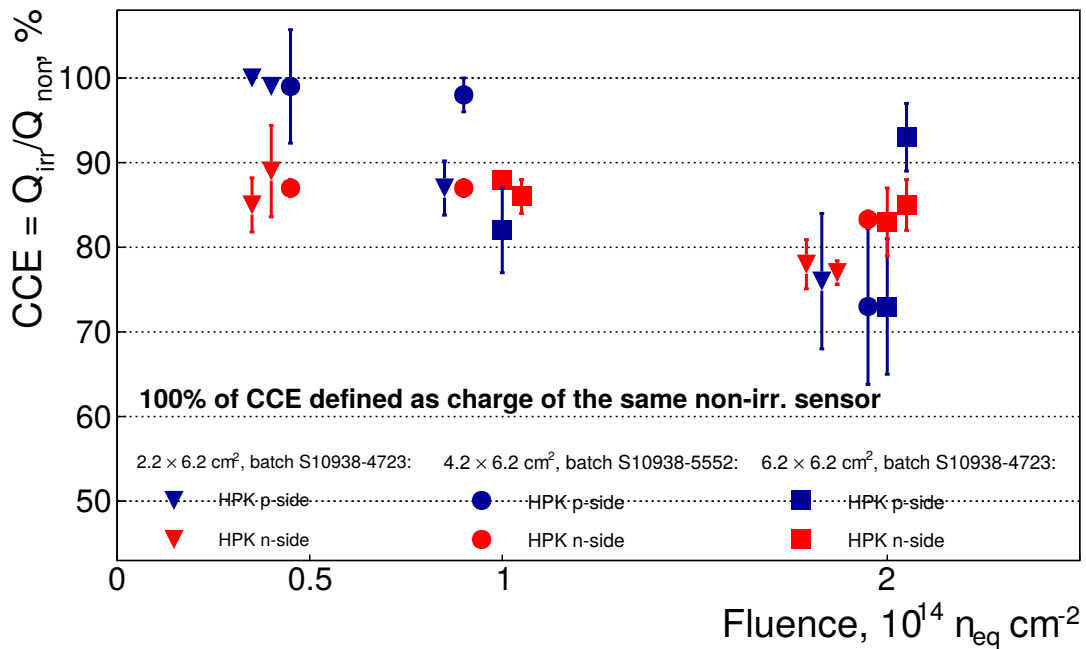
Figure B.2: Charge collection efficiency as a function of fluence for HPK sensors.
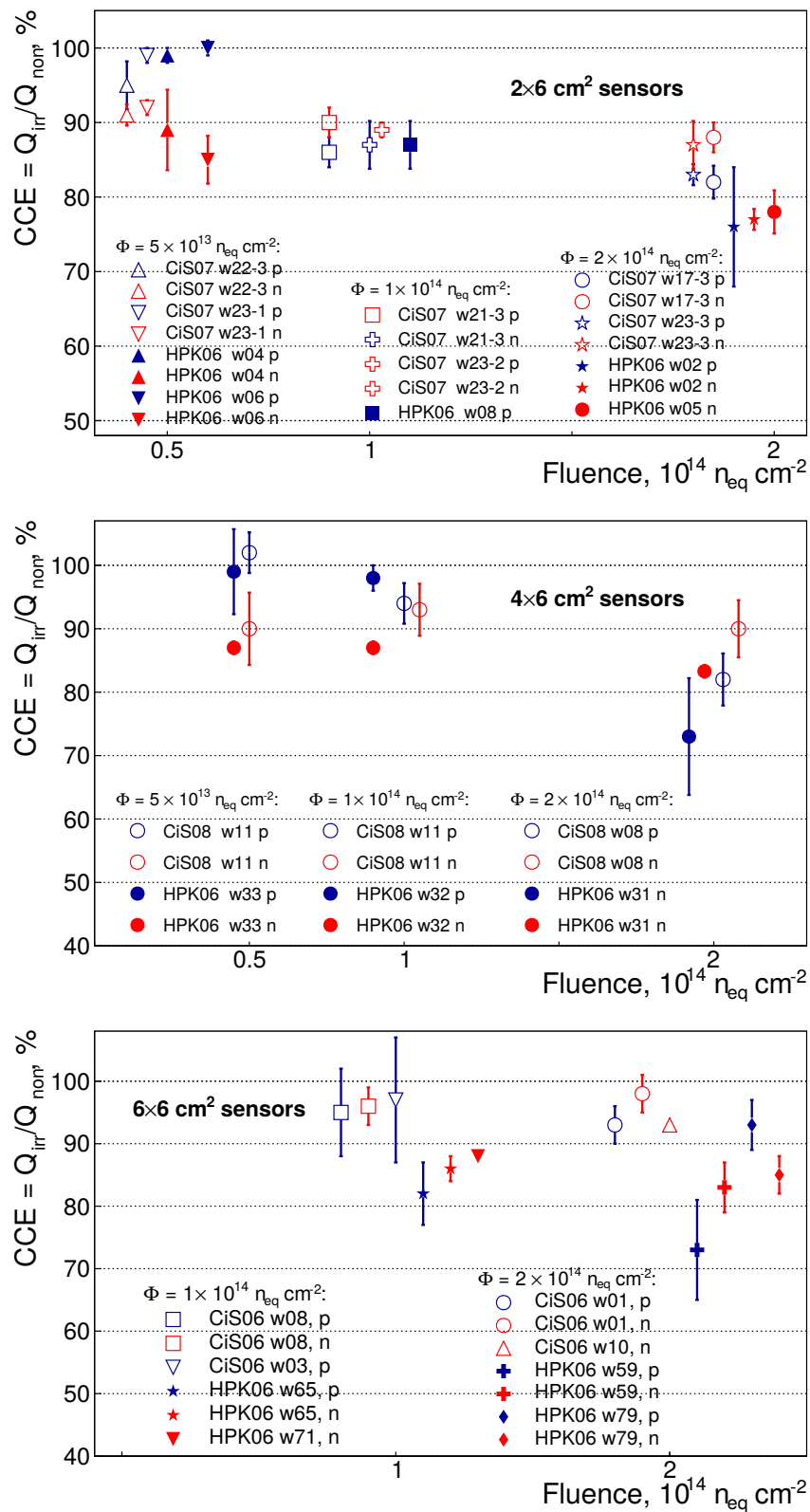
Figure B.3: Charge collection efficiency as a function of the fluence for irradiated $62 \times 22\,\mathrm{mm}^2$(top), $62 \times 42\,\mathrm{mm}^2$ (middle), $62 \times 62\,\mathrm{mm}^2$(bottom) sensors. Points corresponding to the same fluence are spread horizontally for illustration purpose.

List of figures

References

[1] G. Stephans, "Probing the extremes of high baryon density nuclear matter: The BNL AGS program," *Nuclear Physics A*, vol. 583, pp. 653–662, 1995. Nucleus-Nucleus Collisions.

[2] M. Gazdzicki, "The SPS ion program and the first LHC data," *AIP Conference Proceedings*, vol. 1422, no. 1, pp. 98–103, 2012.

[3] B. Mohanty and t. S. Collaboration, "STAR experiment results from the beam energy scan program at the RHIC," *Journal of Physics G: Nuclear and Particle Physics*, vol. 38, no. 12, p. 124023, 2011.

[4] J. T. Mitchell, "The RHIC Beam Energy Scan Program: Results from the PHENIX Experiment," *Nuclear Physics A*, vol. 904-905, pp. 903c–906c, 2013. The Quark Matter 2012.

[5] P. Romatschke and U. Romatschke, "Viscosity Information from Relativistic Nuclear Collisions: How Perfect is the Fluid Observed at RHIC?," *Phys. Rev. Lett.*, vol. 99, p. 172301, Oct 2007.

[6] N. Armesto and E. Scomparin, "Heavy-ion collisions at the Large Hadron Collider: A review of the results from Run 1," *The European Physical Journal Plus*, vol. 131, p. 52, Mar 2016.

[7] A. Andronic *et al.*, "Excitation function of elliptic flow in Au+Au collisions and the nuclear matter equation of state," *Phys. Lett.*, vol. B612, pp. 173–180, 2005.

[8] P. Senger *et al.*, "The kaon spectrometer at SIS," *Nuclear Instruments and Methods in Physics Research Section A: Accelerators, Spectrometers, Detectors and Associated Equipment*, vol. 327, no. 2, pp. 393–411, 1993.

[9] T. Galatyuk, "HADES overview," *Nuclear Physics A*, vol. 931, pp. 41–51, 2014. QUARK MATTER 2014.

[10] Spiller P. and Franchetti G., "The FAIR accelerator project at GSI," vol. 561, no. 2, pp. 305–309.

[11] A. Sorin, V. Kekelidze, A. Kovalenko, R. Lednicky, I. Meshkov, and G. Trubnikov, "Heavy-ion program at NICA/MPD at JINR," *Nuclear Physics A*, vol. 855, no. 1, pp. 510–513, 2011. Proceedings of the 4th International Conference on Hard and Electromagnetic Probes of High-Energy Nuclear Collisions – HP2010.

[12] V. Friese, "The CBM experiment at GSI/FAIR," *Nuclear Physics A*, vol. 774, pp. 377–386, 2006. QUARK MATTER 2005.

[13] D. Baranov, M. Kapishin, T. Mamontova, G. Pokatashkin, I. Rufanov, V. Vasendina, and A. Zinchenko, "The BM@N Experiment at JINR: Status and Physics Program," *KnE Energy*, vol. 3, no. 1, pp. 291–296, 2018.

[14] Odyniec, Grazyna, "Future of the beam energy scan program at RHIC," *EPJ Web of Conferences*, vol. 95, p. 03027, 2015.

[15] F. Becattini, M. Bleicher, T. Kollegger, T. Schuster, J. Steinheimer, and R. Stock, "Hadron Formation in Relativistic Nuclear Collisions and the QCD Phase Diagram," *Physical Review Letters*, vol. 111, p. 082302, Aug. 2013.

[16] J. Stachel, A. Andronic, P. Braun-Munzinger, and K. Redlich, "Confronting LHC data with the statistical hadronization model," *Journal of Physics: Conference Series*, vol. 509, no. 1, 2014.

[17] A. Bazavov *et al.*, "Chiral and deconfinement aspects of the QCD transition," *Phys. Rev. D*, vol. 85, p. 054503, Mar 2012.

[18] S. Borsányi, Z. Fodor, C. Hoelbling, S. D. Katz, S. Krieg, C. Ratti, and K. K. Szabó, "Is there still any T c mystery in lattice QCD? Results with physical masses in the continuum limit III," *Journal of High Energy Physics*, vol. 2010, p. 73, Sep 2010.

[19] Y. Aoki, G. Endrődi, Z. Fodor, S. D. Katz, and K. K. Szabó, "The order of the quantum chromodynamics transition predicted by the standard model of particle physics," *Nature*, vol. 443, pp. 675–678, Oct. 2006.

[20] Letter of Intent for the Compressed Baryonic Matter Experiment at the Future Accelerator Facility in Darmstadt, Darmstadt, January 2004.

[21] Z. Fodor and S. D. Katz, "Lattice determination of the critical point of QCD at finite T and mu," *JHEP*, vol. 03, p. 014, 2002.

[22] B. Friman, C. Höhne, J. Knoll, S. Leupold, J. Randrup, R. Rapp, and P. Senger, *The CBM physics book. Compressed baryonic matter in laboratory experiments*, vol. 814. 01 2011.

[23] I. C. Arsene, L. V. Bravina, W. Cassing, Y. B. Ivanov, A. Larionov, J. Randrup, V. N. Russkikh, V. D. Toneev, G. Zeeb, and D. Zschiesche, "Dynamical phase trajectories for relativistic nuclear collisions," *Phys. Rev. C*, vol. 75, p. 034902, Mar 2007.

[24] W. Cassing, E. L. Bratkovskaya, and A. Sibirtsev, "Open charm production in relativistic nucleus-nucleus collisions," *Nucl. Phys.*, vol. A691, pp. 753–778, 2001.

[25] A. Adronic. Private communication.

[26] T. Ablyazimov *et al.*, "Challenges in QCD matter physics –The scientific programme of the Compressed Baryonic Matter experiment at FAIR," *Eur. Phys. J.*, vol. A53, no. 3, p. 60, 2017.

[27] W. Reisdorf, A. Andronic, R. Averbeck, M. Benabderrahmane, O. Hartmann, N. Herrmann, K. Hildenbrand, T. Kang, *et al.*, "Systematics of central heavy ion collisions in the 1A GeV regime," *Nuclear Physics A*, vol. 848, no. 3, pp. 366–427, 2010.

[28] H. Oeschler, H. G. Ritter, and N. Xu, "Hadron Production in Heavy Ion Collisions: Datasheet from Landolt-Börnstein - Group I Elementary Particles, Nuclei and Atoms · Volume 23: "Relativistic Heavy Ion Physics" in Springer-Materials (http://dx.doi.org/10.1007/978-3-642-01539-7_5)." Copyright 2010 Springer-Verlag Berlin Heidelberg.

[29] J. Auvinen, J. Steinheimer, and H. Petersen, "What the collective flow excitation function can tell about the quark–gluon plasma," *Nucl. Phys.*, vol. A931, pp. 975–980, 2014.

[30] F. Karsch and E. Laermann, "Thermodynamics and in medium hadron properties from lattice QCD," 2003.

[31] M. A. Stephanov, "Sign of Kurtosis near the QCD Critical Point," *Phys. Rev. Lett.*, vol. 107, p. 052301, Jul 2011.

[32] J.-W. Chen, J. Deng, and L. Labun, "Baryon susceptibilities, non-Gaussian moments, and the QCD critical point," *Phys. Rev. D*, vol. 92, p. 054019, Sep 2015.

[33] P. Koch, B. Müller, and J. Rafelski, "Strangeness in relativistic heavy ion collisions," *Physics Reports*, vol. 142, no. 4, pp. 167–262, 1986.

[34] M. Gazdzicki, "Strangeness and pion production as signals of QCD phase transition," *J. Phys.*, vol. G23, pp. 1881–1888, 1997.

[35] B. Tomášik and E. E. Kolomeitsev, "Complete strangeness measurements in heavy-ion collisions," *The European Physical Journal A*, vol. 52, p. 251, Aug 2016.

[36] V. Manzari, t. N. Collaboration, F. Antinori, A. Badala, R. Barbera, H. Beker, I. J. Bloodworth, J. Böhm, M. Botje, *et al.*, "Experiment NA57 at the CERN SPS," *Journal of Physics G: Nuclear and Particle Physics*, vol. 25, no. 2, p. 473, 1999.

[37] S. V. Afanasiev, T. Anticic, D. Barna, J. Bartke, R. A. Barton, M. Behler, L. Betev, H. Białkowska, *et al.*, "Energy dependence of pion and kaon production in central Pb+Pb collisions," *Phys. Rev. C*, vol. 66, p. 054902, Nov 2002.

[38] P. Braun-Munzinger, J. Stachel, and C. Wetterich, "Chemical freezeout and the QCD phase transition temperature," *Phys. Lett.*, vol. B596, pp. 61–69, 2004.

[39] L. D. McLerran and T. Toimela, "Photon and dilepton emission from the quark-gluon plasma: Some general considerations," *Phys. Rev. D*, vol. 31, pp. 545–563, Feb 1985.

[40] H. A. Weldon, "Reformulation of finite temperature dilepton production," *Phys. Rev.*, vol. D42, pp. 2384–2387, 1990.

[41] R. Rapp and H. van Hees, "Thermal dileptons as fireball thermometer and chronometer," *Physics Letters B*, vol. 753, pp. 586–590, 2016.

[42] T. Matsui and H. Satz, "J/ψ Suppression by Quark-Gluon Plasma Formation," *Phys. Lett.*, vol. B178, pp. 416–422, 1986.

[43] A. Adare, S. Afanasiev, C. Aidala, N. N. Ajitanand, B. M. Johnson, K. S. Joo, D. Jouan, F. Kajihara, *et al.*, "J/ψ," *Phys. Rev. Lett.*, vol. 98, p. 232301, Jun 2007.

[44] B. Abelev *et al.*, "J/ψ suppression at forward rapidity in Pb-Pb collisions at $\sqrt{s_{NN}} = 2.76$ TeV," *Phys. Rev. Lett.*, vol. 109, p. 072301, 2012.

[45] A. S. Botvina, J. Steinheimer, E. Bratkovskaya, M. Bleicher, and J. Pochodzalla, "Formation of hypermatter and hypernuclei within transport models in relativistic ion collisions," *Phys. Lett.*, vol. B742, pp. 7–14, 2015.

[46] S. Bufalino, "Strangeness and nuclei production in nuclear collisions." Talk at QM2018.

[47] I. Augustin, H. H. Gutbrod, D. Kramer, K. Langanke, and H. Stocker, "New Physics at the International Facility for Antiproton and Ion Research (FAIR) Next to GSI," in *4th International Conference on Fission and Properties of Neutron Rich nuclei (ICFN4) Sanibel Island, Florida, USA, November 11-17, 2007*, 2008.

[48] S. Chattopadhyay, "Physics at FAIR," *Nuclear Physics A*, vol. 931, pp. 267–276, 2014. QUARK MATTER 2014.

[49] "FAIR – An International Facility for Antiproton and Ion Research." http://www.fair-center.eu/index.php?id=1.

[50] "APPA physics – Atomic, Plasma Physics and Applications." http://www.fair-center.eu/public/experiment-program/appa-physics.html.

[51] "CBM – Compressed Baryonic Matter experiment." http://www.fair-center.eu/for-users/experiments/nuclear-matter-physics/cbm/introduction.html.

[52] "Nustar - Nuclear Structure, Astrophysics and Reactions." http://www.fair-center.eu/public/experiment-program/nustar-physics.html.

[53] "PANDA – Antiproton Annihilation at Darmstadt." http://www.fair-center.eu/public/experiment-program/antiproton-physics/panda.html.

[54] A. Malakhov and A. Shabunov, eds., *Technical Design Report for the CBM Superconducting Dipole Magnet*. Darmstadt: GSI, 2013.

[55] P. Kurilkin *et al.*, "Superconducting dipole magnet for the CBM experiment at FAIR," *EPJ Web Conf.*, vol. 138, p. 12001, 2017.

[56] M. Koziel, S. Amar-Youcef, N. Bialas, M. Deveaux, *et al.*, "The prototype of the Micro Vertex Detector of the CBM Experiment," *Nuclear Instruments and Methods in Physics Research Section A: Accelerators, Spectrometers, Detectors and Associated Equipment*, vol. 732, pp. 515–518, 2013. Vienna Conference on Instrumentation 2013.

[57] J. Heuser, W. Müller, V. Pugatch, P. Senger, C. J. Schmidt, C. Sturm, and U. Frankenfeld, eds., *[GSI Report 2013-4] Technical Design Report for the CBM Silicon Tracking System (STS)*. Darmstadt: GSI, 2013.

[58] S. Chattopadhyay, Y. P. Viyogi, P. Senger*, W. F. J. Müller*, and C. J. Schmidt*, eds., *Technical Design Report for the CBM : Muon Chambers (MuCh)*. Darmstadt: GSI, 2015.

[59] C. Höhne* *et al.*, "Technical Design Report for the CBM Ring Imaging Cherenkov Detector," tech. rep., 2013.

[60] B. Friman, C. Höhne, J. Knoll, S. Leupold, J. Randrup, R. Rapp, and P. Senger, "The CBM physics book: Compressed baryonic matter in laboratory experiments," *Lect. Notes Phys.*, vol. 814, pp. pp.1–980, 2011.

[61] N. Herrmann, ed., *Technical Design Report for the CBM Time-of-Flight System (TOF)*. Darmstadt: GSI, 2014.

[62] I. E. Korolko, M. S. Prokudin, and Y. M. Zaitsev, "The CBM ECAL," *Journal of Physics: Conference Series*, vol. 798, no. 1, p. 012164, 2017.

[63] F. Guber and I. Selyuzhenkov, eds., *Technical Design Report for the CBM Projectile Spectator Detector (PSD)*. Darmstadt: GSI, 2015.

[64] J. Heuser and V. Friese, "Measurement of rare probes with the silicon tracking system of the CBM experiment at FAIR," *Nuclear Physics A*, vol. 931, pp. 1136–1140, 2014. QUARK MATTER 2014.

[65] I. Vassiliev, P. Senger, I. Kisel, and M. Zyzak, *Hypernuclei Program at the CBM Experiment*.

[66] O. Vassyliev, "Status of STS System Integration." private communication.

[67] P. Grybos, R. Szczygiel, K. Kasinski, R. Kleczek, and P. Otfinowski, "STS-XYTER a prototype silicon strip detector readout chip for the STS," tech. rep. https://repository.gsi.de/record/51956/files/PHN-NQM-EXP-22.pdf.

[68] K. Kasinski, R. Kleczek, and R. Szczygiel, "Front-end readout electronics considerations for Silicon Tracking System and Muon Chamber," *Journal of Instrumentation*, vol. 11, no. 02, p. C02024, 2016.

[69] "CBM Radiation simulations," 2017. private communication, plots based on Fluka simulation of A. Senger.

[70] "Cortesy of Volker Friese. Private communication.."

[71] I. Kisel, "Event reconstruction in the CBM experiment," *Nuclear Instruments and Methods in Physics Research Section A: Accelerators, Spectrometers, Detectors and Associated Equipment*, vol. 566, no. 1, pp. 85–88, 2006. TIME 2005.

[72] T. Basar, *A New Approach to Linear Filtering and Prediction Problems*. IEEE, 2001.

[73] S. Gorbunov and I. Kisel, "Reconstruction of decayed particles based on the Kalman filter." May 2007.

[74] G. Lutz, *Semiconductor Radiation Detectors.* Springer, 2001.

[75] F. Hartmann, "Silicon tracking detectors in high-energy physics," *Nuclear Instruments and Methods in Physics Research Section A: Accelerators, Spectrometers, Detectors and Associated Equipment*, vol. 666, pp. 25–46, 2012. Advanced Instrumentation.

[76] D. Bortoletto, A. Garfinkel, A. Hardman, K. Hoffman, T. Keaffaber, N. Shaw, and G. Stanley, "Capacitance measurements of double-metal double-sided silicon microstrip detectors," *Nuclear Instruments and Methods in Physics Research Section A: Accelerators, Spectrometers, Detectors and Associated Equipment*, vol. 383, no. 1, pp. 104–109, 1996. Development and Application of Semiconductor Tracking Detectors.

[77] J. Kemmer and G. Lutz, "New structures for position sensitive semiconductor detectors," *Nuclear Instruments and Methods in Physics Research Section A: Accelerators, Spectrometers, Detectors and Associated Equipment*, vol. 273, no. 2, pp. 588–598, 1988.

[78] M. S. Lazo, D. M. Woodall, and P. J. McDaniel, "Silicon and silicon dioxide neutron damage functions," in *Proc. Fast Burt React. Workshop*, vol. 1, 1987.

[79] "ASTM E722-14: Standard Practice for Characterizing Neutron Fluence Spectra in Terms of an Equivalent Monoenergetic Neutron Fluence for Radiation-Hardness Testing of Electronics."

[80] M. Moll, *Radiation Damage in Silicon Particle Detectors.* PhD thesis, Universität Hamburg, 1999.

[81] H. Spieler, *Semiconductor Detector Systems.* Series on Semiconductor Science and Technology, OUP Oxford, 2005.

[82] Y. Shi, D. X. Shen, F. M. Wu, and K. J. Cheng, "A numerical study of cluster center formation in neutron-irradiated silicon," *Journal of Applied Physics*, vol. 67, no. 2, pp. 1116–1118, 1990.

[83] V. A. V. Lint, "The physics of radiation damage in particle detectors," *Nuclear Instruments and Methods in Physics Research Section A: Accelerators, Spectrometers, Detectors and Associated Equipment*, vol. 253, no. 3, pp. 453–459, 1987.

[84] W. Shockley and W. T. Read, "Statistics of the Recombinations of Holes and Electrons," *Phys. Rev.*, vol. 87, pp. 835–842, Sep 1952.

[85] H. Boesch and F. McLean, "Hole transport and trapping in field oxides," *IEEE Trans. Nucl. Sci.*, vol. NS-32 N 6, 1985.

[86] M. D. Rold *et al.*, "Study of breakdown effects in silicon multiguard structures," *IEEE Transactions on Nuclear Science*, vol. 46, pp. 1215–1223, Aug 1999.

[87] M. Huhtinen, "Simulation of non-ionising energy loss and defect formation in silicon," *Nuclear Instruments and Methods in Physics Research Section A: Accelerators, Spectrometers, Detectors and Associated Equipment*, vol. 491, no. 1, pp. 194–215, 2002.

[88] E. M. Donegani, E. Fretwurst, E. Garutti, R. Klanner, G. Lindstroem, I. Pintilie, R. Radu, and J. Schwandt, "Study of point- and cluster-defects in radiation-damaged silicon," *Nucl. Instrum. Meth.*, vol. A898, pp. 15–23, 2018.

[89] B. R. Gossick, "Disordered Regions in Semiconductors Bombarded by Fast Neutrons," *Journal of Applied Physics*, vol. 30, no. 8, pp. 1214–1218, 1959.

[90] S. J. Watts, J. Matheson, I. H. Hopkins-Bond, A. Holmes-Siedle, A. Mohammadzadeh, and R. Pace, "A new model for generation-recombination in silicon depletion regions after neutron irradiation," *IEEE Transactions on Nuclear Science*, vol. 43, pp. 2587–2594, Dec 1996.

[91] K. Gill, G. Hall, and B. Macevoy, "Bulk damage effects in irradiated silicon detectors due to clustered divacancies," *Submitted to: J. Appl. Phys.*, 1997.

[92] P. Larionov, *Systematic irradiation studies and Quality Assurance of silicon strip sensors for the CBM Silicon Tracking System.* PhD thesis, Johann Wolfgang Goethe-Universität Frankfurt, 2016.

[93] E. Gatti and P. F. Manfredi, "Processing the signals from solid-state detectors in elementary-particle physics," *Nuovo Cimento Rivista Serie*, vol. 9, pp. 1–146, Jan. 1986.

[94] "Recent advances in the development of radiation tolerant silicon detectors for the SLHC." https://indico.cern.ch/event/62864/attachments/1006220/1431375/090717-Detector-Seminar-Moll-final.pdf.

[95] G. Casse, *The effect of hadron irradiation on the electrical properties of particle detectors made from various silicon materials.* PhD thesis, Grenoble-1 University, 1998.

[96] "KIT – ETP Proton Irradiation." http://www.etp.kit.edu/english/irradiation_center.php.

[97] A. Dierlamm, "Irradiations in Karlsruhe." `https://indico.cern.ch/event/86625/contributions/2103519/attachments/1080676/1541436/Irradiations_Ka.pdf`.

[98] G. C. Messenger and M. S. Ash, *The effects of radiation on electronic systems.* Reinhold Company, 1986.

[99] M. J. Berger, "ESTAR, PSTAR, and ASTAR: Computer programs for calculating stopping-power and range tables for electrons, protons, and helium ions," vol. -1, 11 1992.

[100] S. M. Sze, *Physics of semiconductor devices /2nd edition/.* 1981.

[101] J. Blocki, "The thermal failure analysis of microstrip silicon detectors," *Nuclear Instruments and Methods in Physics Research A*, vol. 564, pp. 197–203, Aug. 2006.

[102] T. Kohriki, T. Kondo, H. Iwasaki, S. Terada, Y. Unno, and T. Ohsugi, "First observation of thermal runaway in the radiation damaged silicon detector," *IEEE Transactions on Nuclear Science*, vol. 43, pp. 1200–1202, June 1996.

[103] O. Bertini, E. Friske, J. Heuser, P. Larionov, A. Lymanets, I. Momot, I. Panasenko, H. Schmidt, and M. Teklishyn, "Specifications for Quality Assurance of Microstrip Sensors in the CBM Silicon Tracking System," tech. rep., Nov. 2016.

[104] M. Morone, *Evaluation of Silicon sensors for the ATLAS Silicon Tracker, and TPC reconstruction in the HARP Experiment.* PhD thesis.

[105] I. Panasenko, E. Lavrik, A. Lymanets, and H. R. Schmidt, "A Custom Probe Station for Microstrip Detector Quality Assurance of the CBM Experiment," *Journal of Physics: Conference Series*, vol. 742, no. 1, p. 012037, 2016.

[106] W. Zubrzycka and K. Kasiński, "Noise considerations for the STS/MUCH readout ASIC," `https://indico.gsi.de/event/6883/session/0/contribution/4/material/slides/0.pdf`.

[107] F. Lutz, "The ATLAS Silicon Microstrip Tracker," `https://web.physik.rwth-aachen.de/service/wiki/pub/Feld/FeldVortraege/sct_seminar_19_12_00.pdf`.

[108] "IAEA Nuclear Data Section." `https://www-nds.iaea.org/relnsd/NdsEnsdf/nuclide.jsp?NUCID=90SR&unc=nds`.

[109] "Nuclear Science References," 2018. Information extracted from the NSR database ENSDF.

[110] C. Patrignani *et al.*, "Review of Particle Physics," *Chin. Phys.*, vol. C40, no. 10, p. 100001, 2016.

[111] R. Talman, "On the Statistics of Particle Identification Using Ionization," *Nucl. Instrum. Meth.*, vol. 159, p. 189, 1979.

[112] "ALIBAVA systems." https://www.alibavasystems.com/.

[113] S. Löchner *et al.*, *The Beetle reference manual for chip version 1.3, 1.4 and 1.5.* LHCb note, August 2006.

[114] R. Marco-Hernandez *et al.*, "ALIBAVA: A portable readout system for silicon microstrip sensor," *IEEE Trans. Nucl. Sci.*, vol. 56, pp. 1642–1649, 2009.

[115] S. Löchner, *Development, optimisation and characterisation of a radiation hard mixed-signal readout chip for LHCb.* PhD thesis, Heidelberg Uni., 2006.

[116] H. Malygina, *Hit reconstruction for the Silicon Tracking System of the CBM experiment.* PhD thesis, Johann Wolfgang Goethe-Universität Frankfurt, 2018.

[117] I. Momot, M. Teklishyn, A. Lymanets, O. Bertini, and J. Heuser, "Investigation into the charge collection efficiency of prototype microstrip sensors for the CBM Silicon Tracking System," *Journal of Physics: Conference Series*, vol. 1024, no. 1, p. 012004, 2018.

[118] I. Momot, M. Teklishyn, O. Bertini, and J. Heuser, *Charge collection efficiency of irradiated STS silicon micro-strip sensors.* GSI, 2017. http://repository.gsi.de/record/209729/files/CBMProgressReport2017.pdf.

[119] M. Singla, P. Larionov, I. Momot, T. Balog, J. Heuser, I. Sorokin, and C. Sturm, *Neutron irradiated prototype CBM-STS microstrip sensors tested for double metal or cable interconnections of the end strips.* Darmstadt: GSI, 2014. http://repository.gsi.de/record/97909/files/978-3-9815227-1-6.pdf.

[120] I. Momot, H. Malygina, M. Singla, P. Larionov, T. Balog, M. Teklishyn, J. Heuser, and C. Sturm, *Charge collection of n-irradiated prototype CBM-STS microstrip sensors.* GSI, 2015. https://cbm-wiki.gsi.de/foswiki/pub/Public/CbmPr2015/cbm_pr2015_compressed.pdf.

[121] H. Malygina, *Hit reconstruction for the Silicon Tracking System of the CBM experiment.* PhD thesis, Johann Wolfgang Goethe-Universität Frankfurt, 2018.

[122] A. Rodriguez Rodriguez. Private communication.

[123] H. Malygina. Private communication.

[124] T. Kawasaki, "The Belle Silicon Vertex Detector," *Nuclear Instruments and Methods in Physics Research Section A: Accelerators, Spectrometers, Detectors and Associated Equipment*, vol. 494, no. 1, pp. 94–101, 2002. Proceedings of the 8th International Conference on Instrumentatio n for Colliding Beam Physics.

[125] R. Angstadt, L. Bagby, A. Bean, T. Bolton, D. Buchholz, *et al.*, "The layer 0 inner silicon detector of the D0 experiment," *Nuclear Instruments and Methods in Physics Research Section A: Accelerators, Spectrometers, Detectors and Associated Equipment*, vol. 622, no. 1, pp. 298–310, 2010.

[126] S. Straulino, O. Adriani, L. Bonechi, M. Bongi, S. Bottai, *et al.*, "Spatial resolution of double-sided silicon microstrip detectors for the PAMELA apparatus," *Nuclear Instruments and Methods in Physics Research Section A: Accelerators, Spectrometers, Detectors and Associated Equipment*, vol. 556, no. 1, pp. 100–114, 2006.

[127] V. Re *et al.*, "Status and prospects of the BaBar SVT," *Nucl. Instrum. Meth.*, vol. A560, pp. 5–8, 2006.

[128] C. Grupen and B. Shwartz, *Particle Detectors*. Cambridge University Press, 2 edition ed., Apr. 2008.

[129] "LHCb collaboration," http://lhcb.web.cern.ch/lhcb/.

[130] R. Maier, "Cooler synchrotron COSY — Performance and perspectives," *Nuclear Instruments and Methods in Physics Research Section A: Accelerators, Spectrometers, Detectors and Associated Equipment*, vol. 390, no. 1, pp. 1–8, 1997.

[131] J. DeWitt, D. Dorfan, T. Dubbs, A. Grillo, B. Hubbard, S. Kashigin, *et al.*, "Signal-to-noise in silicon microstrip detectors with binary readout," *IEEE Transactions on Nuclear Science*, vol. 42, pp. 445–450, Aug 1995.

Acknowledgments